2022

Visible light positioning systems under imperfect synchronization and signal-dependant noise

Cheema, Ahmad

Visible Light Positioning Systems under Imperfect Synchronization and Signal-Dependant Noise

by

AHMAD CHEEMA

Graduate Program
in
Department of Electrical and Computer Engineering

A thesis submitted in partial fulfillment of the requirements
for the degree of Doctor of Philosophy (Ph.D.)

The Faculty of Graduate Studies
Lakehead University
Thunder Bay, Ontario, Canada

December 2021

Examining Committee Membership

The following served on the Examining Committee for this thesis. The decision of the Examining Committee is by majority vote.

External Examiner: Tariq Sajjad
Assistant Professor, Dept. of Electrical Engineering,
London South Bank University, United Kingdom

Internal Member: Abdulsalam Yassine
Associate Professor, Dept. of Software Engineering,
Lakehead University, Canada

Ruizhong Wei
Professor, Dept. of Computer Science,
Lakehead University, Canada

Supervisor: Salama Ikki
Associate Professor, Dept. of Electrical Engineering,
Lakehead University, Canada

Co-Supervisor: Malek Alsmadi
Postdoctoral Fellow , Dept. of Electrical Engineering,
Lakehead University, Canada

Author's Declaration

I hereby declare that I am the sole author of this thesis. This is a true copy of the thesis, including any required final revisions, as accepted by my examiners.

I understand that my thesis may be made electronically available to the public.

Acknowledgements

First and foremost, I am grateful to Almighty Allah (Subhanahu Wa Ta'ala) for His countless blessings and for giving me the opportunity and capacity to endeavour to complete my Ph.D. research.

I want to express my sincere gratitude to my supervisors, Dr. Salama Ikki and Dr. Malek Alsmadi, for their patience, motivation, and immense knowledge. Over the years, Dr Ikki has been more than a teacher and a supervisor; he has been a great role model and mentor. I could not have accomplished what I had set out to achieve without his unconditional help and unlimited support.

I am also grateful to Prof. Ruizhong Wei, and Dr. Abdulsalam Yassine for serving on my thesis committee and providing constructive comments that have improved my thesis. By the same vein, I am thankful to Prof. Rachid Benlamri and Prof. Ruizhong Wei for serving on my seminar and comprehensive exam committees and providing constructive comments that guided me in finishing this thesis.

I am also indebted to all my colleagues at Lakehead University, Electrical and Computer Engineering Department, for making my Ph.D. study such a great experience. Special and heartiest thanks to my friends, Mohannad Al-Mousa, Ibrahim Al-Hurani, Osama Amjad, and Emad Saleh for their help and invaluable insights.

My most profound appreciation and sincere thanks go to my family for their prayers, support, and care. Your love and encouragement have always been an excellent source of inspiration in my life. I want to express my most sincere appreciation of my parents for their heartfelt prayers, endless love, support, and numerous sacrifices for our family and me. Special thanks to my wife, who has been the joy of my life. Maria, my work could not have been completed without your undying love, support, and sacrifice. Last but not least, I thank my lovely kids, Zynub, Bilal, Lylah, and Khawlah, for being so spectacular and filling our lives with love and hope. I am looking forward to having more fun with you all.

Dedication

This is dedicated to my deceased mother, Musarrat Begum. She passed away in March of 2020. I am especially grateful to you Ami jee for always encouraging me to aim higher in life and teaching me to be kind to others.

May Allah (Subhanahu Wa Ta'ala) grant her place in Jannah al Firdous Aameen!

Abstract

Optical Wireless Communication (OWC) is an enabling technology for sixth-generation (6G) and beyond communication networks. Visible light communication (VLC) is a crucial branch of OWC technology expected to meet 6G communication system requirements. The VLC system can facilitate multiple functionalities simultaneously including illumination, ultra-high data rate communications, positioning such as location and navigation services. In VLC systems, a light-emitting diode (LED) functions as a transmitter. A photodetector or imaging sensor acts as a receiver and the visible light is used as the transmission medium. Researchers have shown a great deal of interest in VLC based positing and localization techniques, as visible light positioning (VLP) systems have shown better localization accuracy than radio frequency (RF) based positioning or global positioning system (GPS). This thesis considers the problem of position estimation accuracy in VLC systems in the presence of signal-dependent shot noise (SDSN). We investigate distance and 3D position estimation approaches in different scenarios, focusing on error estimation performance bounds. Additionally, this work attempts to resolve the synchronization problem found in VLP systems.

First, we investigate VLP systems in the presence of SDSN. Here, synchronous, quasi-synchronous and asynchronous downlink communications are considered when evaluating the Cramér–Rao lower bounds (CRLBs). Moreover, the performance assessment is based on time of arrival (TOA), received signal strength (RSS), hybrid (time difference of arrival (TDOA-RSS), and hybrid (TOA-RSS) based distance and 3D position estimations. Second, we propose a bi-directional synchronization protocol, which can mitigate the effects of timing clock biasing between the LED transmitters and photodetector receivers. The results demonstrate that SDSN has a critical impact on the VLP bounds in all the considered scenarios. Moreover, the level of degradation observed at higher SDSN levels is not uniform among all scenarios. Furthermore, bi-directional distance estimation protocol outperforms directional estimation techniques even in the case of perfect synchronization between the LED transmitter and photodetector receiver.

Table of Contents

List of Tables

List of Figures

Abbreviations

2D two-dimensional 5, 15

2G second-generation 12

3D three-dimensional 4, 6, 8, 9, 32, 34, 35, 38, 55, 73, 74, 78, 79, 81, 95, 97

5G fifth-generation 1

6G sixth-generation 1–3, 12, 27, 37

A-interface application interface 19, 20

AE application entity 20

AI artificial intelligence 1

AOA angle of arrival 4, 32, 33, 55

AP access point 56–59, 62, 67

APC application protocol convergence 20

APD avalanche photodiode 26

AWGN additive white Gaussian noise 5, 38, 56

CC convolutional code 22

CCD charge coupled device 15

CDMA code division multiple access 26

CMOS complementary metal oxide semiconductor 15

CRC cyclic redundancy check 26

CRLB Cramér–Rao lower bound 4, 7, 8, 38, 39, 41–47, 49–52, 55, 56, 61, 62, 64–74, 79, 81–85, 88, 90, 92, 94, 96–98

CSK color-shift keying 25

CSMA carrier sense multiple access 26

CSMA/CA carrier sense multiple access/collision avoidance 26, 27

CT computed tomography 4, 29

DC direct current 23, 24

DD direct detection 20, 39, 56, 75

DL down-link 6–9, 39, 56–59, 62, 68, 75, 76

DLL data link layer 17, 20

DME device management entity 18

EMI electromagnetic interference 3, 15, 29, 55

FDMA frequency-division multiple access 26, 75

FEC forward error-correction 22, 26

FIM fisher information matrix 42–45, 47, 61–63, 65, 66, 68, 82

FOV field of view 5, 39, 74, 76

FSK frequency shift keying 25

FSO free-space optical 12–14, 37

Gbps gigabit per second 1, 2, 14, 54

GPS global positioning system 3, 30, 31

I2V infrastructure-to-vehicle 29, 55

IEEE Institute of Electrical and Electronics Engineers 16–18, 21, 22, 24, 26

IM intensity modulation 20, 25, 39, 56, 75

IoT Internet of Things 1, 11

IR infrared 2, 5, 12–14, 20, 32, 37

ISC image-sensor communication 15

ISI intersymbol interference 2

ITU-R International Telecommunication Union Radiocommunication Sector 17

ITU-T International Telecommunication Union Telecommunication Standardization 17, 19, 20

JEITA Japan Electronics and Information Technology Industries Association 16

LAN local area network 20

LCD liquid crystal display 15

LD laser diode 2, 14

LED light-emitting diode 2, 5–7, 14, 15, 24, 25, 27–29, 31–36, 38, 51, 54, 56, 57, 59, 67, 72, 74–77, 81, 82, 84, 86, 87, 92, 98

Li-Fi light fidelity 12–14, 37

LLC logical link control 18, 20

LOS line of sight 5, 13, 28, 32, 35, 38, 39, 45, 57, 74–76

MAC medium access control 16–18, 20, 26

MCPS MAC common-part sublayer 17

MDI medium-dependent interface 19

MIMO multiple inputs and multiple outputs 3, 38

MLME MAC layer management entity 17, 18

mMTC massive machine type communications 1

MPM mirror pulse modulation 25

MRI magnetic resonance imaging 4, 29, 73

NOMA non-orthogonal multiple access 26

OCC optical camera communication 12, 14, 15, 21, 37

OFDM orthogonal frequency division multiplexing 19, 20, 25

OFDMA orthogonal frequency division multiple access 26

OOK ON-OFF keying 25

OWC Optical wireless communication 1, 2, 8, 12, 13, 15–17, 37

PCS physical coding sublayer 20

PD physical layer data 17

PDOA phase difference of arrival 4, 33, 55

PHY I physical layer I 19, 20

PHY II physical layer II 19

PHY-switch physical layer switch 17

PIN p-type, intrinsic, and n-type 25, 35

PLC power line communication 3, 20, 29, 38

PLME physical layer management entity 17, 18

PMA physical medium attachment 20

PMD physical medium dependent 20

PMI physical medium-independent interface 19, 20

PN p-type and n-type 25

PPM pulse-position modulation 25

PSK phase shift keying 25

PWM pulse width modulation 25

RF radio frequency 1–4, 11, 20, 21, 27–31, 37, 38, 55, 73

RFID radio frequency identification 31, 32

RGB Red, Green and Blue 2, 38, 98

RLL run length limited 23, 24

RS Reed-Solomon 22

RSS received signal strength 4, 6–8, 32–34, 38–40, 45, 46, 50, 52, 55, 64, 70, 74, 79, 82, 84, 90, 92, 96–98

SAP service access point 17, 18, 26

SDMA space division multiple access 26

SDSN signal-dependent shot noise 5–9, 34–36, 38–41, 49–52, 55–58, 60, 64, 66, 70–72, 74, 97, 98

SM spatial modulation 25

SP spatial multiplexing 25

SSCS service-specific convergence sublayer 18

Tbps terabit per second 1, 54

TDMA time-division multiple access 26, 75

TDOA time difference of arrival 4, 6, 8, 32–34, 55, 56, 74, 82, 96, 98

TOA time of arrival 4, 6–8, 32, 33, 38–40, 43, 45, 52, 55, 74, 79, 82, 96–98

UD user device 56–59, 62, 68

UL up-link 7, 56–59, 62, 68

UV ultraviolet 2, 12, 14, 20, 37

V2I vehicle-to-infrastructure 29, 55

V2V vehicle-to-vehicle 29, 55

V2X vehicle-to-anything 3, 29, 38

VAT Vehicular Assistant Technology 16

VLC visible light communication 2–9, 14–17, 19–21, 24–32, 35–39, 54–57, 72–75, 78, 84, 86, 97, 98

VLCA Visible Light Communication Association 16

VLCC Visible Light Communication Consortium 16

VLP visible light positioning 3–9, 31, 33–36, 38, 39, 43, 45, 52, 55, 56, 58, 60, 64, 66, 73–75, 77–79, 81, 82, 95–98

VPAN VLC personal area network 18

VPPM variable pulse position modulation 25

Wi-Fi wireless fidelity 13, 27–29, 31

WLAN wireless local area network 3, 13, 20, 29

WPAN wireless personal area network 13, 16

List of Symbols

α	optical channel attenuation factor
R	photodetector responsivity
R	photodetector responsivity
$x(t)$	transmitted signal
$r(t)$	received signal
τ	time of arrival
$\xi_{sh}(t)$	shot noise
$\xi_{th}(t)$	thermal noise
ζ_n	scaling factor between variance of input-dependent and input-independent noises
$\mathcal{N}(\mu, \sigma^2)$	real Gaussian random variable with μ mean and σ^2 variance
μ_n	the mean of the random variable n
σ_n^2	variance of the random variable n
m	LED's Lambertian order
d	distance between LED transmitter and photodetector receiver

h	perpendicular height of LED transmitter with respect to photodetector receiver
ϕ	irradiance angle
θ	incidence angle
c	represents the speed of light
∇_{ϱ}	gradient operator
$\mathbb{E}\{\cdot\}$	expectation operator
$\mathbf{x}$	vector $\mathbf{x}$
$\mathbf{X}$	matrix $\mathbf{X}$
$[X]^{-1}$	indicates matrix inverse
$[x]^T$	indicates vector transpose
$[X]^T$	indicates matrix transpose
trace$[X]$	the sum of elements on the main diagonal of matrix
$\|\cdot\|$	the Euclidean norm of the vector
a_j	the j^{th}element of any column or row vector $\boldsymbol{a}$

Chapter 1

Introduction

1.1 Background and Motivation

There has been an exponential growth of connected devices. We are witnessing the birth of the Internet of Things (IoT). Now not only our smartphones and computers are connected to the internet but also our household items (e.g., smart washing machines & fridges) [1, 2]. This has led to the evolution of fifth-generation (5G) and beyond wireless communication technology. However, the sixth-generation (6G) has set even more demanding system requirements than the 5G [3–5]. The 6G systems are expected to have even higher system capacity, higher energy constraints, ultra-high data density, ultra-high reliability (99.99999%), ultra-high data rates (gigabit per second (Gbps) to terabit per second (Tbps)), and ultra-low latency (sub-millisecond) [6–8]. The 6G systems will support ubiquitous global connectivity for massive machine type communications (mMTC) with enhanced security and artificial intelligence (AI) integration to support seamless connectivity [6–8]. The radio frequency (RF) communication alone will not be enough to meet all the needs.

Optical wireless communication (OWC) is an enabling technology for 6G and beyond communication networks [6–10]. OWC technologies utilize optically transparent media

to transmit data over optical links, using ultraviolet (UV), infrared (IR), or visible light spectrum for signal propagation. The transmission nature of the optical medium provides a spatial reuse and protection from the RF spectrum co-channel and intersymbol interference (ISI), and diminishes the spectrum crunch issue in wireless communication [11]. Furthermore, the OWC spectrum provides secure communication with its physical layer's inherent properties but also adds range limitations as the light can not pass through opaque materials [7]. The other key feature includes infrastructure, mobile, and vehicle network topologies in terrestrial, space, and underwater applications [12]. The primary benefits of the OWC are the ultra-high bandwidth in the unregulated license-free spectrum, ultra-high data rate, and ultra-low latency [6–8, 13].

There are approximately more than 10 billion light-emitting diode (LED) based light infrastructures in the world according to the statistics from the United States Department of Energy [14]. The LED based artificial light sources are everywhere around us, from lights on the ceiling to the screen of our smartphones, from the headlights of a car to the streetlights. A new form of communication technology has been developed, which uses modern LEDs for communication. It is known as visible light communication (VLC) and it can complement RF communication to meet the growing connectivity requirements [15]. The VLC technology serves a dual purpose by providing communication and lighting at the same time [16, 17].

The VLC systems are among emerging communication technologies expected to meet 6G communication system requirements [6]. In VLC systems, LED or laser diode (LD) functions as the transmitter, the photodetector (also referred to as a light sensor or a photodiode) or the imaging sensor acts as the receiver, and the visible light is used as the transmission medium [13, 16–20]. The VLC systems for indoor communication are anticipated to achieve an ultra-high data rate. For instance, the researchers have demonstrated over 100 Gbps data rate in an indoor optical bi-directional wireless link [21].

The current research explores LED light emission (Red, Green and Blue (RGB),

Table 1.1: VLC and RF communication comparison

Attribute	**RF Communication**	**VLC**
Standard	Matured	Nascent
electromagnetic interference (EMI)	Affected	Not affected
Spatial reuse	Low	High
Bandwidth	Low	High
Security concern	Signal penetrates walls	Communication within enclosed area
Deployment	Medium to hard	Easy
Coverage area	Medium	Short
Propagation losses	Low	High
Data rate	High	Very high

White), multiple inputs and multiple outputs (MIMO), modulation techniques, multiple access techniques, and bi-directional communication to achieve the 6G system requirements [16–20]. The VLC systems can support particular applications that include wireless local area network (WLAN), underground mine communications, vehicle-to-anything (V2X) communication, underwater communications, and hybrid communication with power line communication (PLC) or RF communication [16–19, 22]. Table 1.1 provides a comparisons between RF and VLC communication.

In literature, researchers have shown a great deal of interest in VLC based positing and localization techniques, as the visible light positioning (VLP) systems have shown better localization accuracy than existing systems such as RF positioning and global positioning system (GPS) [23, 24]. VLP system has many advantages over existing positioning systems such as centimetre scale positioning accuracy for indoor environments and VLP systems can be installed inexpensively since they utilize existing lighting systems with very few modifications applied. VLP systems due to the inherent properties of VLC are better suited in scenarios where RF communication is subject to multipath

fading effects, as visible light is less subject to multipath effects and thus make the propagation of visible light is more predictable. For example, RF communication inappropriate environments (e.g., underwater and underground), where RF signals do not propagate well, which results in disruptive errors. Furthermore, where RF radiations are not permitted (e.g., aeroplanes, hospital magnetic resonance imaging (MRI) and computed tomography (CT) scan rooms) due to electromagnetic interference, VLP systems is a safe choice [25–27].

The existing position estimation algorithms and techniques in VLP systems can be categorized into proximity, fingerprinting, trilateration, and triangulation. These algorithms and techniques are categorized by their use of parameters, including time of arrival (TOA), time difference of arrival (TDOA), received signal strength (RSS), angle of arrival (AOA), phase difference of arrival (PDOA), hybrid (TOA-RSS), hybrid (TDOA-RSS), and hybrid (AOA-RSS) [23–26,26,28–32]. Hybrid systems have also been proposed for indoor positioning based on the two different communication technologies such as VLC and RF [24, 28].

VLP systems performance is evaluated in the literature by calculating the Cramér–Rao lower bound (CRLB), which is the benchmark for providing theoretical limits on position estimation accuracy. CRLB offers a lower bound for the variance of any unbiased estimator [33]. Many studies in the literature have evaluated the theoretical limits of distance and three-dimensional (3D) position estimation of VLC systems [28, 34–43]. The works in [34,36] and [28] calculated the CRLBs for distance and 3D position estimation in synchronous VLC systems using TOA measurements, whereas in [39] performance analysis for the TDOA based technique was carried out. Several works investigated distance and 3D position estimation CRLBs in asynchronous VLC systems using RSS based techniques [28, 35, 37, 41–43]. Moreover, The authors in [28, 40] derived the CRLBs in asynchronous VLP systems for hybrid systems by exploiting RSS and considering TDOA parameters, whereas in [38] RSS and PDOA parameters were considered.

There are many challenges that can affect the positioning estimation accuracy in

VLC systems but are not limited to: 1) The signal-dependent shot noise (SDSN), which is the noise generated by the LED's transmitted signal itself at the VLC photodetector receiver. 2) The thermal noise at the VLC photodetector receiver is cause by operation of the light signal amplifier and the load in the photodetector. 3) The visible light multipath effect, which is caused by reflection, refraction, and scattering from objects such as glass walls or human clothing, so the field of view (FOV) and line of sight (LOS) path requirements are critical for position accuracy at the room edges. 4) Synchronization errors which are caused due to timing bias between LED transmitter and VLC photodetector receiver clocks. There are other challenges such as LED tilt position, limited transmission distance, signal collisions, and mobility issues [16, 17, 25–27].

The review of the existing literature has shown that most VLP system models consider only thermal noise, and it is modeled as additive white Gaussian noise (AWGN) [28, 44]. However, in some system models, either SDSN has been considered alone [34] or a total noise variable is constructed as the sum of thermal noise and shot noise (from background radiation, dark current, and shot noise) [25, 35, 45, 46]. In these cases, approximation forms of thermal noise and shot noise has been used that was derived using the spectrum from long-IR transmission wavelengths [45]. These approximations were also presented in [46], with assumptions of the free-space optical channel with AWGN and Poisson channel where corrupting shot noise depends on the signal. The author in [47], while considering the previous two system models in [46], have chosen to develop a system model that better reflects the physical properties of the VLC system. Where thermal noise is considered as AWGN and the variance of shot noise is dependent on the input signal. The analytical comparison with the other models was also discussed.

The current literature indicates that SDSN has a considerable impact on VLP systems. The effect of SDSN on two-dimensional (2D) positioning (distance) accuracy was studied in [34, 35, 38, 41, 42]. However, these works did not consider the time dependency of the SDSN, instead treating it as AWGN with fixed variance. This does not realistically represent the nature of SDSN. Similarly, no distance estimation technique

addresses the time synchronization problem without requiring multiple LEDs or photodetectors at the VLC transmitter or receiver sides. For instance, in asynchronous VLP systems, the TDOA based technique can be adopted, but it requires at least two LEDs at the transmitter. Time synchronization also remains a requirement between the LED transmitters [25, 26]. The impact of SDSN on the position estimation error bounds has not been well studied and neither has the imperfect synchronization issues between an LED transmitter and VLC photodetector receiver due to clock timing bias, which motivated us to pursue the following objectives:

- Studying the distance and 3D position estimation error bounds when the VLC system is under the effects of the SDSN. We aim to present a comprehensive study where we consider a wide range of estimation techniques, including:
  - TOA based distance estimation for synchronous VLC system.
  - Hybrid (TOA-RSS) based distance estimation for synchronous VLC system.
  - Hybrid (TDOA-RSS) based position estimation for quasi-synchronous VLC system.
  - RSS based distance estimation for asynchronous VLC system.
  - Moreover, we consider synchronous, quasi-synchronous and asynchronous downlink (DL) communications when evaluating the error bounds.
- Mitigating the effects of imperfect synchronization between the transmitter and receiver for the VLP system.

We tackled these objectives by:

- Deriving the theoretical limits on distance and 3D position estimations in a DL VLC system for all mentioned scenarios in the objectives.
- Proposing a bi-directional synchronization protocol that can mitigate the effects of imperfect synchronization between the transmitter and receiver. This protocol

needs only one transmitter and one receiver to determine the distance estimate via up-link (UL) and DL communications between the LED transmitter and photodetector receiver.

- Formulating several simulation scenarios to validate all presented results.

1.2 Thesis Contributions

Compared to the existing literature and motivated by the importance of the thesis topic, the contributions of this work can be summarized as follows:

1. The performance of the VLP systems are evaluated in the literature by calculating the CRLB, which is the benchmark for providing theoretical limits on distance and position estimation accuracy. In this thesis, we studied the effect of SDSN and our results represent a benchmark that should be considered when the system is under the effect of SDSN. In addition, the CRLB analysis in this thesis is valid for any value of SDSN. However, it is not necessary for each estimator to reach this bound, but the designer should be aware of the benchmark performance if the system is affected by SDSN.

2. The VLP system based on distance estimation is studied under the joint effects of SDSN and thermal noise. We consider both synchronous and asynchronous DL communications when evaluating the CRLBs of the distancing error. Performance assessment is based on TOA, RSS, and hybrid (TOA-RSS) based distance estimations.

3. A synchronization protocol is proposed, which can mitigate the effects of timing bias between the LED transmitter and VLC photodetector receiver in bi-directional VLC system in the presence of SDSN and thermal noise.

4. Moreover, an exact expression is derived for the CRLB for a bi-directional distance estimation protocol. This expression can be used as a benchmark to predict and evaluate the performance of the estimators.

5. We investigate the error bounds for 3D position estimation in DL VLC systems. More precisely, we study the joint effect of SDSN and thermal noise on the estimation error bounds. When evaluating the positioning error's CRLBs, we consider synchronous, quasi-synchronous, and asynchronous VLC systems. Performance assessment is based on position estimations by utilizing a combination of information from TOA, TDOA, and RSS related parameters.

1.3 Thesis Outline

The rest of the thesis is organized as follows:

In Chapter 2, we briefly introduce some relevant background on the OWC and the fundamentals of VLC system architecture and applications. We also introduce various types of VLP techniques and parameters used for distance and 3D position estimation. Finally, many factors affecting distance and 3D position estimation accuracy are discussed at the end of the chapter.

In Chapter 3, the VLC system model with time dependent SDSN is presented. Then, comparative theoretical analysis of distance estimation for DL communication systems under the effect of SDSN is carried out by providing error performance benchmarks for the different scenarios.

In Chapter 4, the bi-directional VLC system model under the effect of SDSN is presented. Then, a synchronization protocol is proposed to mitigate the synchronization problem. After that, comparative theoretical analysis of distance estimation for bi-directional communication system under the effect of SDSN is carried out by providing error performance benchmarks.

In Chapter 5, the VLC system model with time dependent SDSN is presented. Then, comparative theoretical analysis of 3D positioning estimation for DL VLP systems under the effect of SDSN is carried out by providing error performance benchmarks for the different scenarios.

In Chapter 6, we offer a summary of our investigation and some important conclusions. We also suggest some potential topics for future research.

1.4 List of Publications

- **Related to the thesis**

  1. Ahmad Cheema, Malek Alsmadi and Salama Ikki, "Distance Estimation Error Performance of Visible Light Communication Under the Effect of Signal-Dependent Noise," *IEEE 32nd Annual International Symposium on Personal, Indoor, and Mobile Radio Communications, (IEEE PIMRC'21)*, Helsinki, Finland, pp. 771–776, 2021.
     I am the main contributor of this work, and I played a leading role in the theoretical modeling and planning of the publication.

  2. Ahmad Cheema, Malek Alsmadi and Salama Ikki, "Distance Estimation in Visible Light Communications: The Case of Imperfect Synchronization and Signal-Dependent Noise," in *IEEE Transactions on Vehicular Technology*, vol. 70, no. 10, pp. 11044–11049, Oct. 2021, doi: 10.1109/TVT.2021.3107808.
     I am the main contributor of this work, and I played a leading role in the theoretical modeling and planning of the publication.

  3. Ahmad Cheema, Malek Alsmadi and Salama Ikki, "Position Estimation Error Performance for Downlink Visible Light Positioning under Signal-Dependent Shot Noise," Submitted, *IEEE Photonics Journal.*
     I am the main contributor of this work, and I played a leading role in the

theoretical modeling and planning of the publication.

- **Unrelated to the thesis**

  1. Ahmad Cheema, Malek Alsmadi and Salama Ikki, "Survey of Identity-Based Attacks Detection Techniques in Wireless Networks Using Received Signal Strength," *2018 IEEE Canadian Conference on Electrical & Computer Engineering (CCECE)*, Quebec City, QC, pp. 1–6, 2018.
     I am the main contributor of this work, I played a leading role writing and planning of the publication.
  2. IEEE International Network Generations Roadmap (INGR), "An IEEE 5G and Beyond Technology Roadmap Security 1st Edition," December 2019.
     I am one of the contributors of this work, I was also the co-chair of the group.
  3. IEEE International Network Generations Roadmap (INGR), "2021 Edition - Security And Privacy An IEEE 5G and Beyond Technology Roadmap."
     I am one of the contributors of this work, as a member of the group.

Chapter 2

Visible Light Communication Literature and Preliminaries

2.1 Introduction

Communication is a basic need for people. We can not imagine a world without the internet, the most popular medium of communication, nowadays. Thanks to the advancement in communication technology we are able to communicate cross-continents with a click. In this age of electronic devices, we explore the universe by communicating and controlling devices over extremely large distances. Wireless communication will still be the predominant method of connectivity for everyone and everything in the not so distant future [48]. As a result, there is an ever-growing demand for higher data rates and bandwidth fuelled by the evolution of technology such as IoT and machine-to-machine communication [48–50]. Currently, existing wireless technology most commonly uses RF communication. However, there is a consensus that the RF spectrum alone will not be enough to meet future needs. This is largely due to overcrowding and increased costs in the RF spectrum [51–53]. Whereas, optical spectrum is available and largely untapped, and still unregulated. Fig. 2.1 shows the optical spectrum, which consists of

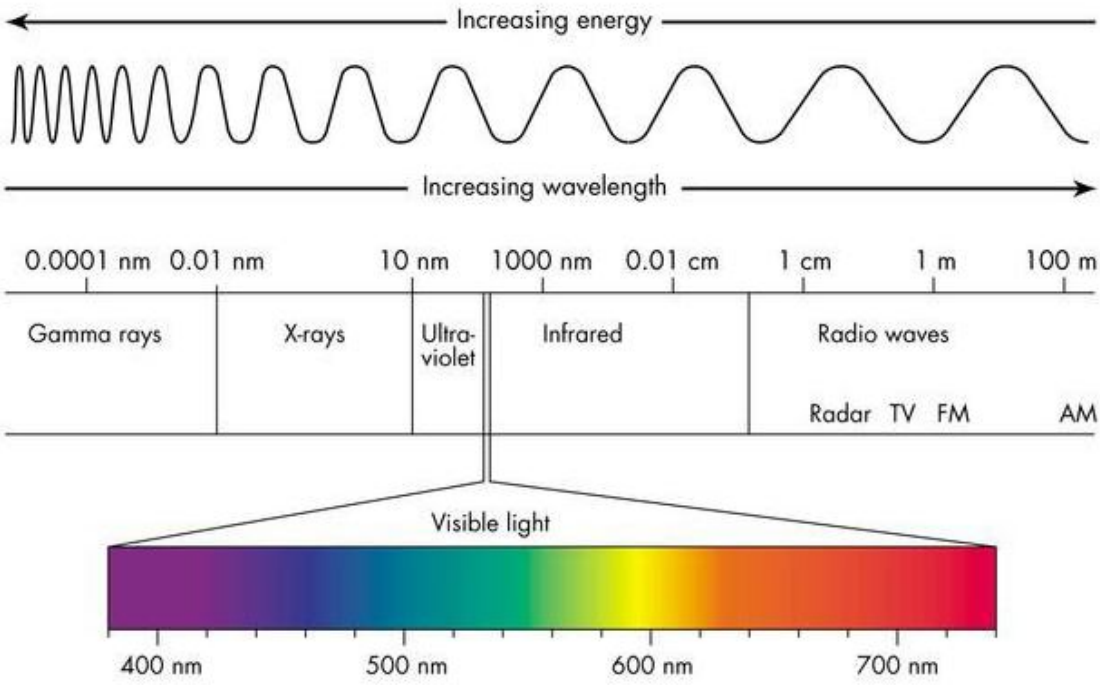

Figure 2.1: The electromagnetic spectrum [54].

IR, visible light, UV, X-rays, and Gamma rays [16, 17, 54, 55]. The optical fiber communication already provides a high data rate utilizing optical spectrum. Therefore, for last mile connectivity and mobile access, it was a natural step to extend the optical fiber medium to include the free-space medium [51]. As a result, there has been a significant interest in OWC technologies from academia and industry. The OWC IR technology was used in second-generation (2G) devices for a short-range high speed wireless digital communication [9, 46]. However, it is expected that OWC will be adopted to meet the vision and demands of the 6G communication system [56–58]. Furthermore, there is a wide range of OWC technologies that can serve many use cases. The OWC technology includes visible light, free-space optical (FSO), light fidelity (Li-Fi), and optical camera communication (OCC) or image-sensor communications [9, 12, 13, 51, 56, 57, 59]. Table

2.1 show a comparison of different OWC technologies.

2.1.1 Free-space Optical Communication

The FSO communication systems are where free space acts as a communication channel between a transmitter and receiver that are in LOS for the successful transmission of optical signals. The communication channel can be space, vacuum, or atmosphere [60–62]. The closest technology to optical fiber communications in terms of functionality is FSO communication. It primarily uses IR wavelength range of the optical spectrum, which can provide static wireless point-to-point communications over relatively large distances of more than 10,000 km. As fiber optic connectivity for fronthaul/backhaul network is sometimes difficult is to be provide due to geographically remote locations, cost-effectiveness, or complexity of the solution. The FSO can be an alternative solution as its data transfer capacities are comparable to optical fiber communication [6, 7, 12, 51, 60–64].

2.1.2 Light-Fidelity

The LOS wireless communication system based on optical radiation, referred to as Li-Fi, was envisioned at the University of Edinburgh. The Li-Fi system is bi-directional, fully connected and high-speed wireless networking with light, which is analogous to well-known WLAN or wireless fidelity (Wi-Fi). It supports multi-user communication with point to multi point and multi point to point communication. A wireless network can be built utilizing multiple Li-Fi access points with seamless handover between very small optical attocells. The Li-Fi technology is complimentary to existing technologies such as IEEE 802.11 WLAN and 802.15 wireless personal area network (WPAN) [9,13,19,65,66].

Table 2.1: Comparison of different OWC technologies.

Technology	FSO	Li-Fi	OCC	VLC
Standard	IOAG.T.OLSG.2012.V1A, ITU-R P.1814-0, and ITU-R P.1817-1	IEEE 802.15.11 LC SG	IEEE 802.15.7m	IEEE 802.15.7, JEITA CP-1223, and ITU-T G.9961
Transmitter	Laser	LED/LD	LED/screen	LED/LD
Receiver	Photodiode/Avalanche-Photodiode	Photodiode	Camera/Image-Sensor	photodiode/avalanche-photodiode/positive-intrinsic-negative diode/camera
Spectrum	IR/Visible Light/UV	IR/Visible Light/UV	IR/Visible Light	Visible Light
Modulation	OOK, IM, PM, OFDM, OAM *	OOK, IM, OFDM, CSK *	OOK, IM, PM, OFDM, CSK *	OOK, IM, PM, OFDM, CSK *
Data rate	∼Gbps	Kbps∼Gbps	bps∼Mbps	Mbps∼Gbps
Distance	>1 km	< 10 m	<100 m	<100 m
Implementation complexity	Moderate	Low	High	Low
Additional function(s)	–	Illumination	Imaging, Localization	Illumination, Localization
Limitations	Sensitive to weather and turbulence	Limited use in outdoor, Limited range	Low data rate	Illumination constraints, Limited range

* **OOK** = ON-OFF keying; **IM** = intensity modulation; **PM** = pulse modulation; **OFDM** = orthogonal frequency division multiplexing; **OAM** = orbital angular momentum multiplexing; **CSK** = color-shift keying;

2.1.3 Optical Camera Communication

The OCC or image-sensor communication (ISC) is similar to other OWC technologies when it comes to the transmitter side, but with a significant difference at the receiver side. The transmitter in the OCC system can be a low rate lighting source such as liquid crystal display (LCD) or a high rate light source such as LED [67]. In OCC, a camera or an image sensor from a webcam, smartphone camera or digital camera is used as a receiver [68]. A camera or an image sensor typically comprises of a 2D array of photodiodes to convert the captured incident light into an array of electrical signals [69]. The camera can operate in global-shutter or rolling-shutter modes with two different sensor technologies, complementary metal oxide semiconductor (CMOS) or charge coupled device (CCD) to capture images digitally.

2.2 Visible Light Communication

The history of VLC dates back to the 1880s when Alexander Graham Bell did the first wireless transmission by inventing the photophone that modulated sunlight over several hundred meters and succeeded in transmitting speech [9]. This pre-dates the transmission of speech by radio. The concept of VLC was proposed again in 1998 when the first white-light LEDs were marketed [9, 70]. A VLC application for wireless audio signal transmission using white LEDs was presented in [71].

There are many factors that pushed the research into VLC such as the very high achievable data rates, ease of deployment, scalability, and immunity to EMI. The visible light spectrum is shown in Fig. 2.1 [6, 16, 17, 54, 55]. The wavelength decreases along the optical spectrum while the frequency and energy increase. VLC utilizes wavelength in the range from 380 to 750 nanometer with a corresponding frequency band of 790 to 430 terahertz. In comparison, radio wave occupies wavelengths between 1 mm and 100 km with a corresponding frequency band of 300 GHz to 3 KHz [6, 18, 72].

2.2.1 VLC Technology Standards

VLC technology standards address many issues that are related to VLC device classification, physical layer and medium access control (MAC) sublayer characteristics such network topologies, architecture, visibility support, flickering, dimming, addressing, acknowledgment, performance, quality indication, collision avoidance, colored status indication, color stabilization and security specifications [16, 17, 53, 73]. There are many organization bodies that are working on standardizing VLC. Next, we discuss some of the standardization work done by these organizations till date.

In 2003, the Visible Light Communication Consortium (VLCC) was founded in Japan by Professor Masao Nakagawa of Keio University to publicize and standardize the VLC technology [74]. A few years later the Japan Electronics and Information Technology Industries Association (JEITA) operationalized multiple standards CP-1221 and CP-1222 in 2007, and CP-1223 in 2013 [16,17,73]. These standards cover the basics of VLC systems, visible light ID systems and visible light beacon systems, respectively [75–77]. In 2014, the Visible Light Communication Association (VLCA) was established, which is the successor to VLCC [78].

The Institute of Electrical and Electronics Engineers (IEEE) recognized the potential of VLC technology and created IEEE 802.15 WPAN Task Group 7 back in 2009 [79]. Since then, the IEEE 802.15 working group has approved two iterations, IEEE 802.15.7-2011 [80] and IEEE 802.15.7-2018 [81]. This VLC standard mainly covers the physical layer and MAC sublayer for short-range, which guarantees data rates sufficient to support audio and video multimedia services [16,17,73,80,81]. Then, there is the "Multi-Gigabit per Second OWC" project undertaken by the IEEE 802.15.13 Task Group. Other recent activities include the Vehicular Assistant Technology (VAT) interest group under the IEEE 802.15 working group, which has published multiple reports on use of visible light as a mode of communication option [82]. Furthermore, the Light Communication interest group under the IEEE 802.11 working group aims to determine the technical

and economic opportunities presented by using light as a medium for wireless communications [83].

The International Telecommunication Union Radiocommunication Sector (ITU-R) working group 15 on spectrum management published reports to understand the distinctive characteristics of VLC, and how and up to what extent VLC for broadband communications can help to ease the congestion in the radio spectrum. The reports also looks into efficiency, interference, health risks, and cybersecurity related use of VLC along with barriers to new application development, implementation and interoperability with current communication systems [11,84]. In addition, the International Telecommunication Union Telecommunication Standardization (ITU-T) released the ITU-T G.9961 standard in March 2019, which specifies the system architecture, physical layer and data link layer (DLL) for high-speed indoor OWC transceivers using visible light [85]. The ITU-T G.9961 standard is derived from the ITU-T G.9960: which is the standard for "Unified high-speed wireline-based home networking transceivers - System architecture and physical layer specification" [86].

2.2.2 Network Architecture and Topologies

In IEEE standards, the architecture for VLC networks has been defined as illustrated in Fig. 2.2. Each lower layer offers service to the layer above. The optical service access point (SAP) consists of light sources or cells which are connected to the physical layer through a physical layer switch (PHY-switch). The VLC system devices are classified as a infrastructure, mobile, or vehicular network architecture. Table 2.2 summarizes the characteristics of each class.

The physical layer and MAC sublayer exchange data through physical layer data (PD) and MAC common-part sublayer (MCPS) SAPs. Similarly, the management information is exchanged using physical layer management entity (PLME) and MAC layer management entity (MLME) SAPs, respectively. The MCPS in MAC sublayers interface

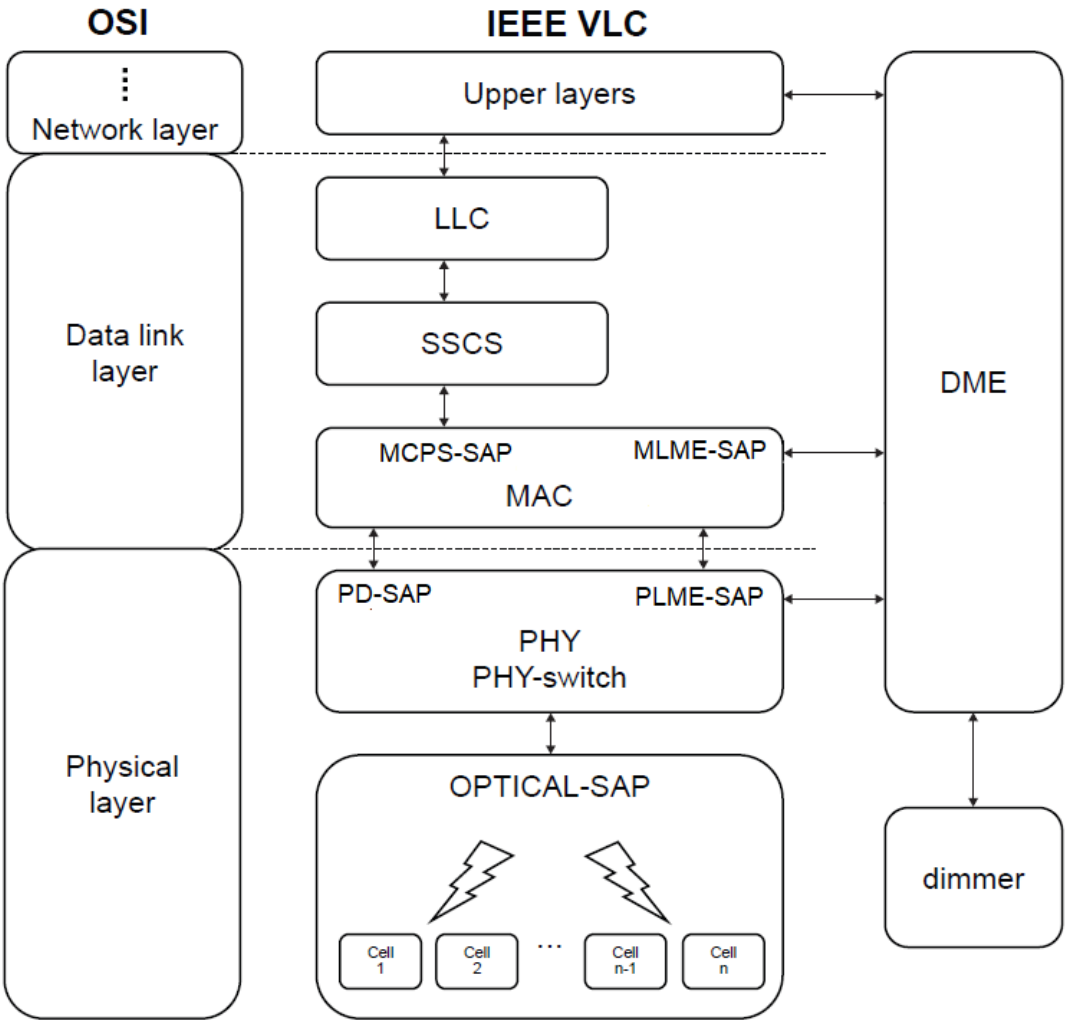

Figure 2.2: IEEE VLC network architecture, adopted from [73].

with service-specific convergence sublayer (SSCS) to provide access to logical link control (LLC). The upper layers are not defined in the standard as they are application and vendor specific. The light source dimmer interfaces with the system at different layers' level through device management entity (DME). It can provide dimming information to the physical layer and MAC sublayer by accessing certain dimmer related attributes from the PLME and MLME SAPs [13, 80].

The IEEE standard categorizes VLC personal area network (VPAN) into three dif-

Table 2.2: IEEE VLC device classification, adopted from [13, 80].

	Infrastructure	**Mobile**	**Vehicle**
Fixed Coordinator	Yes	No	No
Form Factor	Unconstrained	Constrained	Unconstrained
Power Supply	Ample	Limited	Moderate
Light Source	Intense	Weak	Intense
Physical Mobility	No	Yes	Yes
Range	Short/Long	Short	Long
Data Rates	High/Low	High	Low

ferent network topologies based on the intended applications. The basic structure of each network topology (peer-to-peer, star, and broadcast) is illustrated in Fig. 2.3, along with visibility support for all topologies to maintain illumination and mitigate flickering. In each topology, there is a coordinator device and an end user device. The devices in star and broadcast topologies are associated with a single central coordinator that acts like an access point, which is responsible for device association in the network. In peer-to-peer and star topologies, a unique 64-bit destination address is required for bi-directional communication. The devices associated with a coordinator are allowed to have a shortened 16-bit address. Whereas broadcast topology, as it is directional communication, does not require destination addresses [13, 80].

The ITU-T G.9991 standard for VLC has defined the network architecture reference model for VLC as presented in Fig. 2.4. There are multiple reference points namely medium-dependent interface (MDI), physical medium-independent interface (PMI), and application interface (A-interface). The MDI physical interface is where physical signals transmitted over a specific transmission medium and mechanical connection between physical layer and the underlying medium. The reference model adopts physical layer I (PHY I) and physical layer II (PHY II), which are defined for different scenarios. PHY II based on asymmetrically clipped optical orthogonal frequency division multiplexing

(OFDM)is designed for VLC and PHY I based on OFDM adopts the ITU-T G.9960 standard. The physical layer functionalities (e.g., modulation/demodulation, encoding, and data rate) are responsibilities of the physical medium dependent (PMD) sublayer, physical medium attachment (PMA) sublayer, and physical coding sublayer (PCS). The physical layers frames are mapped to MAC protocol data units through the PMI to common the DLL. The PMI is application independent, medium independent, and is responsible for logical signals and functional flows. The DLL has three sublayers: MAC, LLC, and application protocol convergence (APC). The A-interface is described in terms of primitives exchanged between the DLL and the application entity (AE) of the network layer [85, 86].

In ITU-T standards, VLC transmission medium consists of transceiver nodes (which can extend some capabilities of a domain master), and a relaying node. A transmission network consists of a global master, domain masters, and/or nodes. A domain comprises of a domain master and may contain one or more nodes that are connected with it via optical wireless medium i.e., visible light, IR and UV. The ITU-T standards support multiple VLC network topologies as illustrated in Fig. 2.5. They can use any topology depending on the application. Two domains can be connected via a bridge. Domain that do not use visible light as medium of communication is called an alien domain (e.g., PLC, Ethernet/local area network (LAN), and WLAN). A network is made up of many resources such as bandwidth reservations, handover between domains, and operational characteristics between domains are handled by the global master function [85].

2.2.3 IEEE VLC Physical Layer

In general, the physical layer carries the main features of VLC technology. It is the responsibility of the physical layer to transmit data using visible light as communication medium/channel. The physical layer in VLC standards differs significantly from RF standards. VLC uses intensity modulation (IM)/direct detection (DD), a real and

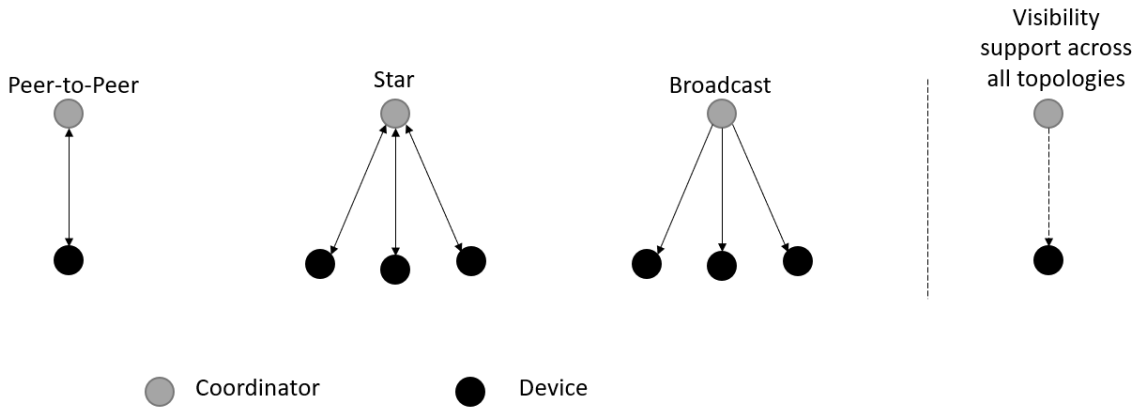

Figure 2.3: IEEE VLC network topologies, adopted from [13, 80].

positive (unipolar) valued signal needs to be produced. Therefore, the conventional modulation schemes used in RF communications should be modified in order to achieve a real valued output signal [18]. The visible light characteristics play an important role in determining components related to signal and channel such as path loss, lightwave propagation, noise, light modulations and coding mechanisms in the VLC systems [16,17,73].

The physical layer in the IEEE standard for VLC defined the relation between the medium and the user device along with device specification and classification [13, 80]. The physical layer has to perform multiple tasks in order for a transceiver to establish or terminate a physical communication link such as transceiver activation and deactivation, channel selection, synchronization between devices, data (bits) transmission and reception, wavelength quality indication for the received frames and error correction [13, 73, 80]. There are six different types of physical layers defined depending upon the implementation environment and transmission data rate. VLC use physical layer types I, II and III. Table 2.3 summarizes the environment classifications and their settings of operating modes. However, the rest of the physical layer types IV, V and VI are defined for OCC only.

Fig. 2.6 shows the physical layer block diagram for the IEEE VLC standard. Initially, at the transmitter side, the input bitstream is passed through a channel encoder to add

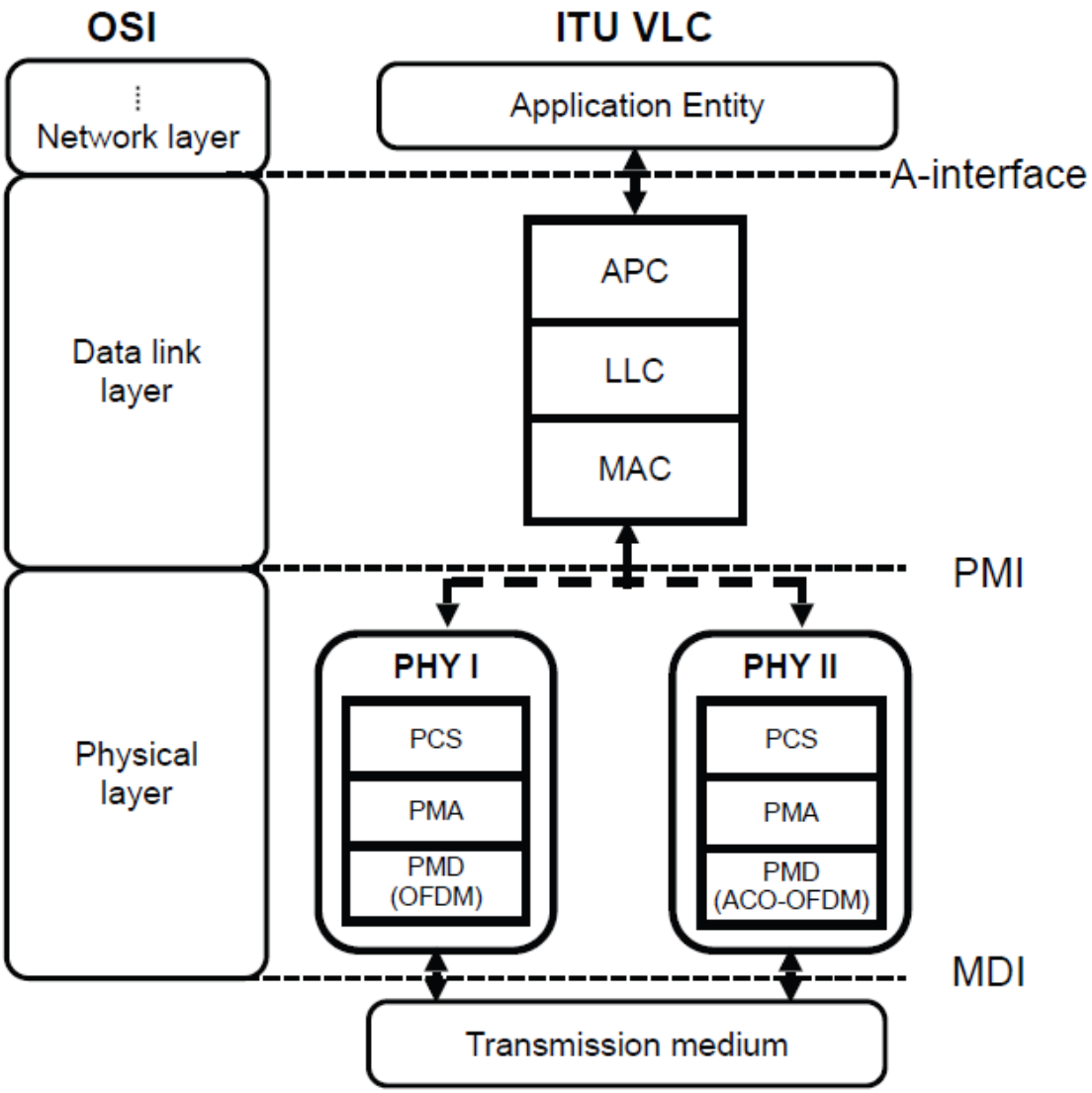

Figure 2.4: IUT-T VLC network architecture, adopted from [73].

controlled redundancy (e.g., parity bits) so that any transmission error (caused due to path loss or interference introduced by optical noise) can be fixed. The bitstream may be protected by a forward error-correction (FEC) encoder. There are various FEC coding schemes such as Reed-Solomon (RS) and convolutional code (CC), which are supported by the IEEE standard depending upon application environments such as indoor or outdoor, low or high data rate, and short or long length of frames. An output

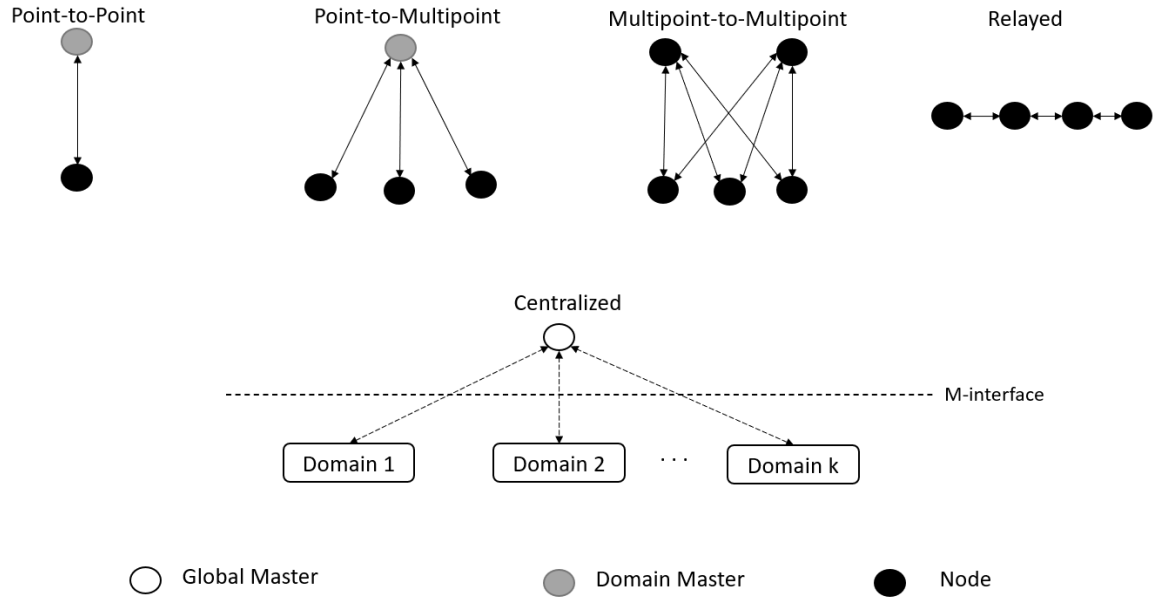

Figure 2.5: IUT-T VLC network topologies, adopted from [85].

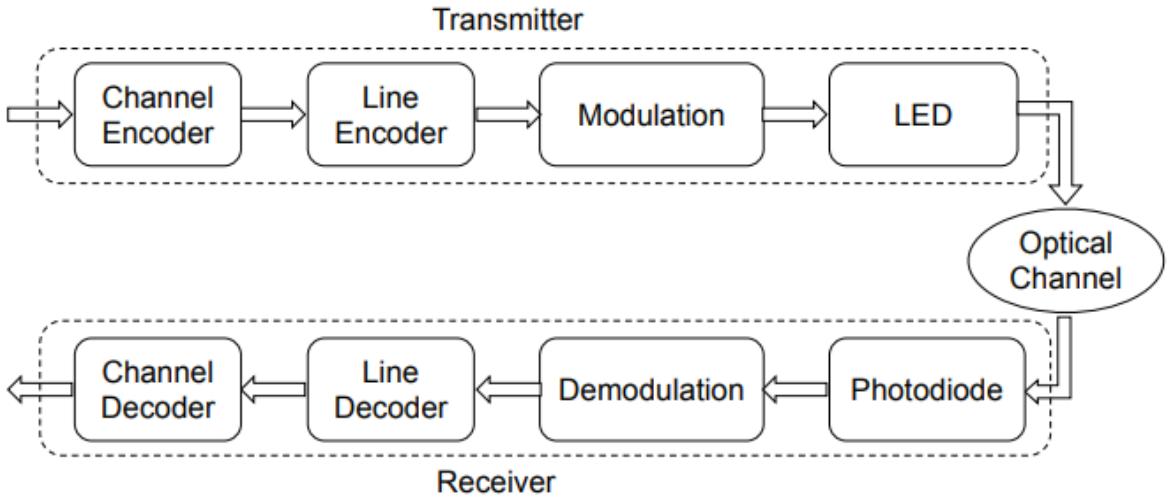

Figure 2.6: IEEE model for VLC physical layer, adopted from [73].

long runs of 1s and 0s from the channel encoder results in direct current (DC) unbalance, which causes flickering. In order to mitigate flickering and to provide DC balance and clock recovery, data symbols from the channel encoder are inserted into the run length limited (RLL) line encoder to gain an equal number of 1s and 0s for each symbol. The most common RLL line codes are Manchester, Half-rate code, 4B6B, and 8B10B codes.

Table 2.3: IEEE physical layer classification and operating modes, adopted from [13, 73].

PHY types	**Environment**	**Modulation**	**RLL code**	**Optical clock rate (Hz)**	**FEC codes**		**Data rate (bps)**
					(RS)	**[CC]**	
PHY I	Outdoor	OOK	Manchester	200k	(15,7)	1/4	11.67k
					(15,11)	1/3	24.44k
					(15,11)	2/3	48.89k
					(15,11)		73.3k
					None		100k
		VPPM	4B6B	400k	(15,2)		35.56
					(15,4)		71.11k
					(15,7)		124.4k
					None		266.6k
PHY II	Indoor	VPPM	4B6B	3.75M	(64,32)		1.25M
					(160,128)		2M
				7.5M	(64,32)		2.5M
					(160,128)		4M
					None		5M
		OOK	8B10B	15M	(64,32)		6M
					(160,128)		9.6M
				30M	(64,32)		12M
					(160,128)		19.2M
				60M	(64,32)		24M
					(160,128)		38.4M
				120M	(64,32)		48M
					(160,128)		76.8M
					None		96M
PHY III	Application with multiple transceivers	4-CSK	None	12M	(64,32)		12M
		8-CSK			(64,32)		18M
		4-CSK		24M	(64,32)		24M
		8-CSK			(64,32)		36M
		16-CSK			(64,32)		48M
		8-CSK			None		72M
		16-CSK			None		96M

PHY = physical layer ; **OOK** = ON-OFF keying; **VPPM** = variable pulse position modulation; **CSK** = color-shift keying;

Each physical layer type uses specific RLL line codes except physical layer type III, which does not use any line code as shown in the Table 2.3 [13, 73].

The line encoder converts this digital data to electrical signals. After line encoding, modulation is performed. The conventional modulated signals are bipolar. In VLC, photodector can only detect the amplitude of the signal not the phase at the receiver side. Therefore, signal conversion is required. TheLED transmitter side needs to produce a real and positive (unipolar) valued signal. All subcarriers are modulated with a high-enough frequency to be imperceptible to the human eye. However, a positive DC is added to make signal unipolar. The IEEE standard for VLC supports many modulation

schemes, including ON-OFF keying (OOK), variable pulse position modulation (VPPM), color-shift keying (CSK), mirror pulse modulation (MPM), frequency shift keying (FSK), phase shift keying (PSK) and others depending upon the underlying the physical layer types [13, 80].

The simplest modulation scheme is OOK, where the LEDs are either turned on or off depending on data bits being 1 or 0. Another way to represent 1 or 0 OOK is to make the intensity of the light distinguished such as 1 representing high intensity of light and 0 as low intensity light [13, 55, 59]. The VPPM uses binary pulse-position modulation (PPM) for communication and the pulse width modulation (PWM) for dimming control [55, 59, 87]. This scheme changes the duty cycle of each optical symbol to encode bits to support illumination with dimming control and communication simultaneously [55]. The CSK is a VLC IM scheme that encodes the bit patterns into color (wavelength) combinations [55, 59, 88]. A great deal of work has been done in literature to develop new or improving existing modulation schemes such as OFDM, spatial modulation (SM), and spatial multiplexing (SP) for increasing data rates [13, 16, 17, 55, 59].

Finally, the modulated electrical signal is fed to the LED, which acts as a transmitter and transmits data through the optical channel. LEDs are able to generate light due to semiconductor material properties which permit electroluminescence. The particular semiconductors used for LED manufacturing are gallium arsenide, gallium phosphide, or gallium arsenide phosphide. The phenomenon referred to as electroluminescence is the emission of photons when electric current passes through semiconductors having electron holes. The light is emitted in the visible spectrum corresponding to a specific color [16, 17, 89].

At the receiver side, the light signals are absorbed by the VLC photodetector (also referred as a light sensor or a photodiode), which acts as a receiver. The photodetector is a semiconductor diode that receives optical signals (photons) and converts them into electrical signals, via the photoelectric effect internally [59]. In VLC the type of photodetector used are p-type and n-type (PN) photodiode; p-type, intrinsic, and n-type

(PIN) photodiode; or avalanche photodiode (APD) [20]. The resulting electrical signal is passed on for demodulation and then through a line decoder. The decoded bitstream is then passed through a channel decoder to generate the output bitstream. Any errors can then be detected and corrected at the receiving end using a FEC channel decoder [73].

2.2.4 IEEE VLC Medium Access Control Sublayer

In the IEEE standard, MAC sublayer provides an interface between the physical and upper layers. It is designed mainly to provide data and management services through two SAPs as illustrated in Fig. 2.2. The MAC sublayer provides a reliable link protocol between two peer MAC entities with the following functionalities: a) Beacon management as a coordinator device; b) Mechanism for channel access with or without guaranteed time slot allocation and management; c) Synchronization to network beacons; d) Successful frame reception and data verification using delivery acknowledgment and cyclic redundancy check (CRC); e) To support device association and disassociation; f) To provide device security; g) To support visibility, color function and dimming support to maintain illumination and mitigate flicker; h) To provide a visual indication of device channel quality and status; i) To support mobility [13, 73, 80].

In general, for multiple access mechanisms VLC consider the adoption of the following approaches: 1) time-division multiple access (TDMA) 2) carrier sense multiple access (CSMA) 3) carrier sense multiple access/collision avoidance (CSMA/CA) 4) frequency-division multiple access (FDMA) 5) orthogonal frequency division multiple access (OFDMA) 6) code division multiple access (CDMA) 7) space division multiple access (SDMA) and 8) non-orthogonal multiple access (NOMA) [13, 17]. The IEEE standard depending upon the application and network configurations provides different random channel access mechanisms [13]. They are as define below

- **Slotted random access:** is used in beacon-enable network topology where devices wishes to transfer data to and from the coordinator.

- **Unslotted random access:** is used in nonbeacon-enable network topology where devices wishes to transfer data to and from the coordinator.

- **Slotted/Unslotted random access with CSMA/CA:** can optionally be used with slotted or unslotted random access mechanisms if the devices are using the same spectrum and within the coverage of each other. In this case each device need to ensure that the channel is not used by another device to avoid collision by performing a channel clear assessment.

- **Unslotted ALOHA:** is used when there is no beacon and transmitter has a packet to send, it just send it. Some physical layer types depending upon the transmitter schemes use this access mechanism.

2.3 Visible Light Communication for 6G

The VLC is a disruptive form of wireless communication and is anticipated to be a key player among emerging technologies, especially when it comes to meeting 6G communication system requirements [90]. It is one of the candidate technologies that can meet the 6G service requirements of 1) ubiquitous mobile ultra-broadband 2) ultra-high speed with low latency communication 3) massive machine-type communication and 4) ultra-high data density [91]. There are number of important factors that has driven research into VLC for 6G systems [6–10, 92, 93]. First and foremost is the scalability and ease of deployment due to the low cost, as LEDs are readily available and fairly cheap these days [20, 55]. VLC is an affordable candidate to providing energy efficient communication system and to deal with the RF spectrum crunch [53].

Table 2.4 states some advantages and disadvantages in this regards. The VLC system can have support bandwidth in 100's of MHz, due to which it reach data rates in the Mbps to Gbps range [20, 94, 95]. A VLC system is 100 times faster than average Wi-Fi [96]. It can support high data density in Gbps, as you can place multiple VLC

Table 2.4: Summary of VLC advantages and disadvantages.

Advantages	**Disadvantages**
High bandwidth	Mostly Line of sight (LOS)
High data rate	Limited transmission range
High data density	Susceptibility to interference
Low latency	
Security	
Usable in RF-inappropriate Environments	
Scalable	

transmitters in a single room [97]. By combining multiple transmitters in the VLC system you can increase the data density in a vicinity/proximity [98, 99]. In comparison a single Wi-Fi is placed in a room whose bandwidth is shared among the users. A VLC system has low latency (as the signal travels at the speed of light (milliseconds) but the latency of a full system from end to end depends upon the environment [90, 100].

The optical channel provides some security due to inherent properties of light not being able to pass through opaque materials (e.g., an attacker cannot eavesdrop from behind a wall) [101–103]. The VLC systems are usable in RF-inappropriate environments (e.g., underground mines, healthcare, aeroplanes). Last but not the least VLC infrastructure is scalable, due to the abundance of artificial light resources such as LED lights. However, there are some limitations such as current VLC systems are mostly static in nature with LOS dependencies for better performance. They have a limited transmission range and are susceptible to interference from ambient light sources (e.g., reflection from surfaces, sunlight) [16, 17, 20].

2.4 Visible Light Communication Applications

The idea behind VLC is to provide lighting and communication at the same time. The applications include indoor WLAN, positioning and localization, underwater communications, underground mine communications, V2X communication, and hybrid communication (e.g., RF-VLC, PLC-VLC) [22, 53, 59, 93, 93, 104, 105]. Fig. 2.7 illustrates some of the scenarios where VLC can be deployed.

Nowadays most building illumination infrastructures are equipped with LED bulbs, which can support high throughput for WLAN applications. For example, connected smart home appliances, streaming applications requiring extreme download speeds, retail store applications (e.g., customer tracking), and in shopping malls or exhibitions centers advertisements or marketing information can directly be sent to you handheld mobile device [16, 17, 103, 106, 107]. This will help in alleviating the crowded RF spectrum in WLAN scenarios [73].

In healthcare facilities, it is a well known that RF communications interfere with health care equipment (e.g., MRIs, CT scans, and electrocardiographs) due to EMI phenomena [108, 109]. Similarly, in the aviation sector due to flight safety reasons, all equipment using RF communication is to be switched to aeroplane mode or turned off for the duration of the flight. There are some aeroplanes that are equipped to provide in-flight internet service using Wi-Fi or aircraft-to-earth communication technology. In such cases where equipment that is sensitive to RF spectrum, the VLC systems can be deployed to provide connectivity with higher data rate [59, 108, 109].

The automobiles and traffic lights widely use LED lights. The use of VLC in transport and vehicular systems scenarios such as vehicle-to-vehicle (V2V), vehicle-to-infrastructure (V2I), and infrastructure-to-vehicle (I2V) is advantageous because implementation is low cost due to existing lighting infrastructure and less complex in comparison to RF systems [17,90,110]. Moreover, in underwater and underground environments, RF presents many challenges (e.g., fading, high attenuation) and therefore not suitable.

Figure 2.7: VLC systems applications.

The VLC systems are suitable candidate to fulfill the connectivity requirements in these environments [16, 17, 19, 59, 93].

2.5 Visible Light Positioning

The term positioning and localization refers to realizing an object's position and location in an indoor or outdoor environment using a variety of technologies and techniques. In that context, positioning is an object's coordinates and localization is to find where an object is on the map. There are number of technologies such as GPS, RF communication, and VLC that can be utilized for to locate an object.

There are navigation-based services that depend upon positioning systems. For example, GPS is the gold standard, which provides real-time positioning and navigation

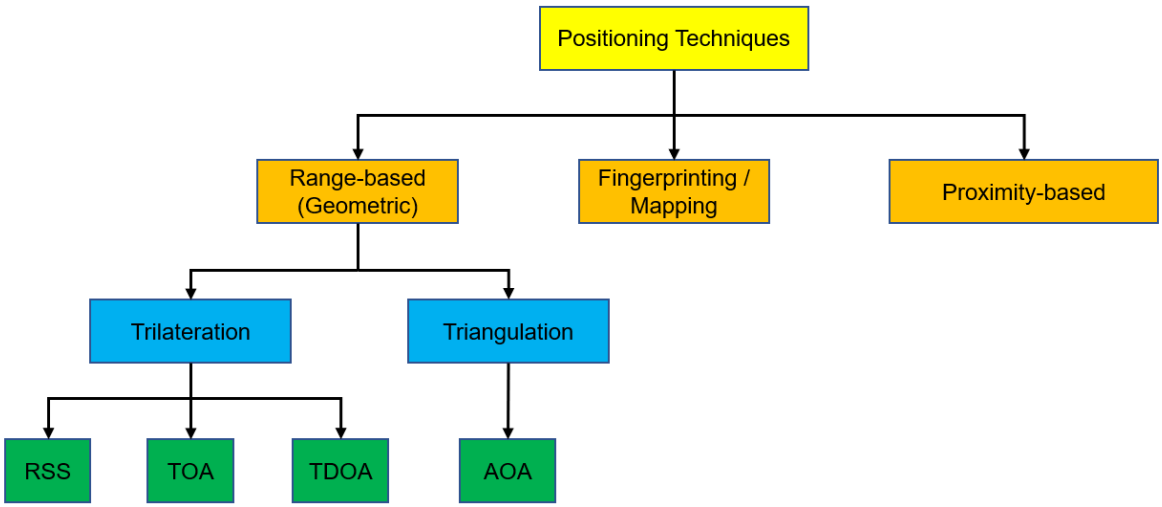

Figure 2.8: VLP techniques.

services on daily basis. The GPS accuracy depends upon the signals received from the satellites. However, GPS services are not available in environments such as indoors, underground, underwater, and mountain terrain. Moreover, the service is interrupted and degraded due to any obstructions such as ceilings, walls, or even cloudy weather [25, 28]. There are applications, which require sub-meter accuracy to locate the object, especially in indoor environments. The RF technology based positioning systems (e.g., Wi-Fi, Bluetooth, radio frequency identification (RFID)) have been a popular choice [111–114]. However, as mentioned earlier there are many issues with RF communication systems and VLC systems are a possible alternative having numerous advantages.

VLP systems are based on VLC technology, which aims to estimate the photodetector receiver's location by utilizing a pilot signal transmitted by the LED transmitters at fixed known positions (reference points/landmarks). These VLP systems provide a low-cost and accurate viable alternative to RF-based positioning systems. Furthermore, VLP systems have shown better localization accuracy. There are applications such as asset tracking, location-aware services, and autonomous vehicles that can utilize VLP systems [23–26, 26, 28–31, 93].

Fig. 2.8 shows most common types of VLC-based positioning techniques. The proximity-based approach provides positioning information in relation to a specific area of the localization environment. It depends simply on connectivity information and is easy to implement. For example, an object (photodetector receiver) that we need to locate the signals from LED transmitters with a known locations, the object is considered near (proximate) to the LED transmitter with the strongest RSS value in comparison to others. These proximity algorithms have been used to provide semantic localization using IR, RFID and Bluetooth technologies. The accuracy of this approach depends upon how dense the LEDs are deployed in the area [25, 26, 44].

The fingerprinting/mapping method consist of positioning techniques, estimating the relative position by matching online measured data with offline pre-measured location-related data. In the offline stage, a map is generated by sampling the location related data using fingerprint (e.g., RSS is considered a type of fingerprint) at each place in the environment is collected. In the online or run-time stage, the currently observed signal strength is matched to the previously collected dataset (map) to estimate the relative position of the object [23, 24, 30].

The geometric properties of triangles are used in range-based approaches, which requires distance or angle measurements between LED transmitters and a photodetector receiver. The distance can be measured using trilateration method, which estimates the receiver's location based on the pilot signals transmitted from at least three LED transmitters from non-collinear fixed positions using RSS, TOA, or TDOA parameters [24–26, 28, 30, 115–117].

The triangulation method can also be used to estimate the receiver's location based on first estimating AOA information from the transmitted signal by at least two LED transmitters at non-collinear fixed positions. Fig. 2.9 and Fig. 2.10 illustrate trilateration and triangulation, respectively. Both methods require a LOS (direct path) between the transmitters and receiver [24–26, 28, 30, 116].

The existing distance and 3D positioning estimation algorithms and techniques in

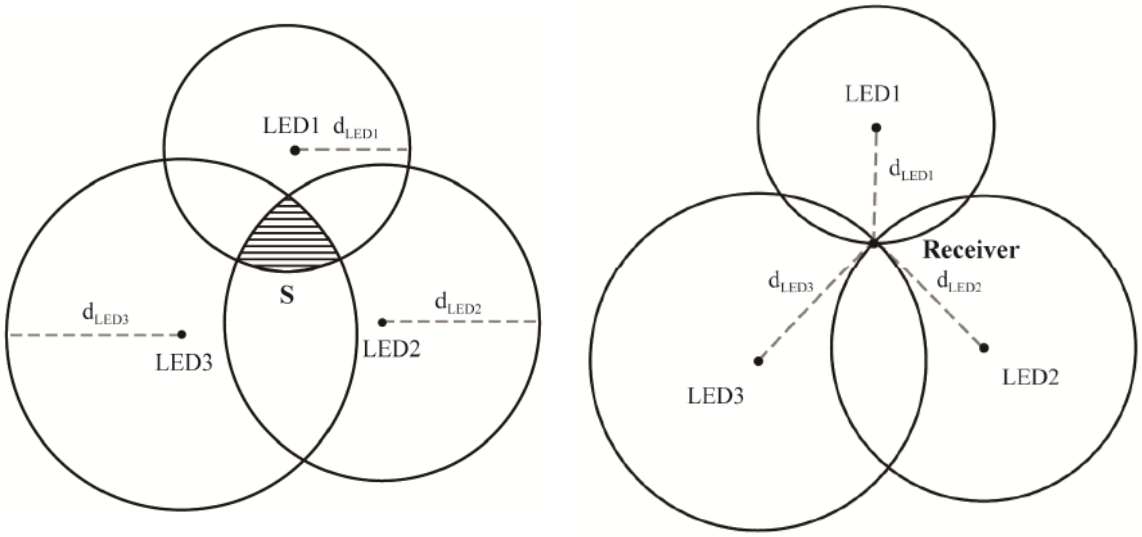

(a) Area (b) Point

Figure 2.9: Trilateration method, adopted from [25].

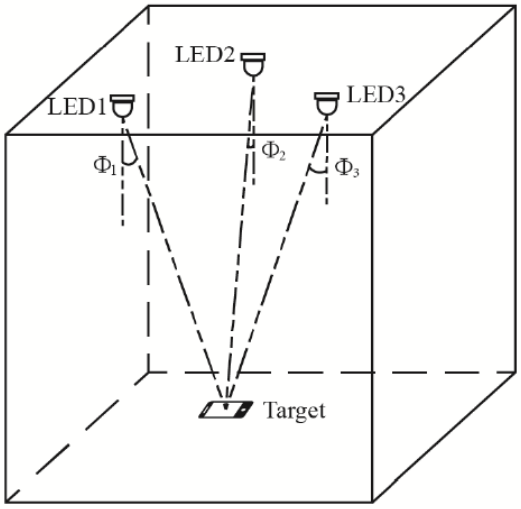

Figure 2.10: Triangulation method, adopted from [25].

VLP systems use various parameters including TOA, TDOA, RSS, AOA, PDOA, hybrid (TOA-RSS), hybrid (TDOA-RSS), and hybrid (AOA-RSS) [23–26, 26, 28–32]. From these, we are only discussing the following,

- **TOA:** is calculated using the velocity of the LED's transmitted signal and mea-

sures the traveled time to photodetector receiver to estimate the distance.

- **TDOA:** follows a similar approach but determines the difference of arrival time (from different LED transmitters with respect to the photodetector receiver) and requires synchronization between the transmitters.
- **RSS:** using the attribute, the attenuation of signal as it travels from the LED transmitter to the photodetector receiver is employed to indicate the distance between them.
- **Hybrid:** is combination of the above distance and 3D position estimation techniques.

As our work in this dissertation is related to them.

2.6 Factors Affecting VLP Accuracy

VLP systems have many challenges that can affect the positioning accuracy or localization error [25, 118, 119]. Some of them are mentioned below:

- Thermal noise: is the noise generated from random motions of electrons. The photodetector may have resistance which can contribute to thermal noise but often the largest contribution to thermal noise comes from the amplifier connected to the photodetector.
- SDSN: is the noise generated by the LED's transmitted signal itself due to the random nature of photon emission.
- Synchronization error: is due to timing bias between transmitter and receiver clocks.
- Ambient light noise: intense ambient optical radiation arising from sunlight, incandescent or fluorescent lamps, or other sources.

- LED tilt: is induced via the LED die placement and packaging. Another important source of tilt is when the operator suspended the LED light fixture. They causes lateral deviation in the receiver plane.

- Mobility: effects the distance estimation because received power varies significantly due to the motion of the object or user.

- Non LOS interference: in VLC is basically, reflection of visible light of the reflective material object (e.g., glass, clothes, paper) which are present in the environment.

2.7 Noise in VLC system

VLP system performance degrades due to the presence of noise in the underlying VLC. There are many noise sources often encounterted in connection with photodetectors. In this thesis, we mainly focus on thermal noise and SDSN, as they are the dominant ones that contribute to distance and 3D positioning estimation error.

- **Thermal noise**: is caused when the photodetector receiver is in use. The temperature of the photodetector receiver electric circuit rises due to the current fluctuation (increase or fall of the voltage in conductors and semiconductors) because the electrons in the conductor do irregular thermal motion in the absence of an external field. The number of free electrons or charge carriers moving in two opposite directions is not equal [25, 119, 120].

- **SDSN**: is mainly due to two reasons. Firstly, it is generated by the ambient light in the photodetector's PIN tube. Secondly, the LED transmitters themselves generate the SDSN. There are many possible sources of ambient light such as sunlight or artificial lights (e.g., incandescent lamps and fluorescent lamps) other than the LED transmitter. The ambient light from these sources is inevitably received by the photodetector receiver, which increases the level of shot noise in

the receiver, since shot noise is non-linear resulting in background current. Most of the VLP systems operate in presence of high ambient levels. Moreover, the interference of modulated visible lights that cannot be filtered results in the noise in the photodetector receiver. As the LED light is controlled by the bias voltage, there is a small amount of power output even at a low level which may result in the noise in the VLC photodetector receiver. In literature, the SDSN is often referred as additive white noise [119–123].

Chapter 3

The Effect of Signal-Dependent Noise on Distance Estimation Error Performance

3.1 Introduction and Related Works

The OWC is an enabling technology for 6G and beyond communication networks [6]. This technology encompasses VLC, Li-Fi, FSO communication, and OCC. OWC uses optically transparent media to transmit data over optical links. The spectra used for signal propagation include IR, visible as well as UV radiations [6–8].

The optical nature of the transmission medium allows for spatial re-utilization and protection from RF co-channel and inter-symbol interference, thus alleviating the current spectrum crunch in wireless communication. Furthermore, with its physical layer's inherent properties, the OWC spectrum provides secure communication, however at the cost of range limitations since light cannot pass through opaque materials [7]. Another key feature is the potential support for infrastructure, mobile, aerial, and vehicular network topologies. Nonetheless, the primary benefits include ultra-high bandwidth in an

unregulated license-free spectrum, ultra-high data rate, and ultra-low latency [6–8].

6G communication technology is expected to implement LED based VLC systems, where LEDs can function as transmitters and photodetectors as receivers [6, 7]. The visible spectrum wavelength ranges from 380 to 750 nanometer, and the corresponding frequency range is 790 to 430 terahertz [6, 8, 17, 20]. Current research explores LED semiconductor materials, light emission (white, RGB), modulation techniques, multiple access techniques, and MIMO to achieve the ultra-high data rate. Specific applications include wireless LAN, positioning and localization, underwater communications, underground mine communications, V2X communication, and hybrid communication (e.g., RF-VLC, PLC-VLC) [17, 20].

The literature has shown a great deal of interest in VLC-based indoor and outdoor positioning techniques. The VLP system has many advantages due to the inherent properties of VLC such as ultra high data rates and ultra low latency which are requirements for 6G applications. Moreover, the VLP system has a higher accuracy than the existing RF communication based positioning systems especially in indoor scenarios.

The CRLB is the benchmark for providing theoretical limits on distance and 3D position estimation accuracy. The CRLB offers a lower bound for the variance of any unbiased estimator [33]. The performance bounds of TOA based techniques were calculated in [36, 124]. The techniques in [28, 35, 37, 124] calculate the CRLB for a RSS based VLP system. In [28, 124], authors derived the CRLB for a hybrid (RSS/TOA)-based technique. However, these studies did not consider the effect of SDSN.

Unfortunately, different factors can degrade the performance of the VLC positioning, such as LOS absence, receiver SDSN, LED tilt position, synchronization errors, and mobility issues [17, 25–27]. The effect of the SDSN on distancing or 2D positioning accuracy limits was studied in [34, 35, 38, 41, 42], where an approximated form of SDSN was obtained using long-IR transmission wavelengths as was done in [46]. Evidently, these work did not consider the time dependency of the SDSN; therefore the SDSN was treated as normal AWGN with fixed variance. Needless to say, this does not reflect the

true nature of the SDSN.

To the best of the authors' knowledge, no work in the literature considered the time dependency of SDSN when calculating the error bounds in VLC systems. Using the system model from [47], this chapter investigates the theoretical limits on distance estimation in a DL VLP system under the joint effects of SDSN and thermal noises. More specifically, the performance evaluation is presented for TOA, RSS and hybrid (TOA/RSS) based distance estimations.

The rest of the chapter is organized as follows: Section 3.2 describes the setup of the VLP system under the effect of SDSN and thermal noises. Section 3.3 evaluates the CRLBs for the different scenarios. Numerical examples are presented in Section 3.4 to explain the theoretical results, where comparative analysis is presented among the various CRLBs. Finally, Section 3.5 provides concluding remarks.

3.2 System Description

This study considers an IM/DD VLC system as shown in Fig. 3.1. VLP systems function based on LOS VLC, where the photodetector receiver mostly lies in the FOV of the light signal emitted by the LED transmitter [17, 46]. The transmitter side uses an LED at a known position on the ceiling. The VLC photodetector receiver is placed on the floor. The photodetector receiver is assumed to be at an unknown distance from the LED transmitter. We consider an LOS scenario where the transmitted signal's attenuated version is received at the photodetector receiver after a certain time delay. The signals on the photodetector receiver side suffer from both SDSN and thermal noise, which can more faithfully reflect the VLC system's physical properties [47]. The SDSN and thermal noise can be modeled as AWGN, and the SDSN variance is dependent on the input signal [47]. Based on this, the received signal is formulated as

$$r(t) = \alpha\, R\, x(t-\tau) + \sqrt{\alpha\, R\, x(t-\tau)}\, \xi_{\text{sh}}(t) + \xi_{\text{th}}(t), \tag{3.1}$$

where α represents the optical channel attenuation factor ($\alpha > 0$). R is the photodetector responsivity and is considered constant over the optical bandwidth of the ranging signal. $x(t)$ is the transmitted signal and is real and positive over an interval of $[0, T_o]$, T_1 and T_2 determines the observation interval for the signal at the photodetector receiver, and τ is the TOA. It is assumed that $x(t)$ is contained completely in the observation interval $[T_1, T_2]$ i.e., $\tau \in [T_1, T_2 - T_o]$. From (3.1), $\sqrt{\alpha R\, x(t-\tau)}\, \xi_{\text{sh}}(t)$ represents the SDSN term, where $\xi_{\text{sh}}(t)$ is the shot noise and $\xi_{\text{th}}(t)$ is the thermal noise [47].

From the statistics of the additive noise, the elements $\xi_{\text{sh}}(t)$ and $\xi_{\text{th}}(t)$ are modeled to be independent and identically distributed (i.i.d.) random variables (RV), implying $\xi_{\text{sh}}(t) \sim N(0, \zeta_n^2 \sigma_n^2)$[1] and $\xi_{\text{th}}(t) \sim N(0, \sigma_n^2)$. Here, σ_n^2 describes the strength of the noise and $\zeta_n^2 > 0$ describes the ratio between the variances of SDSN and thermal noise. $\zeta_n^2 > 0$ is determined by the receiver parameters [47]. However, our analysis is valid for any value of ζ_n^2.

In (3.1), the optical channel attenuation factor α related to RSS is modeled as [34]

$$\alpha = \frac{(m+1)\, W}{2\, \pi\, d^2} \cos^m(\phi) \cos(\theta), \tag{3.2}$$

where m is the LED's Lambertian order, which depends on the approximate Lambertian model $m = -(ln\, 2 / ln(\cos \theta_{\frac{1}{2}}))$ [46]. W is the effective area of the photodetector and d is the distance between LED transmitter and photodetector receiver. The orientation of LED transmitter and photodetector receiver are assumed to be similar to what is seen in [34] and [124].

Therefore, the irradiance angle (see Fig. 3.1) ϕ that photodetector receiver makes with a particular LED transmitter (i.e with the perpendicular axis) equals the incidence angle θ with respect to the optical axis of photodetector receiver. Hence, $\cos(\phi) = \cos(\theta) = h/d$, where h denotes the height of the LED transmitter with respect to photodetector receiver. It is assumed that h, W, and m are known [34]. Thus,

[1] $N(\mu, \sigma^2)$ represents the Gaussian distributed random variable with μ mean and σ^2 variance.

(3.2) can be simplified to

$$\Upsilon \triangleq \frac{(m+1)\,W}{2\pi}\,h^{m+1}, \tag{3.3a}$$

$$\alpha = \Upsilon\, d^{-(m+3)}, \tag{3.3b}$$

and τ in (3.1) is modeled as

$$\tau = \frac{d}{c} + \Delta, \tag{3.4}$$

where c represents the speed of light. The LED transmitter clock is used as a reference and it is assumed that photodetector receiver has a clock bias Δ with respect to it. In the case of a synchronous system $\Delta = 0$, and for an asynchronous system, Δ is modeled as an unknown deterministic parameter. As a result, (3.1) can be re-written as [33]

$$y(t) = \alpha\, R\, x(t-\tau) + \Omega(t). \tag{3.5}$$

Here, $\Omega(t) \sim N(0, \Gamma)$, where $\Gamma = \sigma_n^2\,(1 + \alpha\, R\, x(t-\tau)\,\zeta_n^2)$. It is also assumed that R and $x(t)$ are known at the photodetector receiver.

3.3 Cramér–Rao Lower Bounds

This section studies the performance bounds of the system under the effect of SDSN. We calculate the CRLBs for different scenarios depending on the relationships between d, τ and α when the system is under the effect of the SDSN. Then, we compare the result with the CRLBs that are evaluated when $\zeta_n^2 = 0$. Considering the received signal model in (3.5), the PDF of the received signal can be written as [33]

$$f(y(t)|x) = \frac{1}{\sqrt{2\,\pi\,\Gamma}} \exp\left(-\frac{1}{2\,\Gamma}\,(y(t) - \alpha\, R\, x(t-\tau))^2\right). \tag{3.6}$$

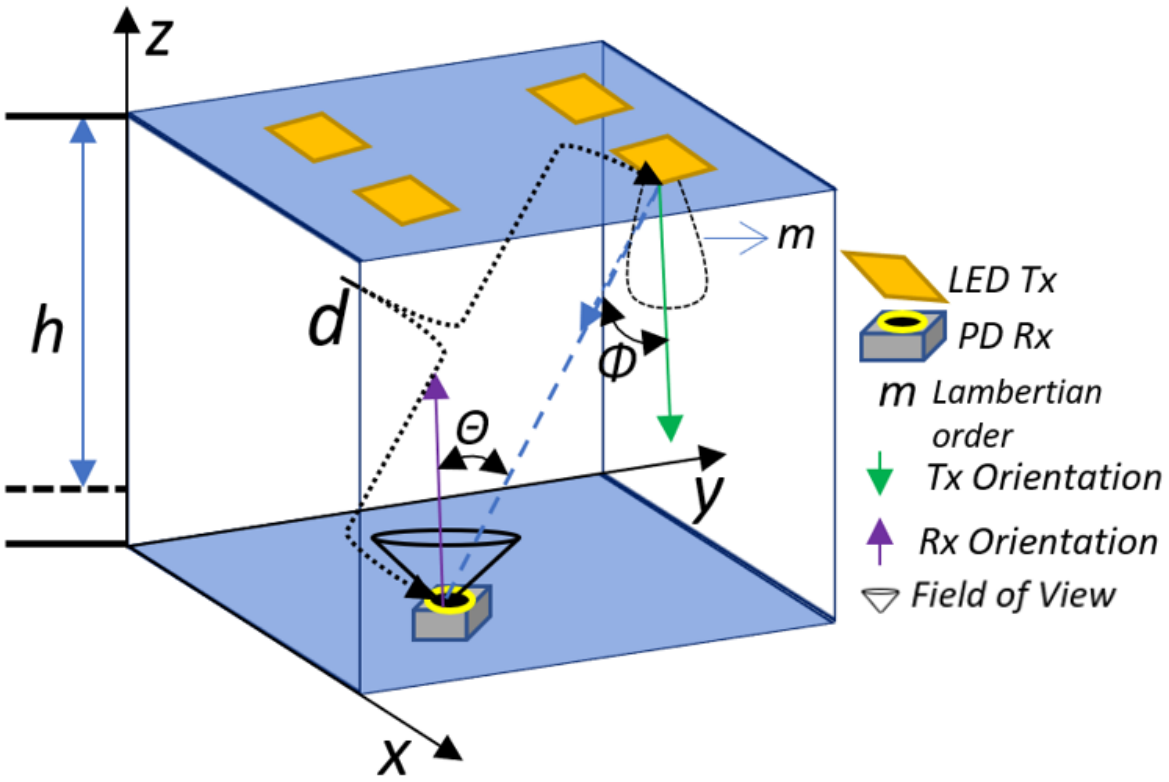

Figure 3.1: The distance-based VLP system model schematic diagram.

By observing the interval of the transmitted signal, the log-likelihood of (3.6) can be given as [33]

$$\mathcal{L}\left(\boldsymbol{\varrho}\right) = -\frac{1}{2}\ln\left(2\,\pi\right) - \frac{1}{2}\int_{T_1}^{T_2} \ln\,\sigma_n^2\left(1+\alpha\,R\,x(t-\tau)\,\zeta_n^2\right)dt \\ - \frac{1}{2\,\sigma_n^2}\int_{T_1}^{T_2}\frac{\left(y(t)-\alpha\,R\,x(t-\tau)\right)^2}{\left(1+\alpha\,R\,x(t-\tau)\zeta_n^2\right)}dt, \tag{3.7}$$

where $\boldsymbol{\varrho}$ represents the set of unknown parameters that need to be estimated. These depend on the different scenarios to be proposed in the upcoming pages.

$\mathcal{I}(\boldsymbol{\varrho})$ is the fisher information matrix (FIM) of $\boldsymbol{\varrho}$, which is obtained from $\mathcal{L}\left(\boldsymbol{\varrho}\right)$ as in [33]

$$\mathcal{I}(\boldsymbol{\varrho}) = \mathbb{E}\left\{\left(\nabla_{\boldsymbol{\varrho}}\mathcal{L}(\boldsymbol{\varrho})\right)\left(\nabla_{\boldsymbol{\varrho}}\mathcal{L}(\boldsymbol{\varrho})\right)^T\right\}, \tag{3.8}$$

where, $\nabla_{\boldsymbol{\varrho}}$ is the gradient operator. The CRLB expresses the lower bound for the

variance of unbiased estimators and is obtained by talking inverse of the FIM. The covariance matrix of the estimation error can consequently be expressed as

$$\mathbb{E}\big\{(\hat{\boldsymbol{\varrho}}-\boldsymbol{\varrho})(\hat{\boldsymbol{\varrho}}-\boldsymbol{\varrho})^T\big\} \succeq \mathcal{I}(\boldsymbol{\varrho})^{-1}. \tag{3.9}$$

Here, $\boldsymbol{A} \succeq \boldsymbol{B}$ is equivalent to $\boldsymbol{A}-\boldsymbol{B} \geq 0$, where ≥ 0. The relevant interpretation here is that the matrix is positive and semidefinite. Now, we discuss the CRLBs for different scenarios based on various relationships between d, τ and α.

3.3.1 Case 1: Synchronous Distance Estimation with TOA

This scenario studies a synchronized VLP system under the assumption that the relationship between α and d as in (3.3a) is unknown. In the absence of a relationship between α and d, and due to a synchronization where $\Delta = 0$, the relationship between d and τ ($d = \tau\, c$) from (3.4) can be exploited. Therefore, the scenario is termed as TOA based distance estimation. When α is unknown to the photodetector receiver, the vector containing the set of unknown parameters in (3.7) becomes $\boldsymbol{\varrho} = (d, \alpha)$, and the log-likelihood function can be written as

$$\begin{aligned}\mathcal{L}(\boldsymbol{d},\boldsymbol{\alpha}) = &-\frac{1}{2}\ln(2\,\pi) - \frac{1}{2}\int_{T_1}^{T_2} \ln\sigma_n^2 \left(1+\alpha\, R\, x(t-\frac{d}{c})\zeta_n^2\right) dt \\ &- \frac{1}{2\,\sigma_n^2}\int_{T_1}^{T_2} \frac{\left(y(t)-\alpha\, R\, x(t-\frac{d}{c})\right)^2}{\left(1+\alpha\, R\, x(t-\frac{d}{c})\zeta_n^2\right)} dt.\end{aligned} \tag{3.10}$$

Now, the FIM $\boldsymbol{I(d,\alpha)}$ is derived from (3.8) and (3.10) to be

$$\boldsymbol{\mathcal{I}}(d,\alpha) = \begin{bmatrix} \mathbb{E}\left\{\left(\frac{\partial\mathcal{L}(d,\alpha)}{\partial d}\right)^2\right\} & \mathbb{E}\left\{\frac{\partial\mathcal{L}(d,\alpha)}{\partial d}\frac{\partial\mathcal{L}(d,\alpha)}{\partial \alpha}\right\} \\ \mathbb{E}\left\{\frac{\partial\mathcal{L}(d,\alpha)}{\partial \alpha}\frac{\partial\mathcal{L}(d,\alpha)}{\partial d}\right\} & \mathbb{E}\left\{\left(\frac{\partial\mathcal{L}(d,\alpha)}{\partial \alpha}\right)^2\right\} \end{bmatrix}, \tag{3.11a}$$

$$\boldsymbol{\mathcal{I}}_{11}(d,\alpha) = \left(\frac{R\,\alpha}{\sigma_n\, c}\right)^2 E_{\mathrm{A}} + \left(\frac{\zeta_n^2\, R\,\alpha}{c}\right)^2 E_{\mathrm{AA}}, \tag{3.11b}$$

$$\boldsymbol{\mathcal{I}}_{12}(d,\alpha) = \boldsymbol{\mathcal{I}}_{21}(d,\alpha) = -\left(\frac{R^2\,\alpha}{\sigma_n^2\,c}\right) E_{\rm C} - \left(\frac{\zeta^4\,R^2\,\alpha}{c}\right) E_{\rm CC}, \tag{3.11c}$$

$$\boldsymbol{\mathcal{I}}_{22}(d,\alpha) = \left(\frac{R}{\sigma_n}\right)^2 E_{\rm B} + \left(\zeta_n^2\,R\right)^2 E_{\rm BB}, \tag{3.11d}$$

where

$$E_{\rm A} \triangleq \int_0^{T_o} \frac{(x'(t))^2}{(1+\alpha\,R\,x(t)\zeta_n^2)}dt, \tag{3.12a}$$

$$E_{\rm AA} \triangleq \int_0^{T_o} \frac{(x'(t))^2}{(1+\alpha\,R\,x(t)\zeta_n^2)^2}dt, \tag{3.12b}$$

$$E_{\rm B} \triangleq \int_0^{T_o} \frac{(x(t))^2}{(1+\alpha\,R\,x(t)\zeta_n^2)}dt, \tag{3.12c}$$

$$E_{\rm BB} \triangleq \int_0^{T_o} \frac{(x(t))^2}{(1+\alpha\,R\,x(t)\zeta_n^2)^2}dt, \tag{3.12d}$$

$$E_{\rm C} \triangleq \int_0^{T_o} \frac{x(t)\,x'(t)}{(1+\alpha\,R\,x(t)\zeta_n^2)}dt, \tag{3.12e}$$

$$E_{\rm CC} \triangleq \int_0^{T_o} \frac{x(t)\,x'(t)}{(1+\alpha\,R\,x(t)\zeta_n^2)^2}dt. \tag{3.12f}$$

The effective CRLB can be obtained from (3.9) and (3.11a) after excluding the nuisance parameter α as [33]

$$\begin{aligned}\text{CRLB} &\triangleq \left(\boldsymbol{\mathcal{I}}_{11} - \boldsymbol{\mathcal{I}}_{12}\left(\frac{1}{\boldsymbol{\mathcal{I}}_{22}}\right)\boldsymbol{\mathcal{I}}_{21}\right)^{-1} \\ &= \left(\frac{\sigma_n\,c}{R\,\alpha}\right)^2 \frac{E_{\rm B} + \zeta^4\sigma_n^2 E_{\rm BB}}{(E_{\rm A} + \zeta^4\sigma_n^2 E_{\rm AA})\,(E_{\rm B} + \zeta^4\sigma_n^2 E_{\rm BB}) - (E_{\rm C} + \zeta^4\sigma_n^2 E_{\rm CC})^2}.\end{aligned} \tag{3.13}$$

Remark 1: If it assumed that α is known, then the vector of unknown parameters in (3.7) becomes $\boldsymbol{\varrho} = d$ and the FIM I(d) can be obtained from (3.8) as

$$\begin{aligned}\boldsymbol{\mathcal{I}}(d) &= \mathbb{E}\left\{\left(\frac{\partial\mathcal{L}(d)}{\partial d}\right)^2\right\} \\ &= \left(\frac{R\,\alpha}{\sigma_n\,c}\right)^2 E_{\rm A} + \left(\frac{\zeta_n^2 R\,\alpha}{c}\right)^2 E_{\rm AA}.\end{aligned} \tag{3.14}$$

Next, the CRLB can be obtained from (3.9) and (3.14) as

$$\text{CRLB} \triangleq \left(\frac{\sigma_n\, c}{R\,\alpha}\right)^2 \frac{1}{E_{\text{A}} + \zeta^4 \sigma_n^2\, E_{\text{AA}}}. \tag{3.15}$$

It is key to note that the CRLB in (3.13) is larger or equal to that in (3.15) due to estimation of the additional parameter.

3.3.2 Case 2: Synchronous Distance Estimation with Hybrid (TOA/RSS)

This scenario considers a synchronized VLP system under the assumption that the relationship between α and d as in (3.3a) is known. This assumption is considered practical for the LOS VLP system since α can be defined as a function of d. The scenario is termed hybrid (TOA/RSS) because information from both α and τ is used for distance estimation. It is also worth mentioning that α is related to RSS.

From (3.3a), (3.4), and (3.5) the vector containing the set of unknown parameters in (3.7) becomes $\boldsymbol{\varrho} = d$, and the corresponding log-likelihood function can be written as follows

$$\begin{aligned}\mathcal{L}(\boldsymbol{d}) = &-\frac{1}{2}\ln(2\,\pi) - \frac{1}{2}\int_{T_1}^{T_2} \ln \sigma_n^2 \left(1 + \Upsilon\, d^{-(m+3)}\, R\, x(t - \frac{d}{c})\zeta_n^2\right) dt \\ &- \frac{1}{2\,\sigma_n^2}\int_{T_1}^{T_2} \frac{\left(y(t) - \Upsilon\, d^{-(m+3)}\, R\, x(t - \frac{d}{c})\right)^2}{\left(1 + \Upsilon\, d^{-(m+3)}\, R\, x(t - \frac{d}{c})\, \zeta_n^2\right)} dt.\end{aligned} \tag{3.16}$$

Now, the FIM $\mathcal{I}(d)$ is derived from (3.8) and (3.16) to be

$$\begin{aligned}\boldsymbol{\mathcal{I}}(d) &= \mathbb{E}\left\{\left(\frac{\partial \mathcal{L}(d)}{\partial d}\right)^2\right\}, \\ \mathcal{I}(d) &= \left(\frac{R\,\Upsilon}{\sigma_n\, d^{m+4}}\right)^2 v_1(d) + \left(\frac{\zeta_n^2\, R\,\Upsilon}{d^{m+4}}\right)^2 v_2(d),\end{aligned} \tag{3.17}$$

where

$$v_1(d) \triangleq (m+3)^2 E_{\mathrm{B}} + 2(m+3)\left(\frac{d}{c}\right) E_{\mathrm{C}} + \left(\frac{d}{c}\right)^2 E_A, \tag{3.18}$$

$$v_2(d) \triangleq (m+3)^2 E_{\mathrm{BB}} + 2(m+3)\left(\frac{d}{c}\right) E_{\mathrm{CC}} + \left(\frac{d}{c}\right)^2 E_{\mathrm{AA}}, \tag{3.19}$$

where E_{A}, E_{AA}, E_{B}, E_{BB}, E_{C}, and E_{CC} are given in (3.12). Next, the CRLB is derived from (3.9) and (3.17) as

$$\mathrm{CRLB} \triangleq \left(\frac{\sigma_n\, d^{m+4}}{R\,\Upsilon}\right)^2 \frac{1}{v_1(d) + (\zeta_n^2\,\sigma_n)^2\, v_2(d)}. \tag{3.20}$$

Now, (3.20) shows that degradation becomes serious as $\zeta_n^2 \to \infty$. In this case, the term v_1 in the denominator $\to 0$, which greatly increases the CRLB.

3.3.3 Case 3: Asynchronous Distance Estimation with RSS

The previous scenarios studied a synchronous distance estimation where $\Delta = 0$. This scenario studies the asynchronous case where Δ is considered to be an unknown deterministic parameter. The relationship between τ and d as in (3.4) is unknown, meaning that the relationship between α and d as in (3.3a) needs to be exploited in order to estimate the distance. Therefore, the scenario is termed RSS based distance estimation. Since τ is unknown to the photodetector receiver, the vector containing the set of unknown parameters in (3.7) becomes $\boldsymbol{\varrho} = (d, \tau)$, and the corresponding log-likelihood function can be written as follows

$$\begin{aligned}\mathcal{L}(\boldsymbol{d}, \boldsymbol{\tau}) = &-\frac{1}{2}\ln(2\pi) - \frac{1}{2}\int_{T_1}^{T_2} \ln\sigma_n^2 \left(1 + \Upsilon\, d^{-(m+3)}\, R\, x(t-\tau)\zeta_n^2\right) dt \\ &- \frac{1}{2\,\sigma_n^2}\int_{T_1}^{T_2} \frac{\left(y(t) - \Upsilon\, d^{-(m+3)}\, R\, x(t-\tau)\right)^2}{\left(1 + \Upsilon\, d^{-(m+3)}\, R\, x(t-\tau)\, \zeta_n^2\right)} dt.\end{aligned} \tag{3.21}$$

Now, the FIM $\mathcal{I}(d,\tau)$ or simply $\mathcal{I}$, can be derived from the distance estimation by applying (3.8) and (3.21) as follows

$$\boldsymbol{\mathcal{I}} = \begin{bmatrix} \mathbb{E}\left\{\left(\frac{\partial \mathcal{L}(d,\tau)}{\partial d}\right)^2\right\} & \mathbb{E}\left\{\frac{\partial \mathcal{L}(d,\tau)}{\partial d}\frac{\partial \mathcal{L}(d,\tau)}{\partial \tau}\right\} \\ \\ \mathbb{E}\left\{\frac{\partial \mathcal{L}(d,\tau)}{\partial \tau}\frac{\partial \mathcal{L}(d,\tau)}{\partial d}\right\} & \mathbb{E}\left\{\left(\frac{\partial \mathcal{L}(d,\tau)}{\partial \tau}\right)^2\right\} \end{bmatrix}, \tag{3.22}$$

where

$$\boldsymbol{\mathcal{I}}_{11} = \left(\frac{R\,\Upsilon}{\sigma_n d^{m+4}}\right)^2 (m+3)^2\, E_{\mathrm{B}} + \left(\frac{\zeta_n^2\, R\,\Upsilon}{d^{m+4}}\right)^2 (m+3)^2\, E_{\mathrm{BB}}, \tag{3.23a}$$

$$\boldsymbol{\mathcal{I}}_{12} = \boldsymbol{\mathcal{I}}_{21} = \left(\frac{R\,\Upsilon}{\sigma_n\, d^{m+4}}\right)^2 d\,(m+3)\, E_{\mathrm{C}} + \left(\frac{\zeta_n^2 R\Upsilon}{d^{m+4}}\right)^2 d\,(m+3)\, E_{\mathrm{CC}}, \tag{3.23b}$$

$$\boldsymbol{\mathcal{I}}_{22} = \left(\frac{R\,\Upsilon}{\sigma_n\, d^{m+4}}\right)^2 d^2\, E_{\mathrm{A}} + \left(\frac{\zeta_n^2\, R\,\Upsilon}{d^{m+4}}\right)^2 d^2\, E_{\mathrm{AA}}. \tag{3.23c}$$

Then, the effective CRLB is obtained from (3.9) and (3.23) after excluding the nuisance parameter τ as [33]

$$\begin{aligned} \mathrm{CRLB} &\triangleq \left(\boldsymbol{\mathcal{I}}_{11} - \boldsymbol{\mathcal{I}}_{12}\left(\frac{1}{\boldsymbol{\mathcal{I}}_{22}}\right)\boldsymbol{\mathcal{I}}_{21}\right)^{-1} \\ &= \left(\frac{\sigma_n\, d^{m+4}}{\Upsilon\, R\,(m+3)}\right)^2 \\ &\quad \times \frac{E_{\mathrm{A}} + \zeta^4 \sigma_n^2\, E_{\mathrm{AA}}}{\left(E_{\mathrm{A}} + \zeta^4\sigma_n^2\, E_{\mathrm{AA}}\right)\left(E_{\mathrm{B}} + \zeta^4\sigma_n^2\, E_{\mathrm{BB}}\right) - \left(E_{\mathrm{C}} + \zeta^4\sigma_n^2\, E_{\mathrm{CC}}\right)^2}. \end{aligned} \tag{3.24}$$

3.4 Discussion and Evaluation Results

In this section, the simulation setup is presented to investigate the theoretical limits of the distance estimation. Unless otherwise stated, we assume that the height $h = 2.5$ m, the Lambertian order $m = 1$, the photodetector receiver is 4 m away from the

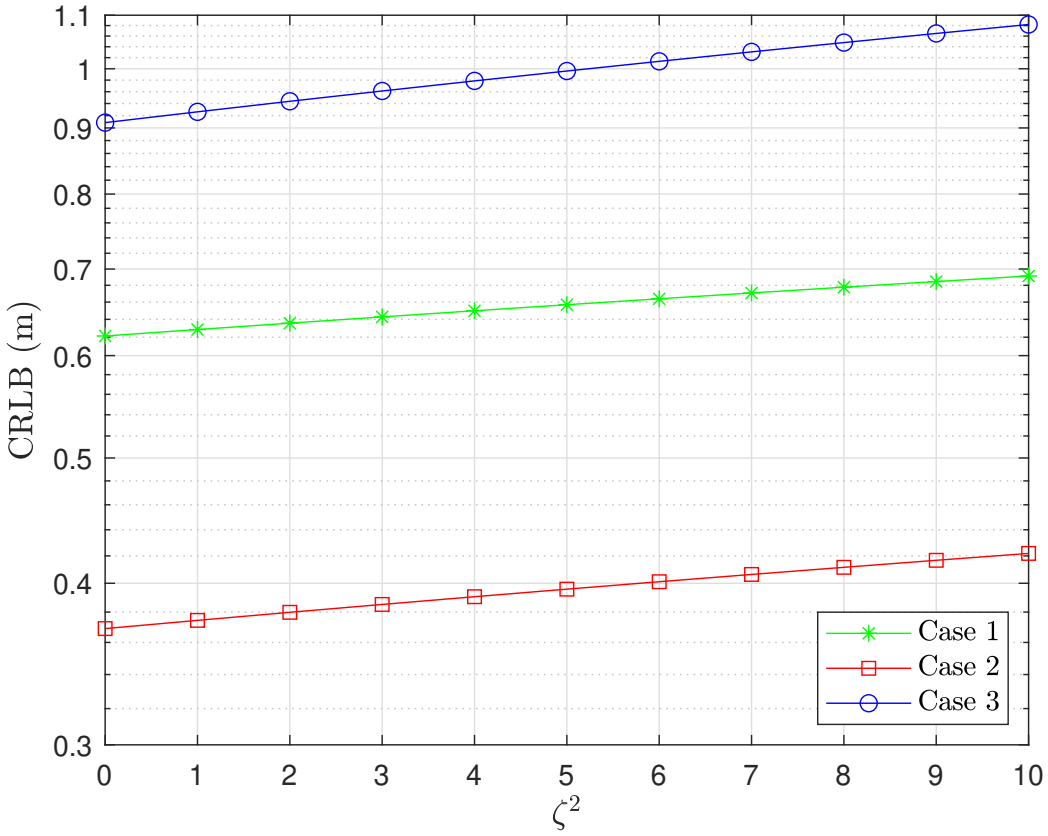

Figure 3.2: CRLB versus ζ_n^2 for Case 1, Case 2 and Case 3.

LED transmitter, the noise variance is $\sigma_n^2 = 10^{-10}$, and $\zeta_n^2 > 0$ as these are practical values [47]. The photodetector responsivity is $R = 1$ amps/watt, the effective area of photodetector W is 3×3 cm^2, and the signal $x(t)$ in (3.5) is modeled as [34, 124]

$$x(t) = A\left(1 - \cos\left(2\,\pi\,t/T_o\right)\right)\left(1 + \cos\left(2\,\pi\,f_c\,t\right)\right), \tag{3.25}$$

where A denotes the source optical power and f_c corresponds to the carrier frequency. Here, the source optical power is directly proportional to the LED Lumens at the transmitter. Therefore, the power constraints apply directly to the LED input and not to the square of its magnitude (as is usually the case for electrical transmission models) [47].

The signal in (3.25) is a dc-biased windowed sinusoid, where $A = 30$ dB is applied

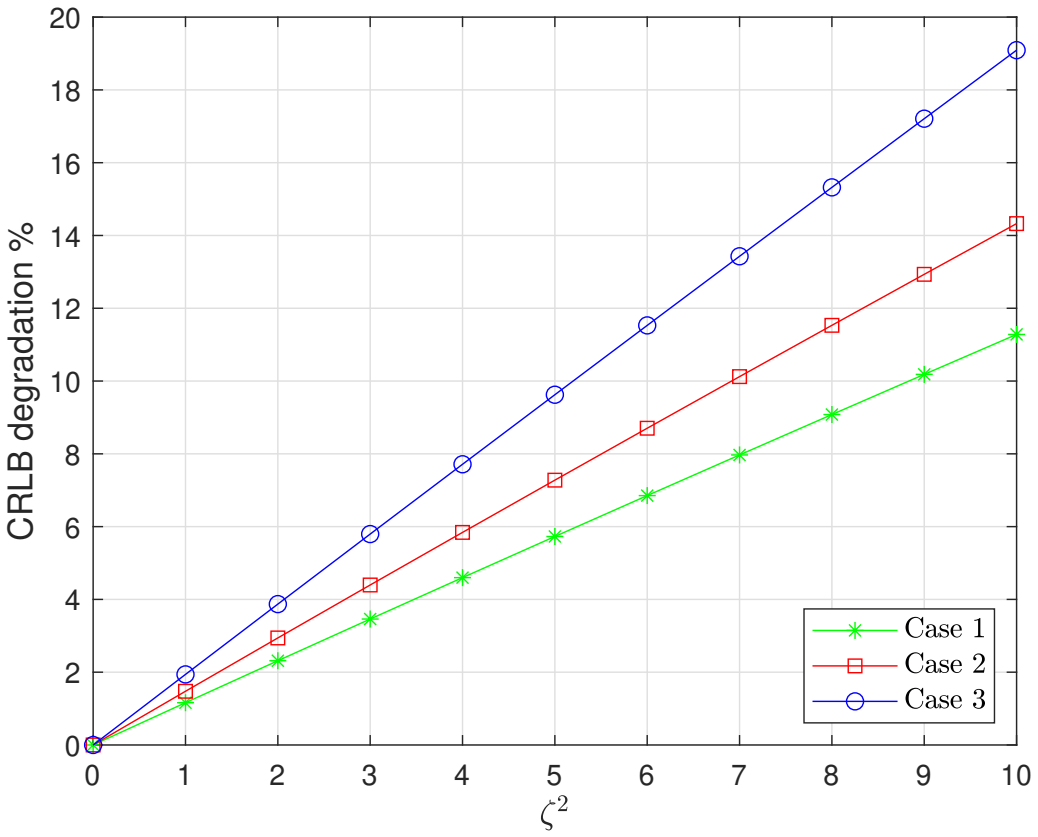

Figure 3.3: CRLB degradation % versus ζ_n^2 for Case 1, Case 2 and Case 3.

with a signal duration of $T_o = 10^{-6}$ s and a carrier frequency of $f_c = 100$ MHz. All transmitted signal energies as in (3.12) have been calculated numerically. Finally, in this section, Case 1 implies that the channel attenuation factor is unknown at the photodetector receiver. Case 2 suggests that the time delay parameter and channel attenuation factor are known at the photodetector receiver. Case 3 proposes that the time delay parameter is unknown at the photodetector receiver.

Fig. 3.2 studies the impact of ζ_n^2 on the CRLBs. The CRLB for all cases degrades as ζ_n^2 increases, as evident from the figure. Moreover, the SDSN has a severe impact on the estimation bounds in all the cases. The difference between the CRLB at $\zeta_n^2 = 0$, and $\zeta_n^2 = 10$ is about 7 cm for case 1, 5.3 cm for case 2 and 17.4 cm for case 3.

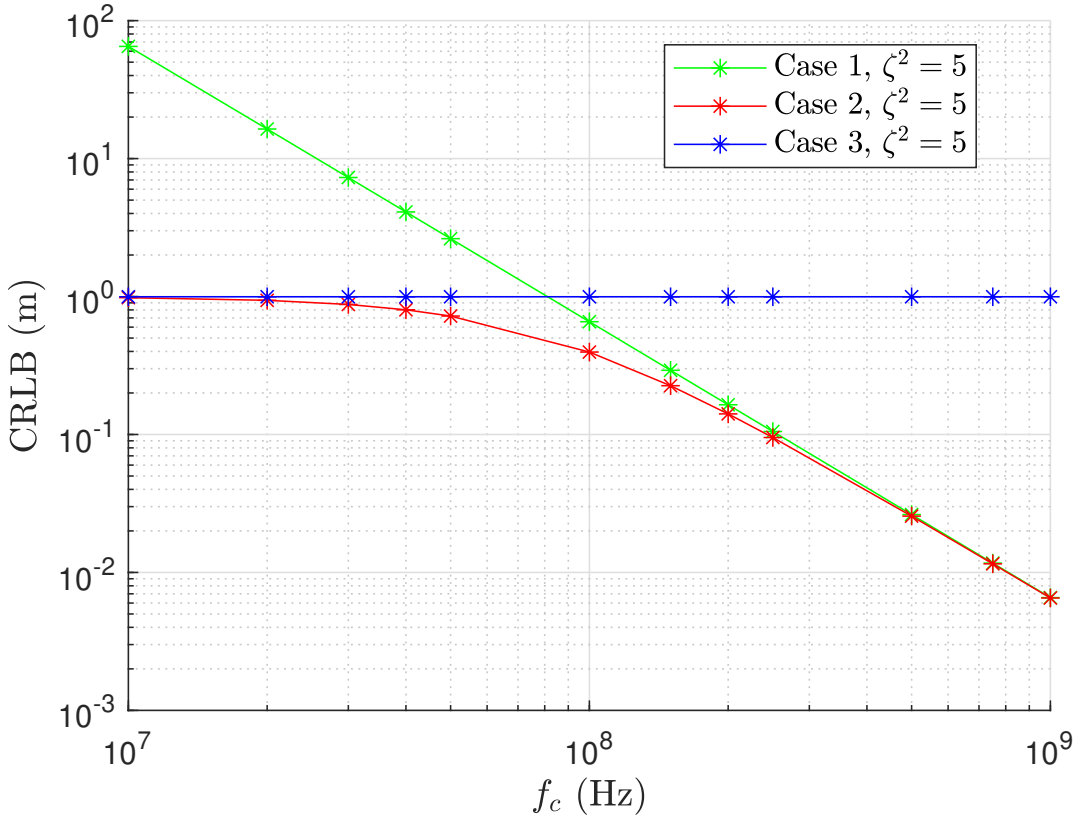

Figure 3.4: CRLB versus f_c for Case 1, Case 2 and Case 3.

Fig. 3.3 illustrates the CRLB degradation due to ζ_n^2. We calculate this degradation using the following equation

$$\text{CRLB}_{\text{deg}} = \left(\frac{\text{CRLB}_{\zeta_n^2}}{\text{CRLB}_{\zeta_n^2 = 0}} - 1 \right) \times 100\%, \tag{3.26}$$

where the CRLBs for each case are obtained using (3.13), (3.20) and (3.24). This figure shows that the degradation level due to the SDSN varies depending on the estimation technique. For instance, there are three levels of degradation, case 3 being the worst, and case 1 being the least degraded. Even though case 2 has the best CRLB under SDSN , the degradation is worse than that of case 1. The reason for this is that case 2 and case 3 use α (RSS based estimation) to estimate the distance while case 1 only considers τ.

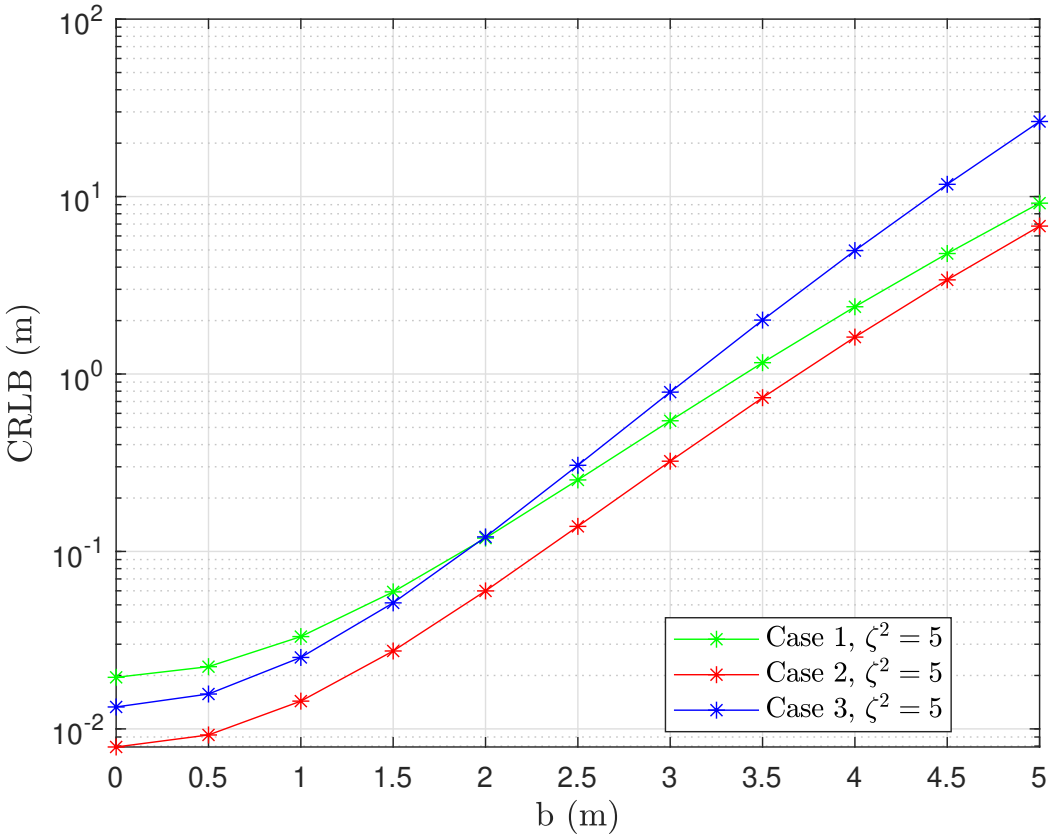

Figure 3.5: CRLB versus distance away from center b for for Case 1, Case 2 and Case 3.

Fig. 3.4 studies the CRLBs impacted by SDSN under different frequencies. The frequency parameter f_c is in Hz range. The CRLBs are plotted versus different frequencies for $\zeta^2 = 5$. For $f_c = 10$ MHz, it can be observed that the CRLB for Case 1 is significantly larger than the CRLB for Case 2 but they become comparable when $f_c > 100$ MHz. As for Case 3, change in frequency f_c has on impact on the CRLB.

Fig. 3.5 studies the CRLBs impacted by SDSN when the photodetector receiver moves away from the LED transmitter when $\zeta^2 = 5$. The distance is calculated as $d = \sqrt{h^2 + b^2}$ where h is height and $b \in [0, 5]$ m is the distance away from the center. As the photodetector receiver moves away from the center, the effect of SDSN decreases as the energy of the signal reduces. The photodetector receiver at a larger distance d away from center receives lower optical power. Therefore, lower electrical energy, which

increases the CRLB.

Fig. 3.6 studies the impact of ζ_n^2 when increasing the transmitted power. The CRLBs are plotted against the source's optical power A for all cases considering $\zeta_n^2 \in \{0, 10\}$. As expected, higher optical power at the source enhances the CRLBs in all cases. Interestingly, higher values of SDSN minimize the effect of increasing the power in all the cases. For example, a 0.5 dB power loss between $\zeta_n^2 = 0$ and $\zeta_n^2 = 10$ can be noticed in case 2 when the CRLB $= 10^{-1}$. This loss reaches 1.5 dB when the CRLB $= 10^{-2}$. The same trend can be seen in the other cases. Moreover, due to the SDSN , the performance of case 1 can be degraded to the level of case 3 with no SDSN , as seen in the subplot where the green and blue line intersects. The same behaviour can be seen for cases 1 and 2.

3.5 Conclusion

This chapter presents the theoretical CRLBs of a VLP system under the effect of SDSN. We consider different synchronous and asynchronous scenarios, specifically the three cases of TOA, RSS and Hybrid (TOA/RSS) based distance estimations. To this end, we consider the relationships between the distance, channel attenuation factor, and time delay parameter. It was shown that the SDSN has a severe impact on the estimation bounds in all cases. In addition, the degradation level is higher for scenarios that depend on RSS compared to when the estimation only considers the time of arrival. The CRLBs for TOA, hybrid (TOA/RSS) and RSS are degrade by more than 11%, 14% and 19%, respectively when SDSN ($\zeta_n^2 = 10$). More realistic scenarios where multiple LED transmitters and a receiver having arbitrary orientations with bi-directional communication can be considered in the future work.

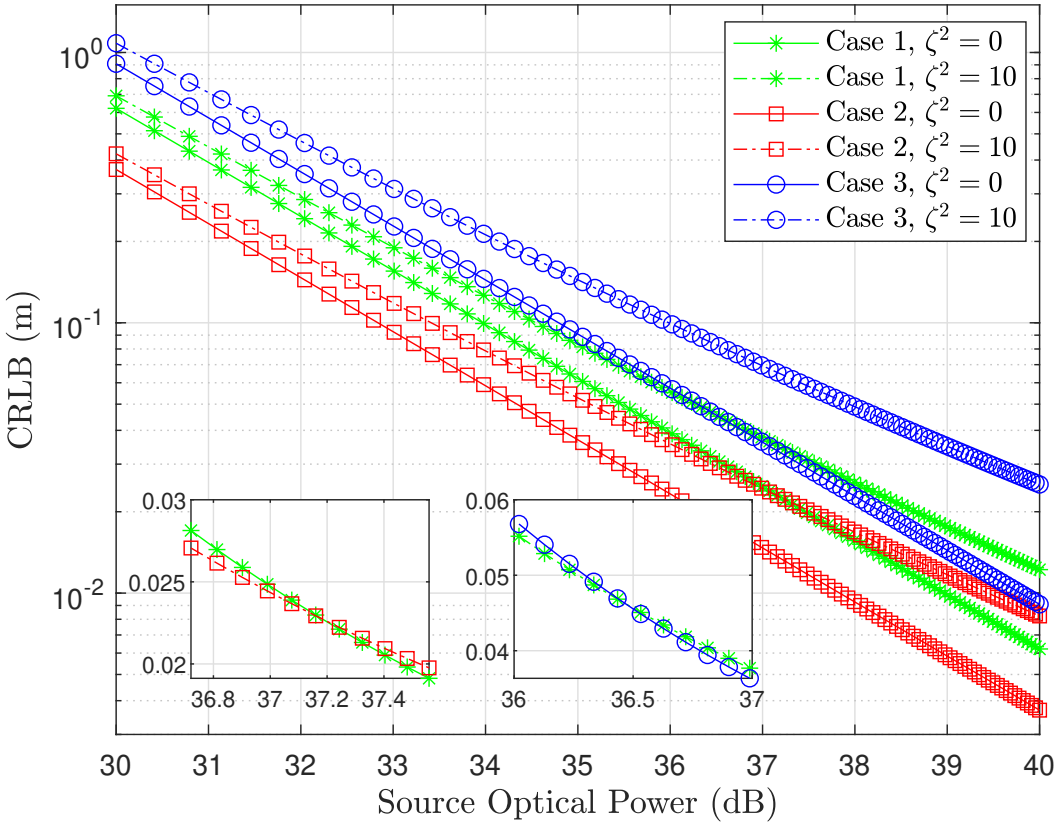

Figure 3.6: CRLB versus source optical power for Case 1, Case 2 and Case 3.

Chapter 4

Distance Estimation in Visible Light Communications: The Case of Imperfect Synchronization and Signal-Dependent Noise

4.1 Introduction and Related Works

VLC is anticipated to be a key player among emerging technologies, especially when it comes to meeting 6G communication system requirements [6]. In VLC systems, the LED acts as a transmitter and the photodetector as a receiver. These systems transmit data through the modulation of light signals within the visible spectrum, which ranges between 380 and 750 nanometer. The VLC systems are expected to achieve an ultra-high data rate (Gbps to Tbps) and ultra-low latency for bi-directional and optical wireless link connectivity. An additional benefit is an ultra-high bandwidth in an unregulated and license-free spectrum [7, 17].

The VLC systems are extremely practical because they can be deployed in many

network topologies (e.g., vehicular, infrastructure, and mobile communication). However, visible light as a medium has certain range limitations since it cannot pass through opaque boundaries. That said, this characteristic inherently protects the communication channel [25]. The VLC systems are also suitable for settings in underground mining and healthcare, where the use of RF communication is inappropriate due to EMI [6, 7].

There are significant research interests that take advantage of the VLC systems for distance estimation and localization applications. Currently, VLP systems provide higher accuracy than RF-based positioning systems due to the inherent physical properties of VLC [17]. The existing VLC positioning techniques use diverse parameters, including RSS, TOA, TDOA, PDOA, AOA, and hybrid systems [25].

Moreover, vehicular visible light communication systems utilize the VLC concepts in vehicular networks [125]. There are mainly three use cases, V2I, I2V, and V2V [17, 25, 125]. These use cases support various applications where VLC can be applied. For example vehicle indoor navigation and parking [126, 127], vehicle safety in tunnel environment [25, 29], and position in underground mines [25, 128].

The VLP system performance is evaluated in the literature by calculating the CRLB, which is the lower bound of the variance for any unbiased estimator [33]. Many studies have evaluated the theoretical limits on distance and 3D position estimation for VLC systems [28, 34–39, 41–43]. In particular, the works in [34, 36] and [28] calculated the performance bounds using TOA-based techniques. Then, performance analysis for the TDOA-based technique was carried out in [39]. The authors in [28, 35, 37, 41–43] used RSS-based techniques to calculate the CRLB s. In [38] and [28], the performance bounds were derived for hybrid systems by exploiting RSSand considering PDOA and TOA parameters.

The VLP system accuracy is affected by many factors that include but are not limited to: SDSN at the receiver, time synchronization problems, transmitter and receiver orientation, limited transmission distance and mobility issues [17, 25–27]. The effect of SDSN on the distancing or 2-D (two-dimensional) positioning accuracy limits has

been studied in [34, 35, 38, 41, 42]. These works did not consider, however, the time dependency of SDSN, therefore treating it as normal AWGN with fixed variance. Unfortunately, this does not represent the nature of SDSN in a realistic manner. Similarly, no distance estimation technique addresses the time synchronization problem without requiring multiple LEDs or photodetectors at the transmitter or receiver sides. For instance, in asynchronous VLP systems, the TDOA-based technique can be adopted, but it requires at least two LEDs at the transmitter. Time synchronization also remains a requirement between the transmitters [25, 26].

The current literature indicates that SDSN and imperfect synchronization have a considerable impact on VLP systems. In an attempt to fill in some of the gaps regarding the nature of these impacts, this chapter has two goals: 1) We consider the time dependency of SDSN and use it to calculate the distance estimation bounds of VLC systems. More specifically, the CRLB is calculated for different estimation scenarios. 2) We adopt a bi-directional synchronization protocol that can mitigate the effects of imperfect synchronization between LED transmitter and photodetector receiver. This protocol needs only one LED transmitter and one photodetector receiver to determine the distance estimate via UL and DL communications between the LED transmitter and photodetector receiver.

The rest of the chapter is organized as follows. The system model is presented in Section 4.2, followed by a synchronization protocol in Section 4.3. The CRLB expressions for directional and bi-directional are calculated in Section 4.4. The performance analysis is then presented in Section 4.5. Finally, the chapter is concluded in Section 4.6.

4.2 System Description

This study considers an IM/DD bi-directional VLC system. The system uses one access point (AP)and one user device (UD) such that the communication link between the devices is bi-directional, as shown in Fig. 4.1. It is also assumed that the AP is located

at a known position and that the UD is placed at an unknown position. A LOS scenario is considered where an attenuated version of the transmitted signal is accepted after some delay by the receiving device. The DL optical wireless channel attenuation factor α^{dl} can be modeled as in [46]

$$\alpha^{\mathrm{dl}} = \frac{(m_{\mathrm{ap}}+1)W_{\mathrm{ud}}}{2\pi d^2}\cos^{m_{\mathrm{ap}}}(\phi)\cos(\theta), \tag{4.1}$$

where m_{ap} is the LED's Lambertian order, W_{ud} is the photodetector's effective area, d is the distance between AP and UD, ϕ and θ are the orientation angles at AP and UD, respectively. The UL channel attenuation factor α^{ul} can be obtained by exchanging ϕ and AP in (4.1) with θ and UD, respectively $\left(\alpha^{\mathrm{ul}} = \frac{(m_{\mathrm{ud}}+1)W_{\mathrm{ap}}}{2\pi d^2}\cos^{m_{\mathrm{ud}}}(\phi)\cos(\theta)\right)$. However, this work assumes that $\cos(\phi) = \cos(\theta) = h/d$, where h denotes the perpendicular distance between the AP and UD[1]. Thus, UL and DL channel attenuation factors can be simplified to

$$\begin{aligned}\Upsilon_i &\triangleq \frac{(m_k+1)W_i}{2\pi}\,h^{m_k+1},\\ \alpha^j &= \Upsilon_i\, d^{-(m_k+3)},\end{aligned} \tag{4.2}$$

where $j \in [\mathrm{ul}, \mathrm{dl}]$ and $i, k \in [\mathrm{ap}, \mathrm{ud}]$, $i \neq k$. It is assumed that the receiving device knows the h, W_i, and m_k [28, 34]. The received signal suffers from both SDSN and thermal noise, a scenario that better reflects the VLC system's physical properties [47]. These noises can be modeled as AWGN random variable $N(\mu, \sigma^2)$ with μ mean and σ^2 variance, where the variance of the SDSN is dependent on the input signal [47]. Based on this, the received signal is formulated as

$$r_i(t) = \alpha^j R_i\, x_k(t-\tau^j) + \sqrt{\alpha^j R_i\, x_k(t-\tau^j)}\,\xi_{\mathrm{sh}_i}(t) + \xi_{\mathrm{th}_i}(t). \tag{4.3}$$

[1]The analysis in this study can be extended to any arbitrary value of ϕ and θ. However, it is not performed as the expressions become lengthy and inconvenient.

The observation time interval is represented by t such that $t \in [T_1, T_2]$, $(\alpha^j > 0)$. Here, R_i indicates the photodetector's responsivity, $x_k(t)$ is the transmitted signal. $\sqrt{\alpha^j R_i\, x_k(t-\tau^j)}\,\xi_{\mathrm{sh}_i}(t)$ is the SDSN and $\xi_{\mathrm{th}_i}(t)$ is the thermal noise. From additive noise statistics, the elements $\xi_{\mathrm{sh}_i}(t)$ and $\xi_{\mathrm{th}_i}(t)$ are modeled to be independent and identically distributed (i.i.d.) random variables, implying that $\xi_{\mathrm{sh}_i}(t) \sim N(0, \zeta_n^2\sigma_n^2)$ and $\xi_{\mathrm{th}_i}(t) \sim N(0, \sigma_n^2)$. Here, $\sigma_n^2 > 0$ describes the strength of the noise and $\zeta_n^2 > 0$ describes the ratio of the SDSN variance to the thermal noise variance [47]. We consider σ_n^2 and ζ_n^2 to be the same for both UL and DL communications. τ^j is the time delay (TOA) observed at the receiving device in UL and DL communications, and can be modeled as

$$\tau^j = \tau + \Delta^j, \quad \tau = \frac{d}{c}, \tag{4.4}$$

where c denotes the speed of light and Δ^j is the clock timing offset between AP and UD. It is worth mentioning that TOA is equal to the time delay between UD and AP. Therefore, and as done in the literature, TOA and time delay are used interchangeably here. A perfectly synchronous system will have no clock bias (i.e., $\Delta^j = 0$); however, in the case of an asynchronous system, Δ^j is modeled as an unknown deterministic parameter. From (4.3), the received signal can be rewritten as

$$y_i(t) = \alpha^j R_i\, x_k(t-\tau^j) + \Omega_i(t), \tag{4.5}$$

where $\Omega_i(t) \sim N(0, \Gamma_i)$ and $\Gamma_i = \sigma_n^2\,(1 + \alpha^j R_i x_k(t-\tau^j)\zeta_n^2)$. It is assumed that R_i and $x_k(t)$ are known at the photodetector receiver.

4.3 Bi-directional Synchronization Protocol

This section explains the bi-directional protocol that addresses the clock synchronization problem in VLP systems. The process can be initiated by either AP or UD, but here we consider the case of AP. In this case, the distance from the responding signal is

estimated. Fig. 4.2 illustrates the bi-directional protocol, where the AP's clock is used as a reference. The AP's LED initiates the signal $x_{\text{ap}}(t)$ at $t = 0$ in its local time (the local time at the UD is $t = \Delta^{\text{dl}}$ at this instance). After that, the UD receives the signal at $t = \tau + \Delta^{\text{dl}}$. Based on this, the received signal can be written from (4.5) as

$$y_{\text{ud}}(t) = \alpha^{\text{dl}} R_{\text{ud}}\, x_{\text{ap}}(t - \tau^{\text{dl}}) + \Omega_{\text{ud}}(t). \tag{4.6}$$

Now, the UD estimates $\hat{\tau}^{\text{dl}}$ and replies after a predetermined delay Λ. This means that it replies at $t = \hat{\tau}^{\text{dl}} + \Lambda$ according to its local time (the local time at the AP is $t = \hat{\tau}^{\text{dl}} + \Lambda + \Delta^{\text{ul}}$ at this instance). The AP receives the UD's reply at $t = \hat{\tau}^{\text{dl}} + \Lambda + \tau + \Delta^{\text{ul}}$ (this is the local time at the AP). Hence, the reply signal is received as

$$y_{\text{ap}}(t) = \alpha^{\text{ul}} R_{\text{ap}}\, x_{\text{ud}}(t - \tau^{\text{ul}}) + \Omega_{\text{ap}}(t). \tag{4.7}$$

The TOA parameter estimates from (4.6) and (4.7) are given as

$$\hat{\tau}^{\text{dl}} = \tau + \Delta^{\text{dl}} + e^{\text{dl}}, \tag{4.8}$$

$$\hat{\tau}^{\text{ul}} = \hat{\tau}^{\text{dl}} + \Lambda + \tau + \Delta^{\text{ul}} + e^{\text{ul}}, \tag{4.9}$$

where e^{dl} and e^{ul} are TOA estimation errors at the respective devices. Now, by substituting (4.8) into (4.9), and noting that $\Delta^{\text{dl}} = -\Delta^{\text{ul}}$, the $\hat{\tau}^{\text{ul}}$ can be given as

$$\hat{\tau}^{\text{ul}} = 2\tau + \Lambda + e^{\text{ul}} + e^{\text{dl}}. \tag{4.10}$$

The bi-directional protocol removes the effect of Δ and therefore resolves the synchronization problem. The AP estimates $\hat{\tau}^{\text{ul}}$ and eventually determines the distance d. In the case where the UD needs to estimate the distance to the AP, it would also be the initiator. All the above expressions would be maintained except for the subscripts of AP and UD, which are exchanged. Consequently, the superscripts for UL and DL would

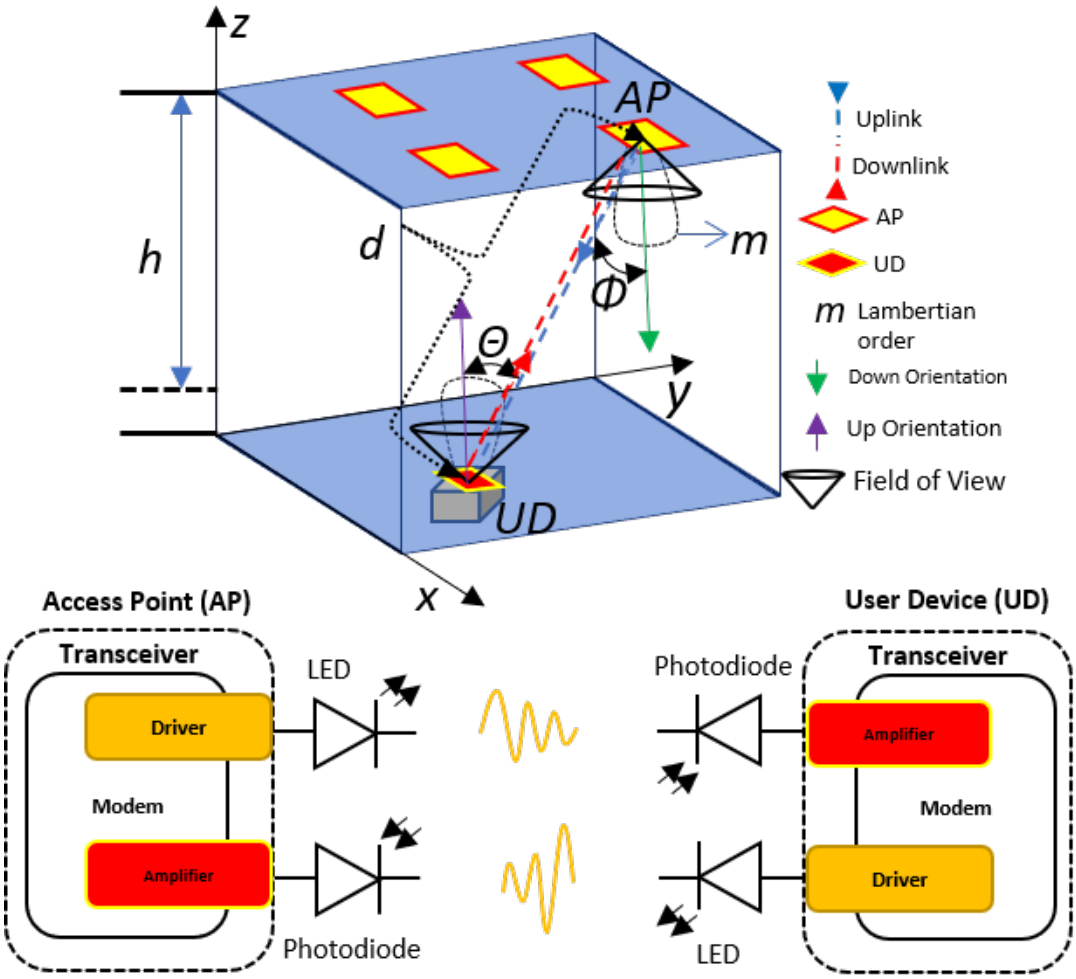

Figure 4.1: Bi-directional VLP system model schematic diagram.

also be exchanged.

4.4 Cramér–Rao Lower Bounds

In this section, we calculate the error bounds to study the effect of SDSN on the performance of the VLP system. Here, different scenarios are considered based on the d relationship with τ^j, and α^j for synchronous and asynchronous scenarios. By observing the interval of the transmitted signal, the log-likelihood function of the received signal

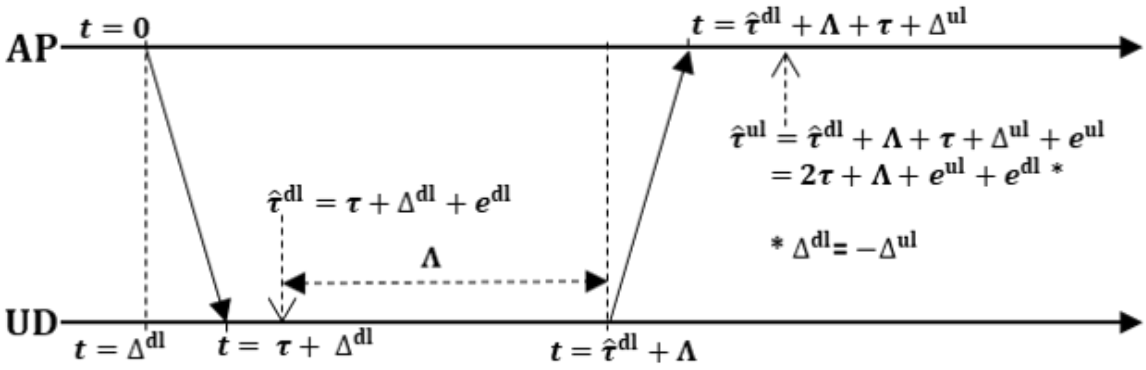

Figure 4.2: The bi-directional synchronization protocol.

can be given as

$$\mathcal{L}(\boldsymbol{\varrho}) = -\frac{1}{2}\ln(2\pi) - \frac{1}{2}\int_{T_1}^{T_2} \ln \sigma_n^2 \left(1 + \alpha^j R_i x_k(t-\tau^j)\zeta_n^2\right) dt \\ -\frac{1}{2\,\sigma_n^2}\int_{T_1}^{T_2} \frac{\left(y_i(t) - \alpha^j R_i\, x_k(t-\tau^j)\right)^2}{(1 + \alpha^j R_i\, x_k(t-\tau^j)\zeta_n^2)} dt, \tag{4.11}$$

where $\boldsymbol{\varrho}$ represents an unknown parameter that needs to be estimated based on the considered scenarios. $\boldsymbol{\mathcal{I}}(\boldsymbol{\varrho})$ is the FIM of $\boldsymbol{\varrho}$, which can be obtained from $\boldsymbol{\mathcal{L}}(\boldsymbol{\varrho})$ as in [33]

$$\boldsymbol{\mathcal{I}}(\boldsymbol{\varrho}) = \mathbb{E}\left\{\left(\nabla_{\boldsymbol{\varrho}}\mathcal{L}(\boldsymbol{\varrho})\right)\left(\nabla_{\boldsymbol{\varrho}}\mathcal{L}(\boldsymbol{\varrho})\right)^T\right\}, \tag{4.12}$$

where $\nabla_{\boldsymbol{\varrho}}$ is the gradient operator. The CRLB is obtained by taking the inverse of the FIM in (4.12). The estimation error covariance can consequently be expressed as

$$\mathbb{E}\{(\hat{\boldsymbol{\varrho}} - \boldsymbol{\varrho})(\hat{\boldsymbol{\varrho}} - \boldsymbol{\varrho})^{\mathrm{T}}\} \succeq \boldsymbol{\mathcal{I}}(\boldsymbol{\varrho})^{-1}, \tag{4.13}$$

where $\boldsymbol{A} \succeq \boldsymbol{B}$ means that $\boldsymbol{A} - \boldsymbol{B} \geq 0$, where ≥ 0 is interpreted as the matrix being positive and semidefinite. More specifically, we discuss three scenarios considering the relationship between d, τ^j and α^j, whether known or unknown. We do this for synchronous and asynchronous estimation.

4.4.1 Bi-directional Distance Estimation

This section studies distance estimation using the bi-directional protocol. With this protocol, the timing bias Δ^j between the AP and UD becomes irrelevant. The TOA parameters τ^{ul} and τ^{dl} are always independent of the channel attenuation factors α^{ul} and α^{dl}, and can hence be treated separately. Now, from the received signals in (4.6), (4.7) and by using (4.12), the FIM of τ^{dl} and τ^{ul} can be derived, following some tedious mathematical derivations, as

$$\begin{aligned}
\boldsymbol{\mathcal{I}}(\tau^{\mathrm{dl}}) &= \mathbb{E}\left\{\left(\frac{\partial \mathcal{L}(\tau^{\mathrm{dl}})}{\partial \tau^{\mathrm{dl}}}\right)^2\right\}, \\
\boldsymbol{\mathcal{I}}(\tau^{\mathrm{ul}}) &= \mathbb{E}\left\{\left(\frac{\partial \mathcal{L}(\tau^{\mathrm{ul}})}{\partial \tau^{\mathrm{ul}}}\right)^2\right\}, \\
\boldsymbol{\mathcal{I}}(\tau^{\mathrm{dl}}) &= \boldsymbol{\mathcal{I}}(\tau^{\mathrm{ul}}) = \left(\frac{R_i \Upsilon_i}{\sigma_n d^{m_k+3}}\right)^2 E_{\mathrm{A}} + \left(\frac{\zeta_n^2 R_i \Upsilon_i}{d^{m_k+3}}\right)^2 E_{\mathrm{AA}},
\end{aligned} \tag{4.14}$$

where E_{A} and E_{AA} are given as

$$E_{\mathrm{A}} \triangleq \int_0^{T_o} \frac{(x_k'(t))^2}{(1+\alpha^j R_i\, x_k(t)\zeta_n^2)} dt, \tag{4.15a}$$

$$E_{\mathrm{AA}} \triangleq \int_0^{T_o} \frac{(x_k'(t))^2}{(1+\alpha^j R_i\, x_k(t)\zeta_n^2)^2} dt. \tag{4.15b}$$

In our analysis, T_o is assumed to be long enough to receive the entire transmitted signal. Assuming that UL and DL communications use the same pilot signal, and that $\phi = \theta$, the FIMs would be the same for both (i.e., $\boldsymbol{\mathcal{I}}(\tau^{\mathrm{ul}}) = \boldsymbol{\mathcal{I}}(\tau^{\mathrm{dl}})$). Then, the variance of the TOA estimation errors are calculated based on the definition as in (4.13)

$$\mathbb{E}\left\{ \left(e^{\mathrm{dl}}\right)^2 \right\} \geq \boldsymbol{\mathcal{I}}^{-1}(\tau^{\mathrm{dl}}),\ \mathbb{E}\left\{ \left(e^{\mathrm{ul}}\right)^2 \right\} \geq \boldsymbol{\mathcal{I}}^{-1}(\tau^{\mathrm{ul}}). \tag{4.16}$$

In order to calculate the CRLB for distance estimation in this scenario, we need to find the FIM of the distance $\boldsymbol{\mathcal{I}}(d)$. Since d is a function of τ, as seen in (4.4), $\boldsymbol{\mathcal{I}}(d)$

can be obtained as a transformation of the FIM of τ. According to (4.8) and (4.9), τ depends on the estimates of τ^{dl} and τ^{ul}. Therefore, to obtain the FIM of τ, we apply the fact that, following the bi-directional protocol, the time delays are independent of any other channel parameters such as α^j. Now, by noting that

$$\begin{aligned}
\tau^{\mathrm{ul}} &= \tau^{\mathrm{dl}} + \Lambda + \tau - \Delta^{\mathrm{ul}}, \\
\tau^{\mathrm{ul}} &= \tau + \Delta^{\mathrm{dl}} + \Lambda + \tau - \Delta^{\mathrm{ul}}, \\
\tau^{\mathrm{ul}} &= 2\tau + \Lambda,
\end{aligned} \tag{4.17}$$

the TOA estimate $\hat{\tau}$ can consequently be given as

$$\hat{\tau} \triangleq \frac{\hat{\tau}^{\mathrm{ul}} - \Lambda}{2} = \tau + \frac{e^{\mathrm{dl}} + e^{\mathrm{ul}}}{2}. \tag{4.18}$$

Applying (4.16) yields

$$\mathbb{E}\left\{ \left(\hat{\tau} - \tau\right)^2 \right\} \geq \frac{1}{4} \left(\boldsymbol{\mathcal{I}}^{-1}(\tau^{\mathrm{dl}}) + \boldsymbol{\mathcal{I}}^{-1}(\tau^{\mathrm{ul}}) \right), \tag{4.19}$$

that is,

$$\boldsymbol{\mathcal{I}}(\tau) = 4 \left(\boldsymbol{\mathcal{I}}^{-1}(\tau^{\mathrm{dl}}) + \boldsymbol{\mathcal{I}}^{-1}(\tau^{\mathrm{ul}}) \right)^{-1}. \tag{4.20}$$

Now, by applying an FIM transformation to $\boldsymbol{\mathcal{I}}(\tau)$, the FIM of $\boldsymbol{\mathcal{I}}(d)$ can be calculated as in [33]

$$\boldsymbol{\mathcal{I}}(d) = \eta \boldsymbol{\mathcal{I}}(\tau) \eta^T, \tag{4.21}$$

where $\eta = 1/c$ is the transformation result from $\tau = d/c$. Thus, $\boldsymbol{\mathcal{I}}(d)$ is given as

$$\boldsymbol{\mathcal{I}}(d) = \boldsymbol{\mathcal{I}}(\tau) \left(\frac{1}{c^2} \right). \tag{4.22}$$

Then, the CRLB can be derived from (4.22) and (4.13) as

$$\text{CRLB} \triangleq \left(\frac{c}{2}\right)^2 \left[\left(\frac{\sigma_n d^{m_{\text{ap}}+3}}{R_{\text{ud}}\Upsilon_{\text{ud}}}\right)^2 \frac{1}{E_{\text{A}} + \zeta_n^4\,\sigma_n^2\,E_{\text{AA}}} + \left(\frac{\sigma_n d^{m_{\text{ud}}+3}}{R_{\text{ap}}\Upsilon_{\text{ap}}}\right)^2 \frac{1}{E_{\text{A}} + \zeta_n^4\,\sigma_n^2\,E_{\text{AA}}} \right]. \tag{4.23}$$

Now, (4.13) shows that as $\zeta_n^2 \to \infty$, the degradation becomes serious. In this case, the CRLB increases greatly as E_{A} in the denominator $\to 0$ and as E_{AA} becomes very small.

4.4.2 Synchronous Directional Distance Estimation

In this section, a perfectly synchronous (i.e., $\Delta^{\text{ul}} = 0$) VLP system under SDSN is studied. The CRLB expressions are obtained by considering only directional communication. As in the previous section, the distance will be estimated at the AP. Then, the TOA parameter τ^{ul} in (4.4) is modeled as

$$\tau^{\text{ul}} = \tau = \frac{d}{c}. \tag{4.24}$$

By using (4.24) and noting that α^{ul} in relation to d as in (4.2), this scenario is termed hybrid (TOA/RSS). The reason for this is that information from both α^{ul} and τ^{ul} is utilized for distance estimation, and α^{ul} is in fact related to RSS. From (4.2) and (4.4), and by considering the estimation of d rather than of τ^j in (4.11), the log-likelihood function in (4.11) can be written as

$$\begin{aligned} \mathcal{L}(\boldsymbol{d}) = &-\frac{1}{2}\ln(2\pi) - \frac{1}{2}\int_{T_1}^{T_2} \ln\sigma_n^2 \left(1 + \Upsilon_{\text{ap}}\, d^{-(m_{\text{ud}}+3)} R_{\text{ap}} x_{\text{ud}}(t - \frac{d}{c})\zeta_n^2\right) dt \\ &- \frac{1}{2\,\sigma_n^2}\int_{T_1}^{T_2} \frac{\left(y_{\text{ap}}(t) - \Upsilon_{\text{ap}}\, d^{-(m_{\text{ud}}+3)}\, R_{\text{ap}}\, x_{\text{ud}}(t - \frac{d}{c})\right)^2}{\left(1 + \Upsilon_{\text{ap}}\, d^{-(m_{\text{ud}}+3)}\, R_{\text{ap}}\, x_{\text{ud}}(t - \frac{d}{c})\,\zeta_n^2\right)} dt. \end{aligned} \tag{4.25}$$

From (4.12) and (4.25), the FIM $\boldsymbol{\mathcal{I}}(d)$ can be derived as

$$\begin{aligned}\boldsymbol{\mathcal{I}}(d) &= \mathbb{E}\left\{\left(\frac{\partial \mathcal{L}(d)}{\partial d}\right)^2\right\}, \\ &= \left(\frac{R_{\rm ap}\,\Upsilon_{\rm ap}}{\sigma_n\, d^{m_{\rm ud}+4}}\right)^2 v_1(d) + \left(\frac{\zeta_n^2\, R_{\rm ap}\,\Upsilon_{\rm ap}}{d^{m_{\rm ud}+4}}\right)^2 v_2(d), \end{aligned} \tag{4.26}$$

where

$$v_1(d) \triangleq (m_{\rm ud}+3)^2 E_{\rm B} + 2(m_{\rm ud}+3)\left(\frac{d}{c}\right) E_{\rm C} + \left(\frac{d}{c}\right)^2 E_A, \tag{4.27a}$$

$$v_2(d) \triangleq (m_{\rm ud}+3)^2 E_{\rm BB} + 2(m_{\rm ud}+3)\left(\frac{d}{c}\right) E_{\rm CC} + \left(\frac{d}{c}\right)^2 E_{\rm AA}, \tag{4.27b}$$

and E_B, E_{BB}, E_C, and E_{CC} are given as

$$E_{\rm B} \triangleq \int_0^{T_o} \frac{(x_{\rm ud}(t))^2}{(1+\alpha^{\rm ul} R_{\rm ap}\, x_{\rm ud}(t)\zeta_n^2)} dt, \tag{4.28a}$$

$$E_{\rm BB} \triangleq \int_0^{T_o} \frac{(x_{\rm ud}(t))^2}{(1+\alpha^{\rm ul} R_{\rm ap}\, x_{\rm ud}(t)\zeta_n^2)^2} dt, \tag{4.28b}$$

$$E_{\rm C} \triangleq \int_0^{T_o} \frac{x_{\rm ud}(t)\, x'_{\rm ud}(t)}{(1+\alpha^{\rm ul} R_{\rm ap}\, x_{\rm ud}(t)\zeta_n^2)} dt, \tag{4.28c}$$

$$E_{\rm CC} \triangleq \int_0^{T_o} \frac{x_{\rm ud}(t)\, x'_{\rm ud}(t)}{(1+\alpha^{\rm ul} R_{\rm ap}\, x_{\rm ud}(t)\zeta_n^2)^2} dt, \tag{4.28d}$$

where E_A and E_{AA} are given as in (4.15) by considering i=AP, k=UD and j=UL. Then, the CRLB is derived from (4.13) and (4.26) as

$$\text{CRLB} \triangleq \left(\frac{\sigma_n\, d^{m_{\rm ud}+4}}{R_{\rm ap}\,\Upsilon_{\rm ap}}\right)^2 \frac{1}{v_1(d) + (\zeta_n^2\,\sigma_n)^2\, v_2(d)}. \tag{4.29}$$

Now, (4.29) shows that as $\zeta_n^2 \to \infty$, the degradation becomes serious. In this case, the CRLB increases significantly as the term $v_1(d)$ in the denominator $\to 0$, and $v_2(d)$ becomes very small. Another important note is that when $\zeta_n^2 = 0$, the CRLB matches perfectly with the one in [28], hence validating the presented analysis.

4.4.3 Asynchronous Directional Distance Estimation

In this section, an asynchronous VLP system under SDSN for directional communication is studied. The CRLB expressions are obtained by only considering directional communication. As in the previous section, the distance will be estimated at the AP. Here, the relationship between τ^{ul} and d as in (4.4) is considered unknown due to the existence of Δ^{ul}. The CRLB expressions are obtained by instead considering the relationship between α^{ul} and d as in (4.2). Therefore, the scenario is called RSS-based distance estimation. Based on this, the unknown parameter in (4.11) becomes a vector of parameters containing $\boldsymbol{\varrho} = (d, \tau^{\mathrm{ul}})$. Furthermore, τ^{ul} is considered a nuisance parameter when calculating the FIM of d. The corresponding log-likelihood function can be written from (4.11) as

$$\begin{aligned}\mathcal{L}(d,\tau^{\mathrm{ul}}) = &-\frac{1}{2}\ln(2\pi) - \frac{1}{2}\int_{T_1}^{T_2} \ln\sigma_n^2\left(1+\Upsilon_{\mathrm{ap}} d^{-(m_{\mathrm{ud}}+3)} R_{\mathrm{ap}}\, x_{\mathrm{ud}}(t-\tau^{\mathrm{ul}})\zeta_n^2\right) dt \\ &- \frac{1}{2\,\sigma_n^2}\int_{T_1}^{T_2} \frac{\left(y_{\mathrm{ap}}(t) - \Upsilon_{\mathrm{ap}}\, d^{-(m_{\mathrm{ud}}+3)}\, R_{\mathrm{ap}}\, x_{\mathrm{ud}}(t-\tau^{\mathrm{ul}})\right)^2}{\left(1+\Upsilon_{\mathrm{ap}}\, d^{-(m_{\mathrm{ud}}+3)}\, R_{\mathrm{ap}}\, x_{\mathrm{ud}}(t-\tau^{\mathrm{ul}})\,\zeta_n^2\right)} dt. \end{aligned} \tag{4.30}$$

Then, the FIM $\boldsymbol{\mathcal{I}}(d,\tau^{\mathrm{ul}})$ can be derived from (4.12) as

$$\boldsymbol{\mathcal{I}}(d,\tau^{\mathrm{ul}}) = \begin{bmatrix} \mathbb{E}\left\{\left(\frac{\partial\mathcal{L}(d,\tau^{\mathrm{ul}})}{\partial d}\right)^2\right\} & \mathbb{E}\left\{\frac{\partial\mathcal{L}(d,\tau^{\mathrm{ul}})}{\partial d}\frac{\partial\mathcal{L}(d,\tau^{\mathrm{ul}})}{\partial \tau^{\mathrm{ul}}}\right\} \\ \mathbb{E}\left\{\frac{\partial\mathcal{L}(d,\tau^{\mathrm{ul}})}{\partial \tau^{\mathrm{ul}}}\frac{\partial\mathcal{L}(d,\tau^{\mathrm{ul}})}{\partial d}\right\} & \mathbb{E}\left\{\left(\frac{\partial\mathcal{L}(d,\tau^{\mathrm{ul}})}{\partial \tau^{\mathrm{ul}}}\right)^2\right\} \end{bmatrix}, \tag{4.31}$$

where

$$\boldsymbol{\mathcal{I}}_{(d,d)} = \left(\frac{R_{\mathrm{ap}}\Upsilon_{\mathrm{ap}}}{\sigma_n d^{m_{\mathrm{ud}}+4}}\right)^2 (m_{\mathrm{ud}}+3)^2\, E_{\mathrm{B}} + \left(\frac{\zeta_n^2 R_{\mathrm{ap}}\Upsilon_{\mathrm{ap}}}{d^{m_{\mathrm{ud}}+4}}\right)^2 (m_{\mathrm{ud}}+3)^2\, E_{\mathrm{BB}}, \tag{4.32a}$$

$$\boldsymbol{\mathcal{I}}_{(d,\tau^{\mathrm{ul}})} = \boldsymbol{\mathcal{I}}_{(\tau^{\mathrm{ul}},d)} = \left(\frac{R_{\mathrm{ap}}\Upsilon_{\mathrm{ap}}}{\sigma_n d^{m_{\mathrm{ud}}+4}}\right)^2 x\,(m_{\mathrm{ud}}+3)\, E_{\mathrm{C}} + \left(\frac{\zeta_n^2 R_{\mathrm{ap}}\Upsilon_{\mathrm{ap}}}{d^{m_{\mathrm{ud}}+4}}\right)^2 x\,(m_{\mathrm{ud}}+3)\, E_{\mathrm{CC}}, \tag{4.32b}$$

$$\boldsymbol{\mathcal{I}}_{(\tau^{\mathrm{ul}},\tau^{\mathrm{ul}})} = \left(\frac{R_{\mathrm{ap}}\Upsilon_{\mathrm{ap}}}{\sigma_n d^{m_{\mathrm{ud}}+4}}\right)^2 d^2\, E_{\mathrm{A}} + \left(\frac{\zeta_n^2\, R_{\mathrm{ap}}\Upsilon_{\mathrm{ap}}}{d^{m_{\mathrm{ud}}+4}}\right)^2 d^2\, E_{\mathrm{AA}}. \tag{4.32c}$$

Noting that τ^{ul} is a nuisance parameter, the effective CRLB of $\hat{d}$ can be calculated from (4.13) and (4.32) as in [33]

$$\begin{aligned}\mathrm{CRLB} &\triangleq \left(\boldsymbol{\mathcal{I}}_{(d,d)} - \boldsymbol{\mathcal{I}}_{(d,\tau^{\mathrm{ul}})}\left(\frac{1}{\boldsymbol{\mathcal{I}}_{(\tau^{\mathrm{ul}},\tau^{\mathrm{ul}})}}\right)\boldsymbol{\mathcal{I}}_{(\tau^{\mathrm{ul}},d)}\right)^{-1} \\ &= \left(\frac{\sigma_n\, d^{m+4}}{\Upsilon_{\mathrm{ap}}\, R_{\mathrm{ap}}\,(m+3)}\right)^2 \frac{E_{\mathrm{A}} + \zeta_n^4\sigma_n^2\, E_{\mathrm{AA}}}{\left(E_{\mathrm{A}} + \zeta_n^4\sigma_n^2\, E_{\mathrm{AA}}\right)\left(E_{\mathrm{B}} + \zeta_n^4\sigma_n^2\, E_{\mathrm{BB}}\right) - \left(E_{\mathrm{C}} + \zeta_n^4\sigma_n^2\, E_{\mathrm{CC}}\right)^2}.\end{aligned} \tag{4.33}$$

Now, when $\zeta_n^2 = 0$, all the terms in (4.33) match perfectly with those in [28], therefore validating the presented analysis.

4.5 Discussion and Evaluation Results

This section explains the performance analysis of all the considered scenarios. Here, we consider the responsivity as well as the effective area of photodetector to be $R_i = 1$ amps/watt, and $W_i = 3 \times 3$ cm^2, respectively. The Lambertian order is $m = 1$, the height $h = 2.5$ m, the AP is 4 m away from the UD, the variance of noise is $\sigma_n^2 = 10^{-10}$, and the practical values for $\zeta_n^2 > 0$ as in [47]. However, the CRLB analysis in this chapter is valid for any value of ζ_n^2. The transmitted signal $x_k(t)$ from (4.5) is modeled as in [28, 34]

$$x_k(t) = A\left(1 - \cos\left(2\pi\, t/T_o\right)\right)\left(1 + \cos(2\pi f_c t)\right), \tag{4.34}$$

where $t \in [0, T_o]$, A represents the average emitted optical power (i.e., source optical power) and f_c denotes the carrier frequency. Here, the power constraints apply directly to the LED input signal (in contrast to electrical transmission models) [47]. The transmitted signal seen in (4.34) is a dc-biased windowed sinusoid, where $A = 30$ dB is applied with a signal duration of $T_o = 10^{-6}$s, and a carrier frequency of $f_c = 100$ MHz. The aforementioned parameters stay the same unless otherwise stated. All transmitted signal energies in (4.15) and (4.34) are calculated numerically.

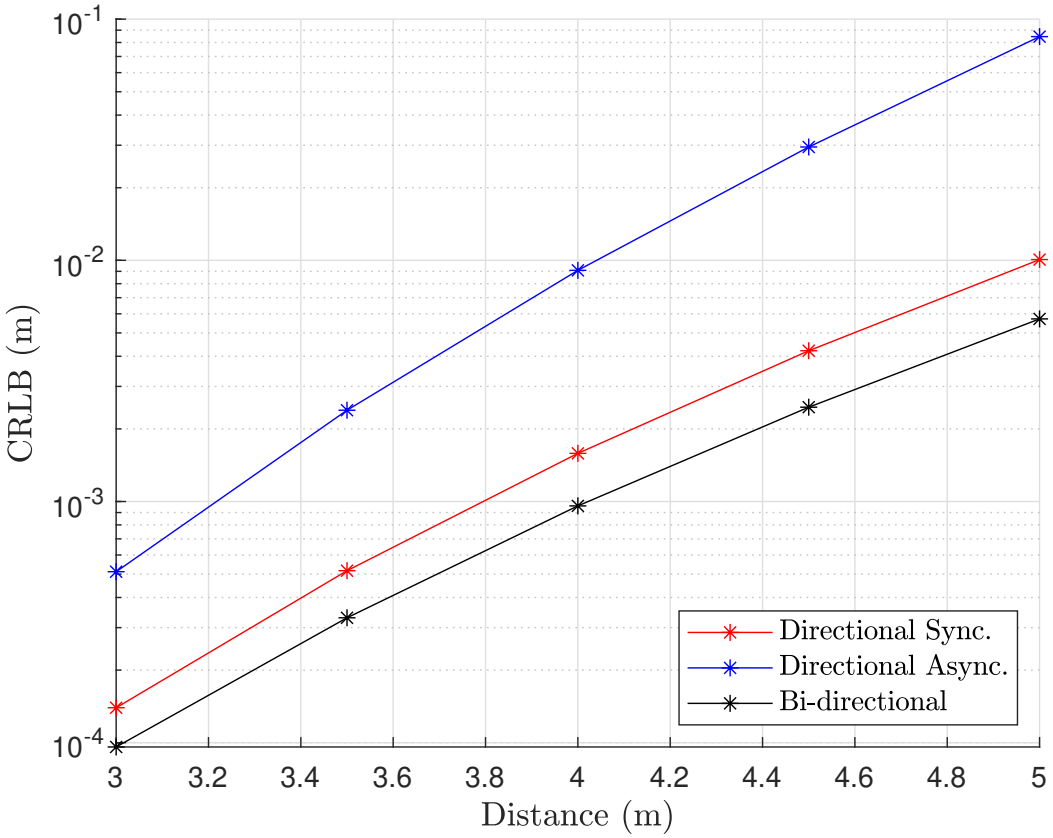

Figure 4.3: CRLB versus distance for directional and bi-directional protocol scenarios, where $\zeta_n^2 = 0$, $f_c = 180$ MHz and $T_o = 10^{-4}$.

Fig. 4.3 illustrates the estimation error bounds of the synchronous and asynchronous directional protocols in [28] along with the bi-directional protocol. As the figure shows, the bi-directional protocol outperforms both directional protocols. This can be explained by noting that the asynchronous protocol depends on the strength of the received signal, which decays as distance increases. Even more, imperfect synchronization increases the value of the CRLB. On the other hand, the bi-directional protocol estimates the TOA at the UD and AP, eliminating the effects of bias between them (i.e., $\Delta^{\text{dl}} = -\Delta^{\text{ul}}$). Moreover, determining τ over the course of two estimations minimizes the error bound. For instance, assuming that $\phi = \theta$, and that the UL and DL communications use the same pilot signal, the same FIMs for both (i.e., $\boldsymbol{\mathcal{I}}(\tau^{\text{ul}}) = \boldsymbol{\mathcal{I}}(\tau^{\text{dl}})$). This reduces the

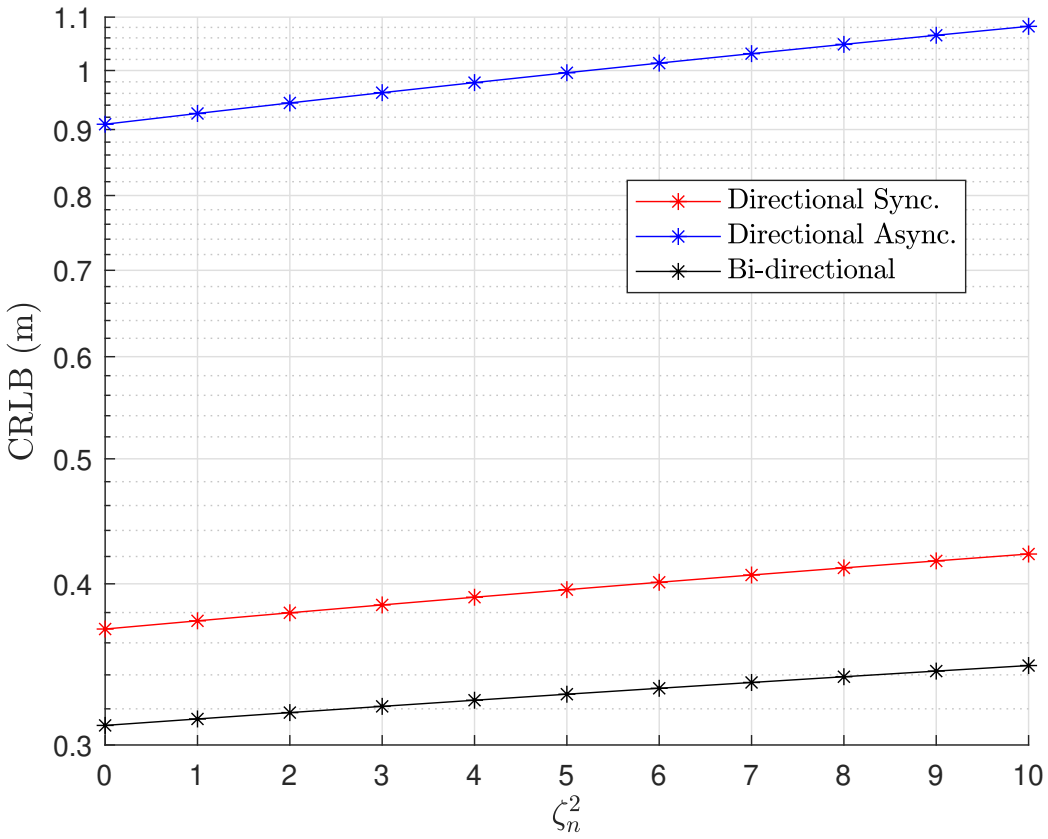

Figure 4.4: CRLB versus ζ_n^2 for directional and bi-directional protocol scenarios.

CRLB when compared to the synchronous protocol in (4.19).

Fig. 4.4 studies the impact of ζ_n^2 on the CRLB s. As evident from this figure, the CRLB for each scenario has the lowest value when $\zeta_n^2 = 0$ (i.e., no SDSN), and the performance degrades as ζ_n^2 increases. Moreover, the result here agrees with the one in Fig. 4.3, where the bi-directional protocol has the lowest CRLB for all values of all ζ_n^2. For instance, when $\zeta_n^2 = 0$, the bi-directional protocol shows an improvement of almost 60 cm and 6 cm over the asynchronous and synchronous directional scenarios, respectively. Similarly, when $\zeta_n^2 = 10$, the CRLB for the bi-directional protocol scenario still outperforms the directional protocols by 74 cm and 8 cm, respectively.

Fig. 4.5 illustrates the performance degradation of all considered scenarios due to

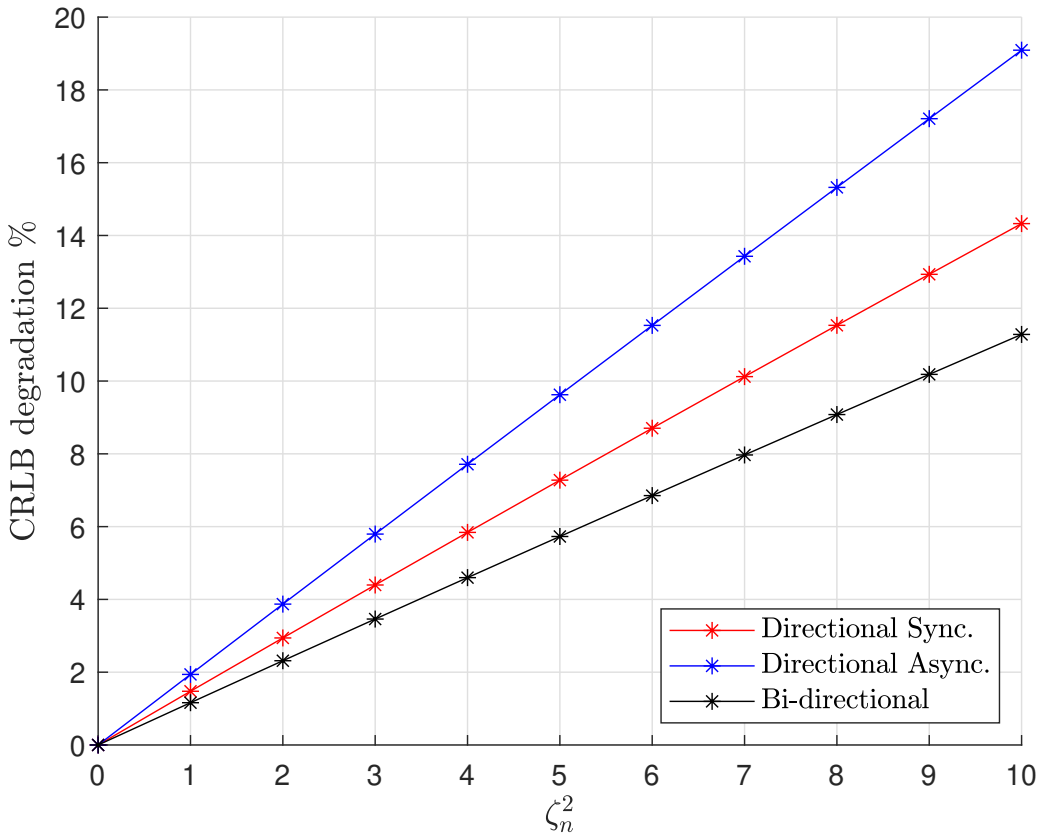

Figure 4.5: CRLB degradation % versus ζ_n^2 for directional and bi-directional protocol scenarios.

the presence of SDSN ζ_n^2. The CRLB degradation is calculated as

$$\text{CRLB}_{\text{deg}} = \left(\frac{\text{CRLB}_{\zeta_n^2}}{\text{CRLB}_{\zeta_n^2 = 0}} - 1 \right) \times 100\%. \tag{4.35}$$

where each scenario's CRLB is obtained using (4.23), (4.29), and (4.33). The synchronous directional protocol shows the worst performance with degradation level close to 20% when $\zeta_n^2 = 10$, then the asynchronous directional and bi-directional protocol with degradation levels close to 14% and 12%, respectively. This can be interpreted by nothing that as RSSincreases, the SDSN will have a significant effect on distance estimation of asynchronous and synchronous directional protocols, as both of these protocols use α

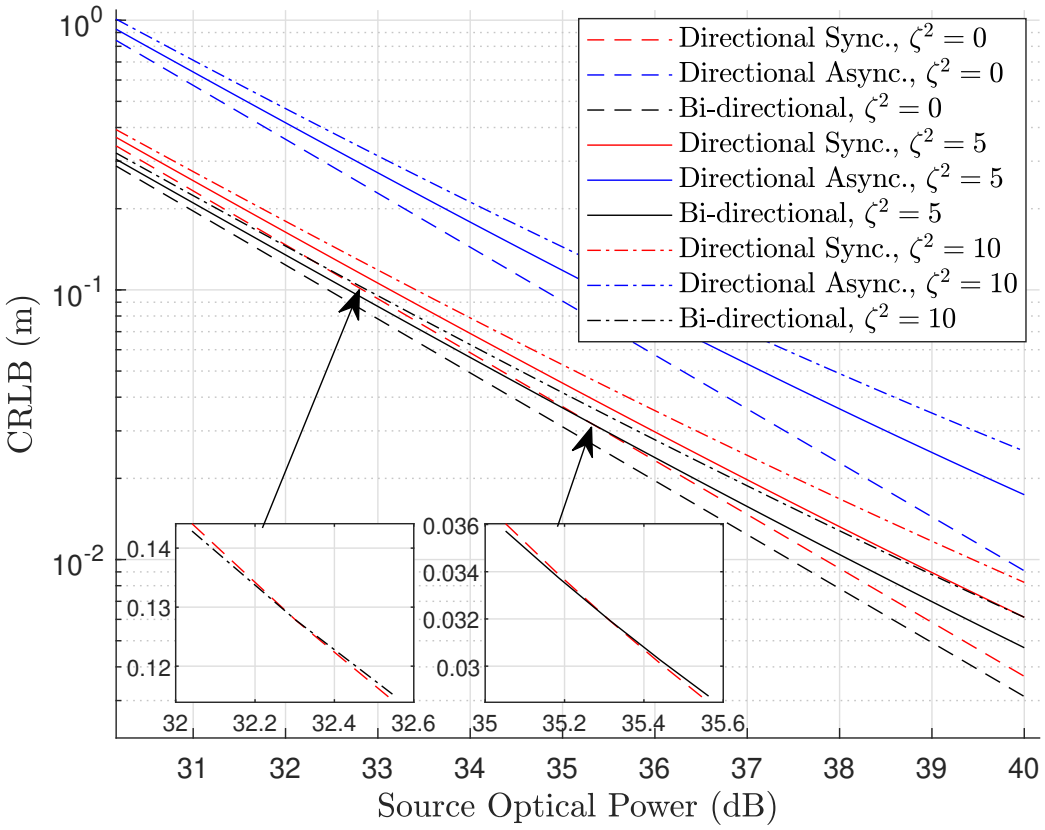

Figure 4.6: CRLB versus source optical power for directional and bi-directional protocol scenarios.

whereas bi-directional only consider τ. However, the energy cost for sending only one transmitted ranging signal in directional scenarios is lower than bi-directional one.

Finally, the impact of ζ_n^2 when increasing the average transmitted optical power is studied in Fig. 6. The CRLB s for all scenarios considering $\zeta_n^2 \in \{0, 5, 10\}$ are plotted against the source's optical power A. As expected, the CRLB s for all the scenarios improve as the power increases. In addition, the asynchronous directional protocol demonstrates the poorest performance for the studied energy values. Interestingly, in all the scenarios, SDSN minimizes the effect of increasing the source power. For example, in the bi-directional protocol, the power gain between $\zeta_n^2 = 0$ and $\zeta_n^2 = 10$ decreases by 0.5 dB when the CRLB $=10^{-1}$. This gain becomes 1 dB when the CRLB $= 10^{-2}$.

Furthermore, due to the impact of SDSN, there is a point where the performance of the bi-directional protocol, at $\zeta_n^2 = 10$, is eclipsed by that of the synchronous directional protocol, at $\zeta_n^2 = 0$. This can be observed in the subplot where the black and red lines intersect (i.e., the bi-directional protocol demonstrates better performance before a source optical power of 32.3 dB, and poorer performance afterward). The same behaviour can be observed between the bi-directional protocol at $\zeta_n^2 = 5$ and the synchronous directional protocol at $\zeta_n^2 = 0$. In this case, the point of intersection shifts to the right and becomes 35.3 dB.

4.6 Conclusion

This chapter addresses two points. First, we consider the effect of SDSN on distance estimation bounds in VLC systems. Second, we exploited a bi-directional synchronization protocol that can eliminate time biasing between the LED transmitter and photodetector receiver. The results indicate that SDSN significantly impacts the CRLB s for both the synchronous and asynchronous protocols. However, the bi-directional protocol shows impressive performance compared to that of the directional protocol. Proposing estimators that correspond to the CRLB 's performance in a system under the effects of SDSN can be considered in future work.

Chapter 5

Synchronous, Asynchronous and Quasi-Synchronous Visible Light Positioning under Signal-Dependent Shot Noise

5.1 Introduction and Related Works

There has been a substantial enthusiasm in the literature towards VLC based positioning techniques. VLP systems have demonstrated better positioning accuracy than RF based positioning, global positioning, and other existing systems. The VLP system has many advantages due to the inherent properties of VLC [25]. Furthermore, VLP systems are used in scenarios where RF communication is subjected to multipath fading or RF-inappropriate environments (e.g., underwater and underground) and where electromagnetic radiations are not permitted (e.g., aeroplanes and hospital MRI rooms) [25,26].

The VLP system's performance is traditionally evaluated in the literature by calculating the CRLB, which is the benchmark for providing theoretical limits on 3D position

estimation accuracy. The CRLB offers a lower bound for the variance of any unbiased estimator [33]. The works in [28,34,36] calculated the CRLBs for the distance and 3D position estimations in synchronous VLC systems using TOA measurements, whereas [39] carried out performance analysis for a technique using TDOA. In addition, several works investigated asynchronous VLC systems using RSS based methods [28, 35, 37, 38, 40–43].

Despite their powerful properties, VLP systems face numerous challenges, including but are not limited to: 1) SDSN, which is the noise generated by the LED's transmitted signal at the receiver, 2) thermal noise, caused by light signal amplification and the photodetector's load, 3) the visible light multipath effect, which is caused by reflection, refraction, and scattering from objects such as glass walls or human clothing, rendering the FOV and LOS path requirements critical for position accuracy at room edges, and 4) synchronization error, which is caused due to a timing bias between transmitting and receiving clocks. There are other reasons such as LED tilt position, signal collisions, and mobility issues [17, 25, 26].

The effect of SDSN on VLP accuracy limits was studied in [34,35,38,41,42]; however, these works did not consider time dependency and therefore treated SDSN as an additive white Gaussian noise (AWGN) with fixed variance. This is not reflective of the true nature of SDSN. To the best of the authors' knowledge, the literature has yet to consider the time dependency of SDSN when calculating the error bounds for 3D positioning in VLC systems. Based on this, and motivated by the importance and timeliness of this topic, this chapter aims to calculate the bounds of VLP systems under the effects of SDSN in different scenarios. More specifically, for synchronous, asynchronous, and quasi-synchronous VLC systems, the position estimation CRLBs are calculated using hybrid (TOA/RSS), hybrid (TDOA/RSS), and RSS parameters.

The rest of the chapter is organized as follows: Section 5.2 describes the setup of the VLP system under the effect of SDSN and thermal noises. Section 5.3, evaluate the CRLB for synchronous, quasi-synchronous, and asynchronous scenarios. Evaluation and performance analysis are presented in Section 5.4 to explain the theoretical results,

where comparative analysis is presented among the various CRLBs. Finally, Section 5.5 provides concluding remarks.

5.2 System Description

This study considers a DL VLC system with IM/DD. The transmitter side employs a number of LEDs and the VLC receiver side has a single photodetector as shown in Fig. 5.1. Our VLP system is based on LOS VLC with no multipath transmission, where the photodetector receiver lies in the FOV of the light signal emitted by the LED transmitters, keeping in line with the VLP system's models in the literature [28, 34–36, 38, 40, 42].

In order to avoid signal collision between the LED transmitters, VLC system utilizes a multiple access protocol (e.g., TDMA and FDMA) [17]. Furthermore, the ith LED transmitted signal is received at the photodetector receiver, which converts the optical signal to electrical signal. The output signal at the photodetector receiver side is a delayed attenuated version of the transmitted pilot signal corrupted by the thermal noise and SDSN, which can be expressed as in [47, 129]

$$r_i(t) = \alpha_i R\, x_i(t-\tau_i) + \sqrt{\alpha_i R\, x_i(t-\tau_i)}\, \xi_{\mathrm{sh}_i}(t) + \xi_{\mathrm{th}_i}(t) \tag{5.1}$$

where $i \in \{1, \ldots, L_{\mathrm{T}}\}$ and L_{T} is the number of LED transmitters. The optical channel attenuation factor is represented by α_i, and it has real positive value ($\alpha_i > 0$). R denotes the photodetector's responsivity, which is assumed to be constant over the optical bandwidth of the transmitted pilot signal. $x_i(t)$ is the transmitted pilot signal used for position estimation and $t \in [T_{1,i}, T_{2,i}]$, here the observation interval is determined by $T_{1,i}$ and $T_{2,i}$, which completely contains the signal emitted by the ith LED transmitter. The TOA of the transmitted pilot signal by the ith LED at the photodetector receiver is represented by τ_i. $\sqrt{\alpha_i R_P\, x_i(t-\tau_i)}\, \xi_{\mathrm{sh_i}}(t)$ is the SDSN term and $\xi_{\mathrm{th}_i}(t)$ is the

signal-independent thermal noise, both noises can be modeled as AWGN, and the SDSN variance is dependent on the input signal [47, 129]. The elements $\left(\xi_{\mathrm{sh}_1}(t), \cdots, \xi_{\mathrm{sh}_{L_\mathrm{T}}}(t)\right)$ and $\left(\xi_{\mathrm{th}_1}(t), \cdots, \xi_{\mathrm{th}_{L_\mathrm{T}}}(t)\right)$ are modeled to be as independent and identically distributed (i.i.d.) random variables (RV) due to the statistics of the additive noise, implying that the SDSN $\xi_{\mathrm{sh}_i}(t) \sim N(0, \zeta_n^2\sigma_n^2)$[1], where the term $\zeta_n^2 > 0$ describes the ratio between the variances of SDSN and thermal noise $\xi_{\mathrm{th}_i}(t) \sim N(0, \sigma_n^2)$ [47].

The DL optical wireless channel attenuation factor α_i in (5.1) can be modeled as in [46, 130]

$$\begin{aligned}\alpha_i =& \frac{(m_i+1)\,W}{2\pi d_i^2}\cos^{m_i}(\phi_i)\cos(\theta_i),\\ \alpha_i =& -\frac{(m_i+1)\,W}{2\pi d_i^2}\frac{\left[(\boldsymbol{P}_\mathrm{r}-\boldsymbol{P}_\mathrm{t}^i)^T\boldsymbol{n}_\mathrm{t}^i\right]^{m_i}}{\|\boldsymbol{P}_\mathrm{r}-\boldsymbol{P}_\mathrm{t}^i\|^{m_i}}\frac{(\boldsymbol{P}_\mathrm{r}-\boldsymbol{P}_\mathrm{t}^i)^T\boldsymbol{n}_\mathrm{r}}{\|\boldsymbol{P}_\mathrm{r}-\boldsymbol{P}_\mathrm{t}^i\|},\end{aligned} \tag{5.2}$$

where m_i is the ith LED's Lambertian order, which depends on the approximate Lambertian model $m = -\left(ln\,2/ln(\cos\theta_{\frac{1}{2}})\right)$. The photodetector's effective area is represented by W. The euclidean distance between the photodetector receiver and the ith LED transmitter is represented by $d_i = \|\boldsymbol{P}_\mathrm{r} - \boldsymbol{P}_\mathrm{t}^i\|^2$, where the photodetector receiver and the ith LED transmitter positions are represented by $\boldsymbol{P}_\mathrm{r} = [P_{\mathrm{r,x}}\ P_{\mathrm{r,y}}\ P_{\mathrm{r,z}}]^T$ and $\boldsymbol{P}_\mathrm{t}^i = \left[P_{\mathrm{t,x}}^i\ P_{\mathrm{t,y}}^i\ P_{\mathrm{t,z}}^i\right]^T$, respectively. ϕ_i and θ_i are arbitrary orientation angles with respective orientation vectors $\boldsymbol{n}_\mathrm{t}^i = [n_{\mathrm{t,x}}^i\ \ n_{\mathrm{t,y}}^i\ \ n_{\mathrm{t,z}}^i]^T$ and $\boldsymbol{n}_\mathrm{r} = [n_{\mathrm{r,x}}\ \ n_{\mathrm{r,y}}\ \ n_{\mathrm{r,z}}]^T$ for the ith LED transmitter and the photodetector receiver. The photodetector receiver must be in the FOV of the optical wireless signal emitted by the ith LED transmitter to have LOS communication as shown in Fig. 5.1.

In (1), the TOA parameter is modeled as

$$\tau_i = \frac{\|\boldsymbol{P}_\mathrm{r} - \boldsymbol{P}_\mathrm{t}^i\|}{c} + \Delta_i, \tag{5.3}$$

where c represents the speed of light. The photodetector receiver has a timing bias

[1] $N(\mu, \sigma_n^2)$ represents the Gaussian distributed RV with μ mean and σ_n^2 variance.
[2] $\|\cdot\|$ is the Euclidean norm of the vector

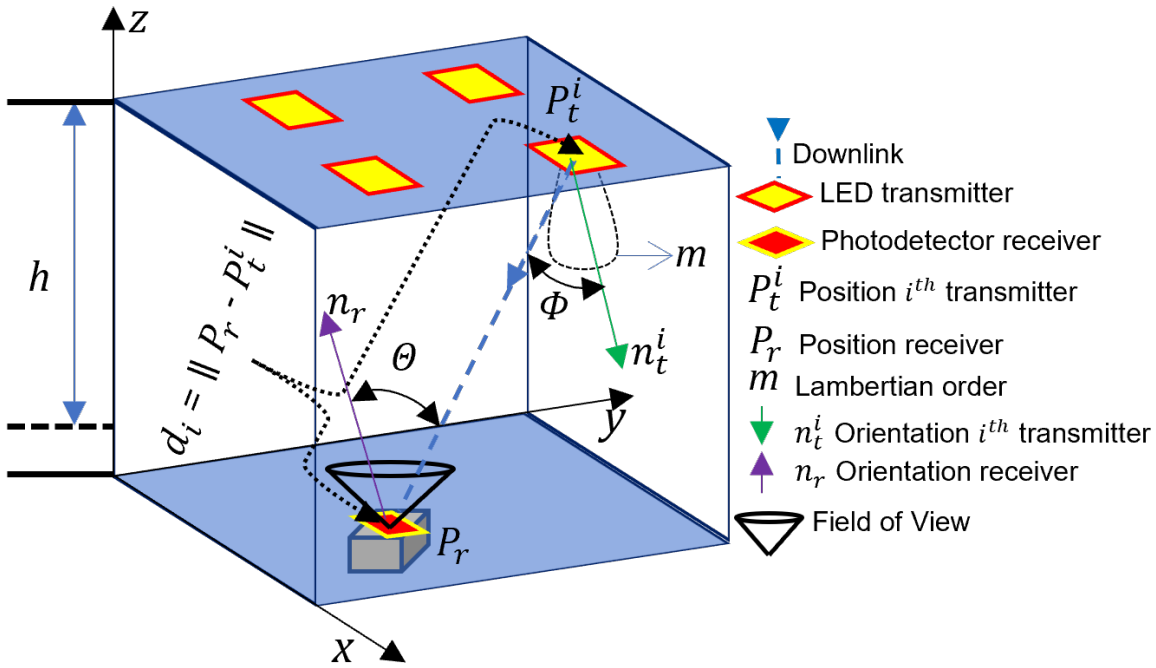

Figure 5.1: The 3D VLP system model schematic diagram.

Δ_i for $i \in \{1, \ldots, L_{\mathrm{T}}\}$ with respect to the ith LED transmitter clocks. Moreover, for asynchronous VLP system Δ_i for each LED transmitter is modeled as an unknown deterministic parameter, in which case timing bias exists between the LED transmitters themselves and between the photodetector receiver and each LED transmitter. In case of synchronous VLP systems, $\tau_i = \frac{\|\boldsymbol{P}_{\mathrm{r}} - \boldsymbol{P}_{\mathrm{t}}^i\|}{c}$ for $i \in \{1, \ldots, L_{\mathrm{T}}\}$ considering $\Delta_i = 0$ suggesting no clock offset between the ith LED transmitter and the photodetector receiver as they are fully synchronized to a reference clock. However, in quasi-synchronous VLP systems, $\Delta_i = \Delta$ is modeled as an unknown deterministic parameter indicating that synchronization exists among all the LED transmitters using a common reference clock but the photodetector receiver has a timing bias towards it, therefore $\tau_i = \frac{\|\boldsymbol{P}_{\mathrm{r}} - \boldsymbol{P}_{\mathrm{t}}^i\|}{c} + \Delta$ for $i \in \{1, \ldots, L_{\mathrm{T}}\}$.

The received signal $r_i(t)$ in (5.1) can be re-written in the form

$$y_i(t) = \alpha_i R\, x_i(t - \tau_i) + \Omega_i(t), \tag{5.4}$$

Here $\Omega_i(t) \sim N(0, \Gamma_i)$, where $\Gamma_i = \sigma_n^2 \left(1 + \alpha_i \, R \, x_i(t - \tau_i)\zeta_n^2\right)$. The system model assume that the W, R, n_{r}, m_i, P_{t}^i, n_{t}^i, and $x_i(t)$ for all $i \in \{1, \ldots, L_{\mathrm{T}}\}$ are known at the photodetector receiver.

5.3 Cramér–Rao Lower Bounds

In this section, we study the 3D positioning error bounds when the VLC system is under the effect of the SDSN. We calculate the CRLBs for synchronous, quasi-synchronous, and asynchronous scenarios depending on τ_i, and α_i information when the VLP system is under the effect of the SDSN. The PDF of the received signal model in (5.4) can be written as

$$f(Y(t))|P_{\mathrm{r}}) = \frac{1}{\sqrt{2\pi\Gamma_i}} \exp\left(-\frac{1}{2\Gamma_i}\left(Y(t) - \alpha_i R \, x_i(t - \tau_i)\right)^2\right). \tag{5.5}$$

The joint PDF for the received signal vector $\boldsymbol{Y}(t) \triangleq [y_1(t) \ldots y_{L_{\mathrm{T}}}(t)]^T$ can be written as

$$f(y_i(t))|P_{\mathrm{r}}) = \left(\prod_{i=1}^{L_{\mathrm{T}}} \frac{1}{\sqrt{2\pi\Gamma_i}}\right) \exp\left(-\frac{1}{2}\sum_{i=1}^{L_{\mathrm{T}}} \frac{\left(y_i(t) - \alpha_i R \, x_i(t - \tau_i)\right)^2}{\Gamma_i}\right). \tag{5.6}$$

Now, by observing the interval of the ith transmitted signal, the log-likelihood of (5.6) can be given as

$$\begin{aligned}\mathcal{L}\left(\boldsymbol{\varrho}\right) = &- \frac{L_{\mathrm{T}}}{2}\ln\left(2\,\pi\right) - \frac{1}{2}\sum_{i=1}^{L_{\mathrm{T}}}\int_{T_{1,i}}^{T_{2,i}} \ln\, \sigma_n^2\left(1 + \alpha_i R x_i(t - \tau_i)\zeta_n^2\right) dt \\ &- \frac{1}{2}\sum_{i=1}^{L_{\mathrm{T}}}\int_{T_{1,i}}^{T_{2,i}} \frac{\left(y_i(t) - \alpha_i R x_i(t - \tau_i)\right)^2}{\sigma_n^2\left(1 + \alpha_i R x_i(t - \tau_i)\zeta_n^2\right)} dt,\end{aligned} \tag{5.7}$$

where $\boldsymbol{\varrho}$ represents the set of unknown parameters that needs to be estimated including P_r and other nuisance parameters. These depend on the considered scenarios, as investigated in the upcoming pages.

The Fisher information matrix (FIM) of $\boldsymbol{\varrho}$ can be obtained from $\mathcal{L}(\boldsymbol{\varrho})$ as in [33]

$$\boldsymbol{\mathcal{I}}(\boldsymbol{\varrho}) = \mathbb{E}\left\{\left(\nabla_{\boldsymbol{\varrho}}\mathcal{L}(\boldsymbol{\varrho})\right)\left(\nabla_{\boldsymbol{\varrho}}\mathcal{L}(\boldsymbol{\varrho})\right)^{T}\right\}, \tag{5.8}$$

where $\nabla_{\boldsymbol{\varrho}}$ is the gradient operator. The CRLB is obtained by taking the inverse of the FIM in (5.8). The estimation error covariance can consequently be expressed as

$$\mathbb{E}\big\{(\hat{\boldsymbol{\varrho}} - \boldsymbol{\varrho})(\hat{\boldsymbol{\varrho}} - \boldsymbol{\varrho})^{\mathrm{T}}\big\} \succeq \boldsymbol{\mathcal{I}}(\boldsymbol{\varrho})^{-1}. \tag{5.9}$$

$\boldsymbol{A} \succeq \boldsymbol{B}$ means that $\boldsymbol{A} - \boldsymbol{B} \geq 0$, where ≥ 0 relevant interpretation is that the matrix is positive and semidefinite [33]. Now, we discuss the CRLBs for three different scenarios depending on the available τ_i and α_i information. We have done this for synchronous, quasi-synchronous and asynchronous estimation.

5.3.1 3D Positioning Estimation in Synchronous System

This scenario studies a perfectly synchronous (i.e., the timing bias $\Delta_i = 0$ in (5.3) for $i \in \{1, \ldots, L_{\mathrm{T}}\}$) VLP system. In this case, the TOA τ_i and the channel attenuation factor α_i parameters information are available. Therefore, τ_i and α_i are functions of $\boldsymbol{P}_{\mathrm{r}}$. This scenario is termed hybrid (TOA/RSS) because the information from both τ_i and α_i is used for 3D position estimation. It is also worth mentioning that α_i is related to RSS.

From (5.2), (5.3), and (5.4) the vector containing the set of unknown parameters in (5.7) becomes $\boldsymbol{\varrho} = [P_{r,x}\ P_{r,y}\ P_{r,z}]^{T} = \boldsymbol{P}_{\mathrm{r}}$. Now, the FIM $\boldsymbol{\mathcal{I}}(\boldsymbol{\varrho})$ is derived from (5.7) and (5.8) to be

$$[\mathcal{I}(\boldsymbol{\varrho})] = \mathbb{E}\left\{\frac{\partial\mathcal{L}(\boldsymbol{\varrho})}{\partial\varrho}\frac{\partial\mathcal{L}(\boldsymbol{\varrho})}{\partial\varrho}\right\}, \tag{5.10}$$

where $[\mathcal{I}(\boldsymbol{\varrho})]$ is a 3×3 matrix with elements as follows:

$$[\mathcal{I}(\boldsymbol{\varrho})]_{v_1,v_2} = R^2\,\zeta_n^4 \sum_{i=1}^{L_\mathrm{T}} \Bigg(\frac{\partial \alpha_i}{\partial P_{\mathrm{r},v_1}} \frac{\partial \alpha_i}{\partial P_{\mathrm{r},v_2}} \int_{T_{1,i}}^{T_{2,i}} \frac{x_i^2(t-\tau_i)}{(1+\alpha_i R\, x_i(t-\tau_i)\zeta_n^2)^2} dt + \alpha_i \frac{\partial \alpha_i}{\partial P_{\mathrm{r},v_1}}$$
$$\times \int_{T_{1,i}}^{T_{2,i}} \frac{x_i(t-\tau_i)}{(1+\alpha_i R\, x_i(t-\tau_i)\zeta_n^2)^2} \frac{\partial x_i(t-\tau_i)}{\partial P_{\mathrm{r},v_2}} dt + \alpha_i \frac{\partial \alpha_i}{\partial P_{\mathrm{r},v_2}} \int_{T_{1,i}}^{T_{2,i}} \frac{x_i(t-\tau_i)}{(1+\alpha_i R\, x_i(t-\tau_i)\zeta_n^2)^2}$$
$$\times \frac{\partial x_i(t-\tau_i)}{\partial P_{\mathrm{r},v_1}} dt + \alpha_i^2 \int_{T_{1,i}}^{T_{2,i}} \frac{\partial x_i(t-\tau_i)}{\partial P_{\mathrm{r},v_1}} \frac{1}{(1+\alpha_i R\, x_i(t-\tau_i)\zeta_n^2)^2} \frac{\partial x_i(t-\tau_i)}{\partial P_{\mathrm{r},v_2}} dt \Bigg) + \frac{R^2}{\sigma_n^2} \sum_{i=1}^{L_\mathrm{T}}$$
$$\Bigg(\frac{\partial \alpha_i}{\partial P_{\mathrm{r},v_1}} \frac{\partial \alpha_i}{\partial P_{\mathrm{r},v_2}} \int_{T_{1,i}}^{T_{2,i}} \frac{x_i^2(t-\tau_i)}{(1+\alpha_i R\, x_i(t-\tau_i)\zeta_n^2)} dt + \alpha_i \frac{\partial \alpha_i}{\partial P_{\mathrm{r},v_1}} \int_{T_{1,i}}^{T_{2,i}} \frac{x_i(t-\tau_i)}{(1+\alpha_i R\, x_i(t-\tau_i)\zeta_n^2)}$$
$$\times \frac{\partial x_i(t-\tau_i)}{\partial P_{\mathrm{r},v_2}} dt + \alpha_i \frac{\partial \alpha_i}{\partial P_{\mathrm{r},v_2}} \int_{T_{1,i}}^{T_{2,i}} \frac{x_i(t-\tau_i)}{(1+\alpha_i R\, x_i(t-\tau_i)\zeta_n^2)} \frac{\partial x_i(t-\tau_i)}{\partial P_{\mathrm{r},v_1}} dt + \alpha_i^2$$
$$\times \int_{T_{1,i}}^{T_{2,i}} \frac{\partial x_i(t-\tau_i)}{\partial P_{\mathrm{r},v_1}} \frac{1}{(1+\alpha_i R\, x_i(t-\tau_i)\zeta_n^2)} \frac{\partial x_i(t-\tau_i)}{\partial P_{\mathrm{r},v_2}} dt \Bigg), \tag{5.11}$$

where $v_1, v_2 \in \{x, y, z\}$ with

$$\frac{\partial x_i(t-\tau_i)}{\partial P_{\mathrm{r},v_{(1|2)}}} = x_i'(t-\tau_i) \left(-\frac{\partial \tau_i}{\partial P_{\mathrm{r},v_{(1|2)}}} \right), \tag{5.12}$$

$$\frac{\partial \tau_i}{\partial P_{\mathrm{r},v_{(1|2)}}} = \frac{P_{\mathrm{r},v_{(1|2)}} - P^i_{\mathrm{t},v_{(1|2)}}}{c\|\boldsymbol{P}_\mathrm{r} - \boldsymbol{P}^i_\mathrm{t}\|}, \tag{5.13}$$

$$\frac{\partial \alpha_i}{\partial P_{\mathrm{r},v_{(1|2)}}} = -\frac{(m_i+1)\,W}{2\pi} \Bigg(\frac{\left[(\boldsymbol{P}_\mathrm{r} - \boldsymbol{P}^i_\mathrm{t})^T \boldsymbol{n}^i_\mathrm{t}\right]^{m_i-1}}{\|\boldsymbol{P}_\mathrm{r} - \boldsymbol{P}^i_\mathrm{t}\|^{m_i+3}}$$
$$\times \left(m_i\, n^i_{\mathrm{t},v_{(1|2)}} (\boldsymbol{P}_\mathrm{r} - \boldsymbol{P}^i_\mathrm{t})^T \boldsymbol{n}_\mathrm{r} + n_{\mathrm{r},v_{(1|2)}} (\boldsymbol{P}_\mathrm{r} - \boldsymbol{P}^i_\mathrm{t})^T \boldsymbol{n}^i_\mathrm{t} \right)$$
$$- \frac{(m_i+3)(P_{\mathrm{r},v_{(1|2)}} - P^i_{\mathrm{t},v_{(1|2)}})}{\|\boldsymbol{P}_\mathrm{r} - \boldsymbol{P}^i_\mathrm{t}\|^{m_i+5}} \left((\boldsymbol{P}_\mathrm{r} - \boldsymbol{P}^i_\mathrm{t})^T \boldsymbol{n}^i_\mathrm{t} \right)^{m_i} (\boldsymbol{P}_\mathrm{r} - \boldsymbol{P}^i_\mathrm{t})^T \boldsymbol{n}_\mathrm{r} \Bigg). \tag{5.14}$$

Now, (5.11) can be written as

$$[\mathcal{I}_{\mathrm{sync}}]_{v_1,v_2} = \frac{R^2}{\sigma_n^2} \Bigg(\zeta_n^4\, \sigma_n^2 \sum_{i=1}^{L_\mathrm{T}} \Bigg(\frac{\partial \alpha_i}{\partial P_{\mathrm{r},v_1}} \frac{\partial \alpha_i}{\partial P_{\mathrm{r},v_2}} E^i_{BB} + \alpha_i^2 \frac{\partial \tau_i}{\partial P_{\mathrm{r},v_1}} \frac{\partial \tau_i}{\partial P_{\mathrm{r},v_2}} E^i_{AA}$$
$$- \alpha_i \left(\frac{\partial \alpha_i}{\partial P_{\mathrm{r},v_1}} \frac{\partial \tau_i}{\partial P_{\mathrm{r},v_2}} + \frac{\partial \tau_i}{\partial P_{\mathrm{r},v_1}} \frac{\partial \alpha_i}{\partial P_{\mathrm{r},v_2}} \right) E^i_{CC} \Bigg)$$

$$+\sum_{i=1}^{L_{\mathrm{T}}}\Bigg(\frac{\partial\alpha_i}{\partial P_{\mathrm{r},v_1}}\frac{\partial\alpha_i}{\partial P_{\mathrm{r},v_2}}E_B^i+\alpha_i^2\frac{\partial\tau_i}{\partial P_{\mathrm{r},v_1}}\frac{\partial\tau_i}{\partial P_{\mathrm{r},v_2}}E_A^i$$
$$-\alpha_i\left(\frac{\partial\alpha_i}{\partial P_{\mathrm{r},v_1}}\frac{\partial\tau_i}{\partial P_{\mathrm{r},v_2}}+\frac{\partial\tau_i}{\partial P_{\mathrm{r},v_1}}\frac{\partial\alpha_i}{\partial P_{\mathrm{r},v_2}}\right)E_C^i\Bigg)\Bigg), \tag{5.15}$$

where

$$E_{\mathrm{A}}^i \triangleq \int_0^{T_{0,i}}\frac{\left(x_i'(t)\right)^2}{(1+\alpha_i R\, x_i(t)\zeta_n^2)}dt, \tag{5.16a}$$
$$E_{\mathrm{AA}}^i \triangleq \int_0^{T_{0,i}}\frac{\left(x_i'(t)\right)^2}{(1+\alpha_i R\, x_i(t)\zeta_n^2)^2}dt, \tag{5.16b}$$
$$E_{\mathrm{B}}^i \triangleq \int_0^{T_{0,i}}\frac{\left(x_i(t)\right)^2}{(1+\alpha_i R\, x_i(t)\zeta_n^2)}dt, \tag{5.16c}$$
$$E_{\mathrm{BB}}^i \triangleq \int_0^{T_{0,i}}\frac{\left(x_i(t)\right)^2}{(1+\alpha_i R\, x_i(t)\zeta_n^2)^2}dt, \tag{5.16d}$$
$$E_{\mathrm{C}}^i \triangleq \int_0^{T_{0,i}}\frac{x_i(t)\,x_i'(t)}{(1+\alpha_i R\, x_i(t)\zeta_n^2)}dt, \tag{5.16e}$$
$$E_{\mathrm{CC}}^i \triangleq \int_0^{T_{0,i}}\frac{x_i(t)\,x_i'(t)}{(1+\alpha_i R\, x_i(t)\zeta_n^2)^2}dt. \tag{5.16f}$$

Here, it is assumed that for an observation interval of $[0, T_{\mathrm{o},i}]$, $x_i(t)$ is real and positive. The terms $\partial\tau_i/\partial P_{\mathrm{r},v_{(1|2)}}$, and $\partial\alpha_i/\partial P_{\mathrm{r},v_{(1|2)}}$ in (5.13), and (5.14) illustrate the effects of LED transmitters and photodetector receiver geometric configuration (orientation, irradiance angle, incidence angle, and positioning). Also, E_{A}^i, E_{AA}^i, E_{B}^i, E_{BB}^i, E_{C}^i, and E_{CC}^i in (5.16) denote the transmitted signals' energies impact. Then, the effective CRLB of the positioning error can be obtained based on (5.9) from (5.15) as in [33]

$$\mathrm{CRLB} \triangleq \mathrm{trace}\{\mathcal{I}_{\mathrm{sync}}^{-1}\}. \tag{5.17}$$

This expression provides the performance bounds on the 3D positioning accuracy limits evaluated for the synchronous VLP system under the effect of SDSN which was not studied in the literature.

Remark 1: As the CRLB in (5.17) is inverse of the FIM in (5.15). It can be observed

that ζ_n^2 term appears in the denominator and as $\zeta_n^2 \to \infty$, in this case, the second summation $\sum_{i=1}^{L_{\mathrm{T}}} \left(\frac{\partial \alpha_i}{\partial P_{\mathrm{r},v_1}} \frac{\partial \alpha_i}{\partial P_{\mathrm{r},v_2}} E_B^i + \alpha_i^2 \frac{\partial \tau_i}{\partial P_{\mathrm{r},v_1}} \frac{\partial \tau_i}{\partial P_{\mathrm{r},v_2}} E_A^i - \alpha_i \left(\frac{\partial \alpha_i}{\partial P_{\mathrm{r},v_1}} \frac{\partial \tau_i}{\partial P_{\mathrm{r},v_2}} + \frac{\partial \tau_i}{\partial P_{\mathrm{r},v_1}} \frac{\partial \alpha_i}{\partial P_{\mathrm{r},v_2}} \right) E_C^i \right) \to 0$. Consequently, $[\mathcal{I}_{\mathrm{sync}}]$ becomes very small which greatly increases the CRLB.

5.3.2 3D Positioning Estimation in Quasi-Synchronous System

In this section, we study a quasi-synchronous VLP system under SDSN effect where $\Delta_i = \Delta$ in (5.3) represents all the synchronized LED transmitters that have a timing bias with the photodetector receiver. Here, the TDOA parameter is considered instead of TOA to eliminate the unknown deterministic parameter Δ from $\tau_i = \frac{\|\boldsymbol{P}_{\mathrm{r}} - \boldsymbol{P}_{\mathrm{t}}^i\|}{c} + \Delta$. The TDOA parameter measurements are computed by $(\tau_i - \tau_j)$, where τ_i and τ_j represent the TOA measurements at photodetector receiver from ith and jth LED transmitters for $i, j \in \{1, \ldots, L_{\mathrm{T}}\}$ and $i \neq j$. Therefore, the scenario is termed as hybrid (TDOA/RSS).

From (5.2), (5.3), and (5.4) the vector containing the set of unknown parameters in (5.7) becomes $\boldsymbol{\varrho_1} = [\varrho, \Delta]^T$. Now, from (5.7) and (5.8), the FIM $\boldsymbol{\mathcal{I}}(\boldsymbol{\varrho_1})$ can be derived by utilizing (5.12)–(5.14) and (5.16) as

$$[\mathcal{I}(\boldsymbol{\varrho_1})] = \begin{bmatrix} \mathcal{I}_{\mathrm{A}} = \mathbb{E}\left\{ \frac{\partial \mathcal{L}(\boldsymbol{\varrho_1})}{\partial \varrho} \frac{\partial \mathcal{L}(\boldsymbol{\varrho_1})}{\partial \varrho} \right\} & \mathcal{I}_{\mathrm{b}} = \mathbb{E}\left\{ \frac{\partial \mathcal{L}(\boldsymbol{\varrho_1})}{\partial \varrho} \frac{\partial \mathcal{L}(\boldsymbol{\varrho_1})}{\partial \Delta} \right\} \\ \mathcal{I}_{\mathrm{b}}^T = \mathbb{E}\left\{ \frac{\partial \mathcal{L}(\boldsymbol{\varrho_1})}{\partial \Delta} \frac{\partial \mathcal{L}(\boldsymbol{\varrho_1})}{\partial \varrho} \right\} & \mathcal{I}_{\mathrm{d}} = \mathbb{E}\left\{ \frac{\partial \mathcal{L}(\boldsymbol{\varrho_1})}{\partial \Delta} \frac{\partial \mathcal{L}(\boldsymbol{\varrho_1})}{\partial \Delta} \right\} \end{bmatrix}, \tag{5.18}$$

where $[\mathcal{I}(\boldsymbol{\varrho_1})]$ is a 4×4 matrix with elements as follows:

$$\begin{aligned} [\mathcal{I}_{\mathrm{A}}]_{v_1,v_2} = \frac{R^2}{\sigma_n^2} \Bigg(\zeta_n^4 \, \sigma_n^2 \sum_{i=1}^{L_{\mathrm{T}}} \Bigg(& \frac{\partial \alpha_i}{\partial P_{\mathrm{r},v_1}} \frac{\partial \alpha_i}{\partial P_{\mathrm{r},v_2}} E_{BB}^i + \alpha_i^2 \frac{\partial \tau_i}{\partial P_{\mathrm{r},v_1}} \frac{\partial \tau_i}{\partial P_{\mathrm{r},v_2}} E_{AA}^i \\ & - \alpha_i \left(\frac{\partial \alpha_i}{\partial P_{\mathrm{r},v_1}} \frac{\partial \tau_i}{\partial P_{\mathrm{r},v_2}} + \frac{\partial \tau_i}{\partial P_{\mathrm{r},v_1}} \frac{\partial \alpha_i}{\partial P_{\mathrm{r},v_2}} \right) E_{CC}^i \Bigg) + \sum_{i=1}^{L_{\mathrm{T}}} \Bigg(\frac{\partial \alpha_i}{\partial P_{\mathrm{r},v_1}} \frac{\partial \alpha_i}{\partial P_{\mathrm{r},v_2}} E_B^i + \alpha_i^2 \frac{\partial \tau_i}{\partial P_{\mathrm{r},v_1}} \frac{\partial \tau_i}{\partial P_{\mathrm{r},v_2}} E_A^i \\ & - \alpha_i \left(\frac{\partial \alpha_i}{\partial P_{\mathrm{r},v_1}} \frac{\partial \tau_i}{\partial P_{\mathrm{r},v_2}} + \frac{\partial \tau_i}{\partial P_{\mathrm{r},v_1}} \frac{\partial \alpha_i}{\partial P_{\mathrm{r},v_2}} \right) E_C^i \Bigg) \Bigg), \end{aligned} \tag{5.19a}$$

where $[\mathcal{I}_{\rm A}]$ is a 3×3 matrix. Next, $[\mathcal{I}_{\rm b}]$ is a 3×1 vector with

$$[\mathcal{I}_{\rm b}]_{v_{(1|2)},\Delta} = \frac{R^2}{\sigma_n^2}\Bigg(\zeta_n^4\,\sigma_n^2\sum_{i=1}^{L_{\rm T}}\left(\alpha_i^2\frac{\partial\tau_i}{\partial P_{{\rm r},v_{(1|2)}}}E_{AA}^i-\alpha_i\frac{\partial\alpha_i}{\partial P_{{\rm r},v_{(1|2)}}}E_{CC}^i\right) + \sum_{i=1}^{L_{\rm T}}\left(\alpha_i^2\frac{\partial\tau_i}{\partial P_{{\rm r},v_{(1|2)}}}E_{A}^i-\alpha_i\frac{\partial\alpha_i}{\partial P_{{\rm r},v_{(1|2)}}}E_{C}^i\right)\Bigg), \tag{5.19b}$$

and $[\mathcal{I}_{\rm d}]_{\Delta,\Delta}$ is a scalar value,

$$[\mathcal{I}_{\rm c}]_{\Delta,\Delta} = \frac{R^2}{\sigma_n^2}\Bigg(\zeta_n^4\,\sigma_n^2\sum_{i=1}^{L_{\rm T}}\left(\alpha_i^2\,E_{AA}^i\right)+\sum_{i=1}^{L_{\rm T}}\left(\alpha_i^2\,E_{A}^i\right)\Bigg). \tag{5.19c}$$

Now, in the presence of the nuisance parameter Δ, the FIM $\mathcal{I}_{\rm qsyn}$ about parameters of interest $\boldsymbol{P}_{\rm r}$ can be calculated from (5.18) based on (5.19) as in [131]

$$\mathcal{I}_{\rm qsyn} = \Bigg(\boldsymbol{\mathcal{I}}_A-\boldsymbol{\mathcal{I}}_b\boldsymbol{\mathcal{I}}_d^{-1}\boldsymbol{\mathcal{I}}_b^T\Bigg). \tag{5.20}$$

Hence, after some mathematical manipulation $\mathcal{I}_{\rm qsyn}$ elements can be given as

$$[\mathcal{I}_{\rm qsyn}] = [\mathcal{I}_{\rm sync}] - \frac{1}{\left(\zeta_n^4\sigma_n^2\sum_{i=1}^{L_{\rm T}}(\alpha_i^2E_{AA}^i)+\sum_{i=1}^{L_{\rm T}}(\alpha_i^2E_{A}^i)\right)}kk^T, \tag{5.21}$$

where $[\mathcal{I}_{\rm sync}]$ is given as (5.15), $k=[k_x\ k_y\ k_z]^T$, and

$$k_{v_{(1|2)}} = \Bigg(R\,\zeta_n^2\sum_{i=1}^{L_{\rm T}}\left(\alpha_i^2\frac{\partial\tau_i}{\partial P_{{\rm r},v_{(1|2)}}}E_{AA}^i-\alpha_i\frac{\partial\alpha_i}{\partial P_{{\rm r},v_{(1|2)}}}E_{CC}^i\right) + \frac{R}{\sigma_n}\sum_{i=1}^{L_{\rm T}}\left(\alpha_i^2\frac{\partial\tau_i}{\partial P_{{\rm r},v_{(1|2)}}}E_{A}^i-\alpha_i\frac{\partial\alpha_i}{\partial P_{{\rm r},v_{(1|2)}}}E_{C}^i\right)\Bigg),$$

Consequently, the effective CRLB is derived based on (5.9) from (5.21) after excluding the nuisance parameter Δ as

$$\text{CRLB} \triangleq \text{trace}\big\{\mathcal{I}_{\rm qsyn}^{-1}\big\}. \tag{5.22}$$

Remark 2: It is key to note that the CRLB in (5.22) is larger or equal to that in (5.17) due to estimation of the additional parameter. This can be explained by noting that $[\mathcal{I}_{\mathrm{A}}] = [\mathcal{I}_{\mathrm{sync}}]$, consequently we can write

$$[\mathcal{I}_{\mathrm{sync}}] - [\mathcal{I}_{\mathrm{qsyn}}] \geq Z, \tag{5.23}$$

where $Z = \boldsymbol{\mathcal{I}}_b \boldsymbol{\mathcal{I}}_d^{-1} \boldsymbol{\mathcal{I}}_b^T$. Here Z is positive semidefinite matrix because $\boldsymbol{\mathcal{I}}_b \boldsymbol{\mathcal{I}}_b^T$ and $\boldsymbol{\mathcal{I}}_d^{-1}$ are always positive. This means that the quasi-synchronous scenario is always worse than the synchronous scenario and it approaches the synchronous scenario performance if $\Delta = 0$ or if the terms E_{A}^i, E_{AA}^i, E_{C}^i, and E_{CC}^i are zero.

5.3.3 3D Positioning Estimation in Asynchronous System

This section studies the positioning error performance in asynchronous VLC system under the effect of SDSN. In asynchronous system, there exists a timing bias Δ_i between the photodetector receiver and the LED transmitters clocks, where Δ_i is considered to be an unknown deterministic parameter for all $i \in \{1, \ldots, L_{\mathrm{T}}\}$. Therefore, the relationship as in (5.3) is unknown, meaning that the relationship between α_i and P_{r} as in (5.2) needs to be exploited in order to estimate the position. The scenario is termed as RSS based position estimation as α_i is related to RSS.

From (5.2), (5.3), and (5.4) the vector containing the set of unknown parameters in (5.7) becomes $\boldsymbol{\varrho_2} = [\varrho, \tau]^T$, where $\tau = [\tau_1 \ldots \tau_{L_{\mathrm{T}}}]$. Then, the FIM $\boldsymbol{\mathcal{I}}(\boldsymbol{\varrho_2})$ can be derived from (5.7), and (5.8) utilizing (5.12)–(5.14) and (5.16) as

$$[\mathcal{I}(\boldsymbol{\varrho_2})] = \begin{bmatrix} \mathcal{I}_{\mathrm{A}} = \mathbb{E}\left\{ \frac{\partial \mathcal{L}(\boldsymbol{\varrho_2})}{\partial \varrho} \frac{\partial \mathcal{L}(\boldsymbol{\varrho_2})}{\partial \varrho} \right\} & \mathcal{I}_{\mathrm{B}} = \mathbb{E}\left\{ \frac{\partial \mathcal{L}(\boldsymbol{\varrho_2})}{\partial \varrho} \frac{\partial \mathcal{L}(\boldsymbol{\varrho_2})}{\partial \tau} \right\} \\ \\ \mathcal{I}_{\mathrm{B}}^T = \mathbb{E}\left\{ \frac{\partial \mathcal{L}(\boldsymbol{\varrho_2})}{\partial \tau} \frac{\partial \mathcal{L}(\boldsymbol{\varrho_2})}{\partial \varrho} \right\} & \mathcal{I}_{\mathrm{D}} = \mathbb{E}\left\{ \frac{\partial \mathcal{L}(\boldsymbol{\varrho_2})}{\partial \tau} \frac{\partial \mathcal{L}(\boldsymbol{\varrho_2})}{\partial \tau} \right\} \end{bmatrix}, \tag{5.24}$$

where $[\mathcal{I}(\boldsymbol{\varrho_2})]$ is a size $\boldsymbol{\varrho_2} \times \boldsymbol{\varrho_2}$ matrix with entries as follows:

$$[\mathcal{I}_{\mathrm{A}}]_{v_1,v_2} = \frac{R^2}{\sigma_n^2}\left(\zeta_n^4\,\sigma_n^2 \sum_{i=1}^{L_{\mathrm{T}}}\left(\frac{\partial \alpha_i}{\partial P_{\mathrm{r},v_1}}\frac{\partial \alpha_i}{\partial P_{\mathrm{r},v_2}}E^i_{BB}\right) + \sum_{i=1}^{L_{\mathrm{T}}}\left(\frac{\partial \alpha_i}{\partial P_{\mathrm{r},v_1}}\frac{\partial \alpha_i}{\partial P_{\mathrm{r},v_2}}E^i_{B}\right)\right), \tag{5.25a}$$

where $[\mathcal{I}_{\mathrm{A}}]$ is a 3×3 matrix. Next, $[\mathcal{I}_{\mathrm{B}}]$ is a $3 \times L_{\mathrm{T}}$ matrix, for $i, j \in \{1, \ldots, L_{\mathrm{T}}\}$ with

$$[\mathcal{I}_{\mathrm{B}}]_{v_{(1|2)},\tau_i} = -\,\frac{R^2}{\sigma_n^2}\,\alpha_i\,\frac{\partial \alpha_i}{\partial P_{\mathrm{r},v_{(1|2)}}}\left(\zeta_n^4\,\sigma_n^2\,E^i_{CC} + E^i_{C}\right), \tag{5.25b}$$

and then, $[\mathcal{I}_{\mathrm{D}}]_{\tau_i,\tau_j}$ is a $L_{\mathrm{T}} \times L_{\mathrm{T}}$ matrix with

$$[\mathcal{I}_{\mathrm{D}}]_{\tau_i,\tau_j} = \begin{cases} \dfrac{R^2}{\sigma_n^2}\,\alpha_i^2\left(\zeta_n^4\,\sigma_n^2\,E^i_{AA} + E^i_{A}\right), & \text{if } i = j \\ 0. & \text{if } i \neq j \end{cases} \tag{5.25c}$$

Now, in the presence of the nuisance parameter τ_i for $i \in \{1, \ldots, L_{\mathrm{T}}\}$, the FIM $\mathcal{I}_{\mathrm{asyn}}$ about parameters of interest $\boldsymbol{P}_{\mathrm{r}}$ can be calculated based on (5.24) from (5.25) as

$$\mathcal{I}_{\mathrm{asyn}} = \left(\boldsymbol{\mathcal{I}}_A - \boldsymbol{\mathcal{I}}_B\boldsymbol{\mathcal{I}}_D^{-1}\boldsymbol{\mathcal{I}}_B^T\right). \tag{5.26}$$

Hence, after some mathematical manipulation $\mathcal{I}_{\mathrm{asyn}}$ elements can be given as

$$\begin{aligned}[\mathcal{I}_{\mathrm{asyn}}]_{v_1,v_2} =& \frac{R^2}{\sigma_n^2}\left(\zeta_n^4\,\sigma_n^2\sum_{i=1}^{L_{\mathrm{T}}}\left(\frac{\partial \alpha_i}{\partial P_{\mathrm{r},v_1}}\frac{\partial \alpha_i}{\partial P_{\mathrm{r},v_2}}\left(\frac{E^i_{AA}\,E^i_{BB} - \left(E^i_{CC}\right)^2}{E^i_{AA}}\right)\right)\right. \\ &\left. + \sum_{i=1}^{L_{\mathrm{T}}}\left(\frac{\partial \alpha_i}{\partial P_{\mathrm{r},v_1}}\frac{\partial \alpha_i}{\partial P_{\mathrm{r},v_2}}\left(\frac{E^i_{A}\,E^i_{B} - \left(E^i_{C}\right)^2}{E^i_{A}}\right)\right)\right).\end{aligned} \tag{5.27}$$

Consequently, the effective CRLB is derived from (5.9) and (5.27) after excluding the nuisance parameter τ_i as

$$\mathrm{CRLB} \triangleq \mathrm{trace}\{\mathcal{I}_{\mathrm{asyn}}^{-1}\}. \tag{5.28}$$

Remark 3: Now, when $\zeta_n^2 = 0$ suggesting no SDSN then all the terms in (5.17), (5.22), and (5.28) match perfectly with those in [28] and [40], therefore validating the presented analysis.

5.4 Discussion and Evaluation Results

In this section, the theoretical limits of the positioning estimation error performance are investigated with the help of simulation. We consider an area of $8 \times 8 \times 5$ m^3 with a perpendicular distance of 4 m between the LED transmitters and the photodetector receiver. There are $L_{\mathrm{T}} = 4$ LED transmitters placed at $P_{\mathrm{t}}^1 = [2\ 2\ 5]^T$, $P_{\mathrm{t}}^2 = [6\ 2\ 5]^T$, $P_{\mathrm{t}}^3 = [2\ 6\ 5^T]$, and $P_{\mathrm{t}}^4 = [6\ 6\ 5]^T$, respectively. The photodetector receiver is placed at $P_{\mathrm{r}} = [4\ 4\ 1]^T$. The LED transmitters orientation vectors are given as $\boldsymbol{n}_{\mathrm{t}}^i = [n_{\mathrm{t,x}}^i\ \ n_{\mathrm{t,y}}^i\ \ n_{\mathrm{t,z}}^i]^T$, where $n_{\mathrm{t,x}}^i = \sin\theta_i \cos\phi_i$, $n_{\mathrm{t,y}}^i = \sin\theta_i \sin\phi_i$, and $n_{\mathrm{t,z}}^i = \cos\theta_i$, for $i \in \{1, \ldots, L_{\mathrm{T}}\}$, ϕ_i is the irradiance angle that photodetector receiver makes with a particular LED transmitter's orientation vector, and θ_i is the incidence angle with respect to orientation vector of the receiver as shown in Fig. 5.1. The LED transmitters orientation angles are taken as $(\theta_1, \phi_1) = (150°, 45°)$, $(\theta_2, \phi_2) = (150°, 135°)$, $(\theta_3, \phi_3) = (150°, -45°)$, and $(\theta_4, \phi_4) = (150°, -135°)$. The photodetector receiver orientation $\boldsymbol{n}_{\mathrm{r}} = [n_{\mathrm{r,x}}\ \ n_{\mathrm{r,y}}\ \ n_{\mathrm{r,z}}]^T$ is chosen as $\boldsymbol{n}_{\mathrm{r}} = [0\ 0\ 1]^T$.

The LED transmitters Lambertian order is $m_i = 1$ for $i \in \{1, \ldots, L_{\mathrm{T}}\}$, the VLC photodetector responsivity is assumed as $R = 1$ amps/watt with the effective area of photodetector W is 3×3 cm^2. The noise variance is $\sigma_n^2 = 10^{-10}$, and the SDSN $\zeta_n^2 > 0$, as these are practical values [47]. The LED's transmitted signal $x_i(t)$ for $i \in \{1, \ldots, L_{\mathrm{T}}\}$ in (5.4) is modeled as

$$x_i(t) = A\left(1 - \cos\left(2\,\pi\, t/T_{\mathrm{o},i}\right)\right)\left(1 + \cos\left(2\,\pi\, f_c\, t\right)\right), \tag{5.29}$$

where $t \in [0, T_{\mathrm{o},i}]$ for $i \in \{1, \ldots, L_{\mathrm{T}}\}$, A denotes the source optical power (i.e., average

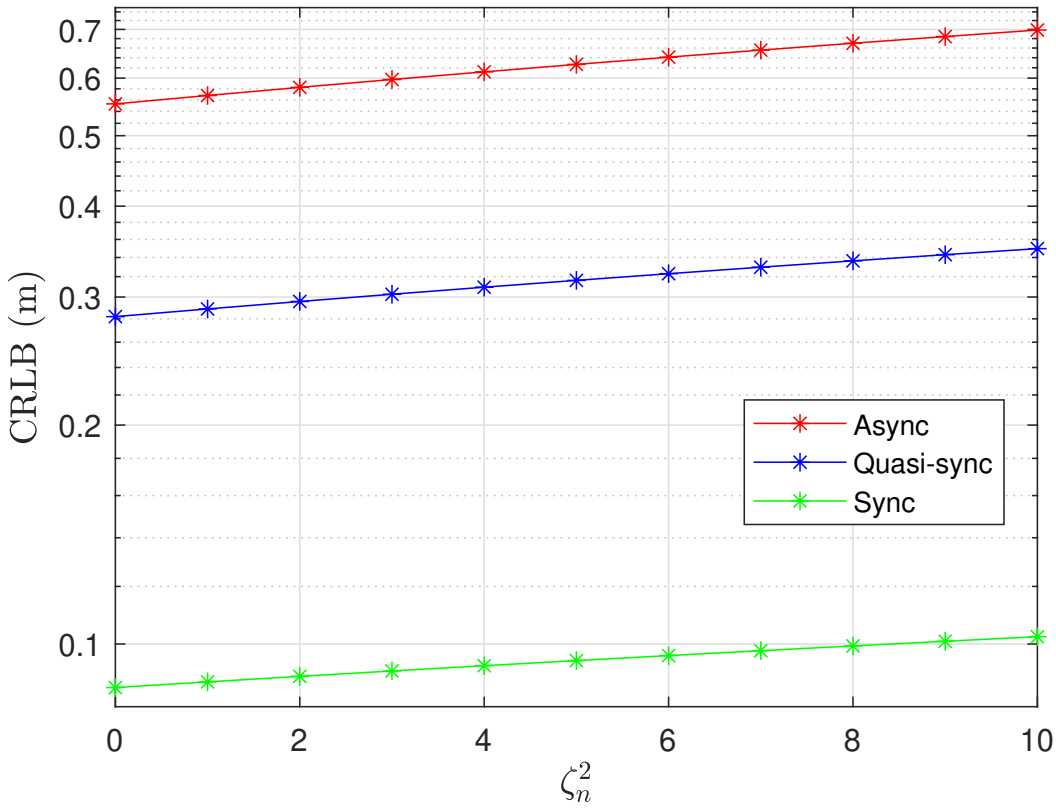

Figure 5.2: CRLB versus ζ_n^2 for synchronous, quasi-synchronous, and asynchronous scenarios.

emitted optical power) and f_c represents the carrier frequency of the signal, respectively. Furthermore, the source optical power is directly proportional to the LED Lumens at the transmitter. Therefore, the power constraints apply directly to the LED input and not to the square of its magnitude (as is usually the case for electrical transmission models) [47].

The LED transmitters use signal in (5.29) for positioning estimation, which is a dc-biased windowed sinusoid, where $A = 30$ dB is applied with a signal duration of $T_{o,i} = 10^{-5}$ s and a carrier frequency of $f_c = 100$ MHz. The aforementioned parameters stay the same unless otherwise stated. All transmitted signal energies in (5.16) are calculated numerically.

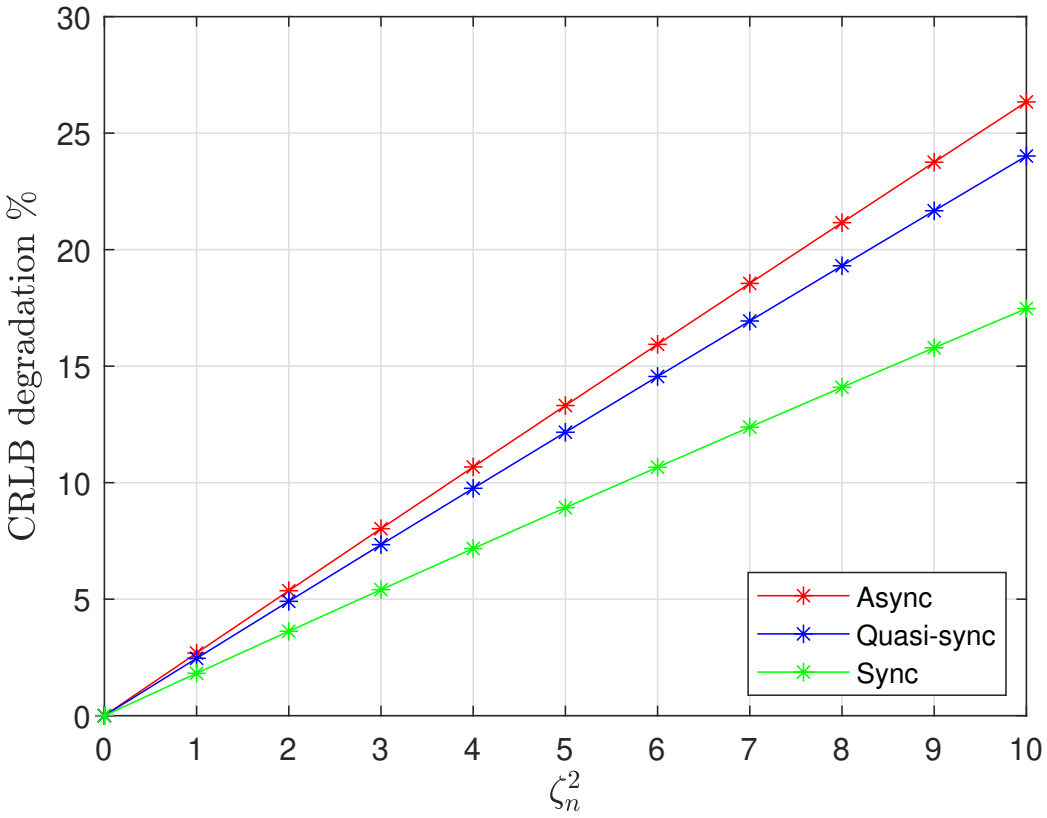

Figure 5.3: CRLB degradation % versus ζ_n^2 for synchronous, quasi-synchronous, and asynchronous scenarios.

Fig. 5.2 studies the effect of ζ_n^2 on the CRLBs for synchronous, quasi-synchronous, and asynchronous scenarios. The CRLB for each scenario has the lowest value when $\zeta_n^2 = 0$ (i.e., no SDSN). However, as ζ_n^2 increases, SDSN impacts the estimation bounds in all the cases, which is evident from the figure. For instance, error bounds at $\zeta^2 = 0$ and $\zeta^2 = 10$ for synchronous scenario is about 8.7 cm and 10.2 cm, for quasi-synchronous scenario is about 28.2 cm and 35 cm, and for asynchronous scenario is about 55.3 cm and 70 cm. respectively.

Fig. 5.3 illustrates the error bounds degradation due to the presence of SDSN ζ_n^2 for

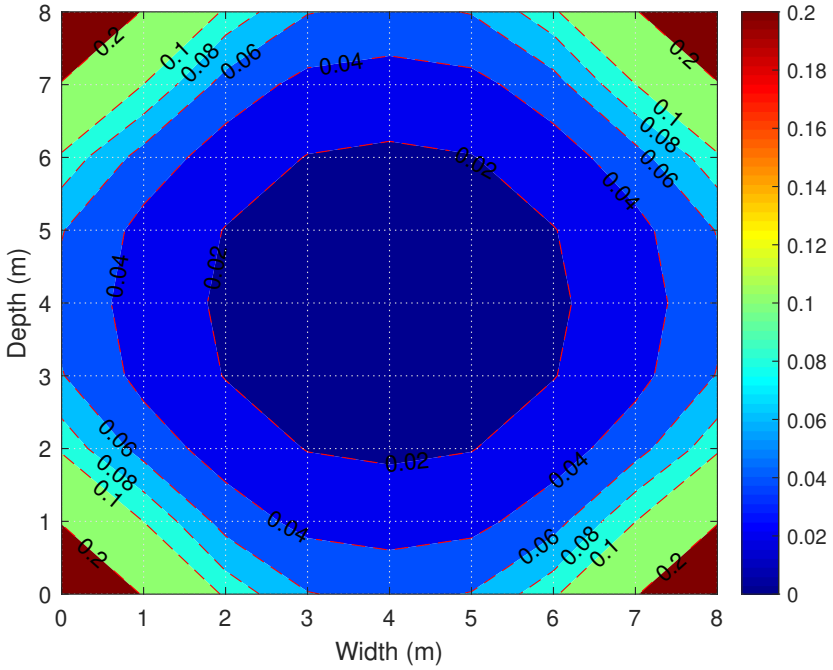

(a) Synchronous Scenario CRLB with $\zeta_n^2 = 0$.

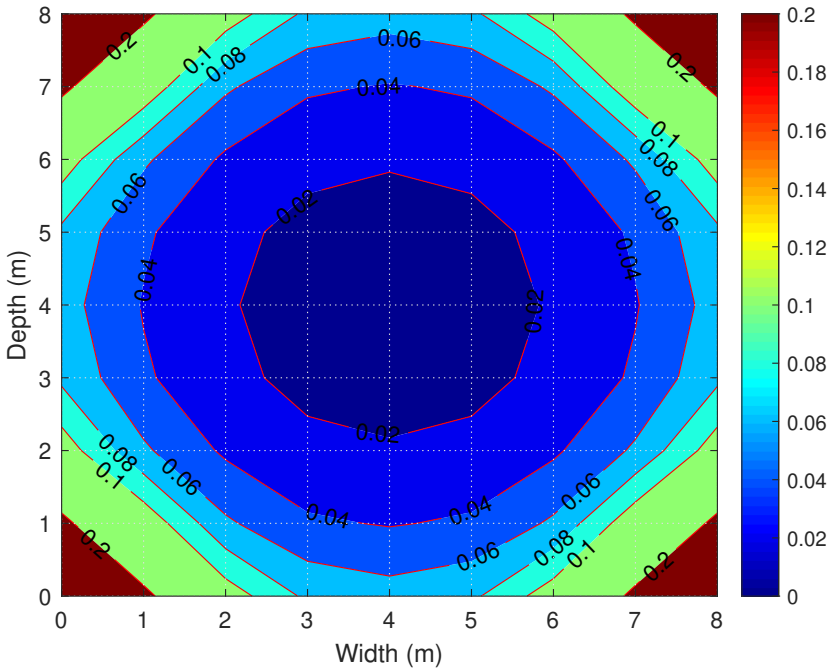

(b) Synchronous Scenario CRLB with $\zeta_n^2 = 20$.

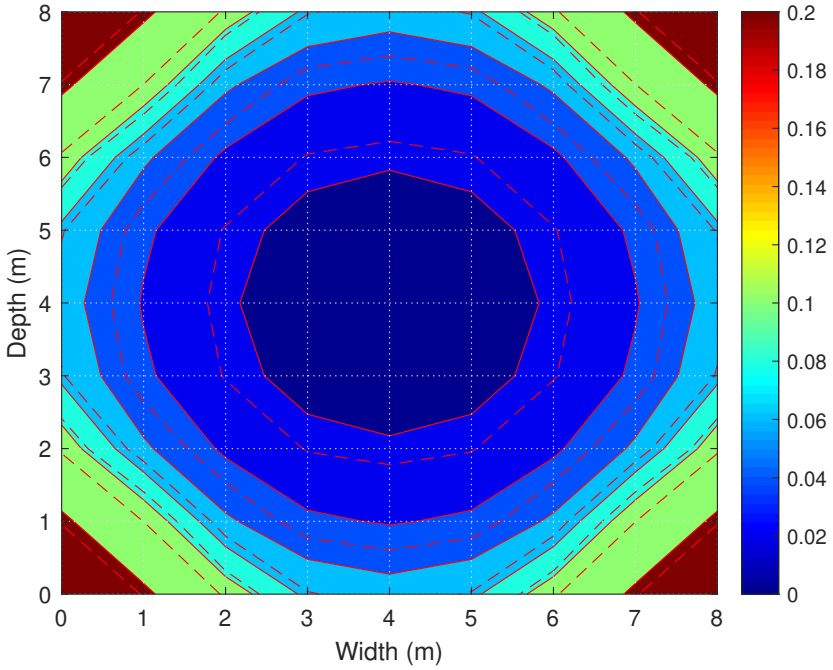

(c) Synchronous Scenario CRLB with $\zeta_n^2 = 0$ and $\zeta_n^2 = 20$.

Figure 5.4: CRLB as the photodetector receiver moves inside the space for synchronous scenario, where $T_{\mathrm{o},i} = 10^{-4}$s.

all considered scenarios. We calculate the CRLB degradation as

$$\mathrm{CRLB}_{\mathrm{deg}} = \left(\frac{\mathrm{CRLB}_{\zeta_n^2 > 0}}{\mathrm{CRLB}_{\zeta_n^2 = 0}} - 1 \right) \times 100\%. \tag{5.30}$$

The CRLBs are obtained using (5.17), (5.22), and (5.28) for synchronous, quasi-synchronous, and asynchronous scenarios, respectively. The asynchronous scenario shows the worst performance with a degradation level of 26.3% when $\zeta_n^2 = 10$, then the quasi-synchronous scenario with a degradation level of 24.01% and synchronous scenario is the least degraded with a degradation level of 17.47%. This behaviour can be explained as asynchronous position estimation relies only on α_i parameter, which is related to RSS. So as RSS increases, the SDSN has a significant impact on error bounds for an asynchronous scenario compared to synchronous and quasi-synchronous position estimations, as these scenarios use both α_i and τ_i parameters.

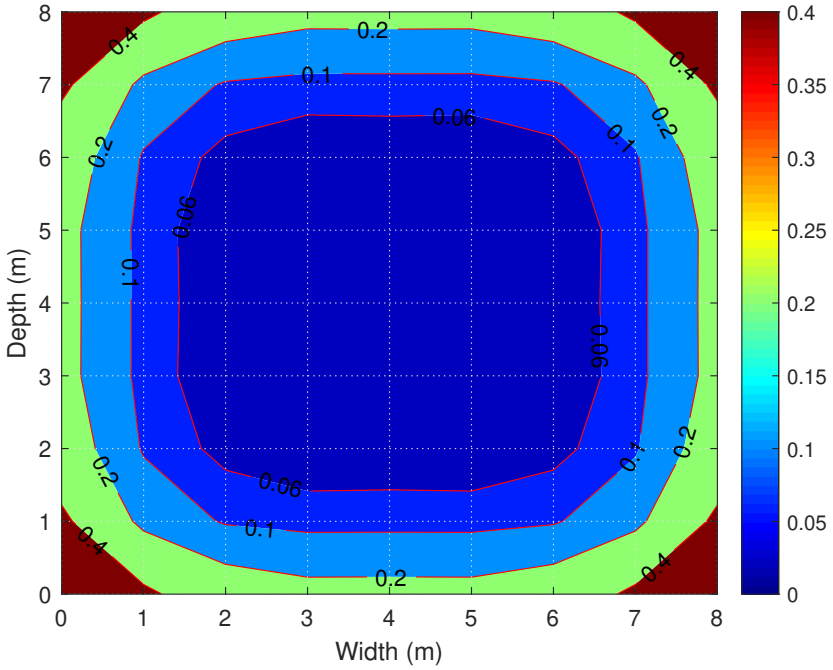

(a) Quasi-synchronous Scenario CRLB with $\zeta_n^2 = 0$.

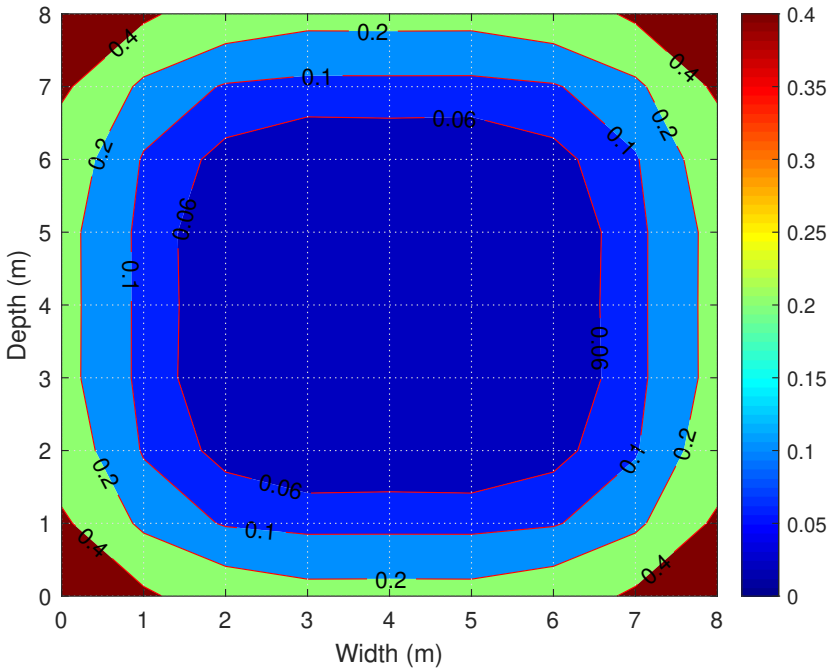

(b) Quasi-synchronous Scenario CRLB with $\zeta_n^2 = 20$.

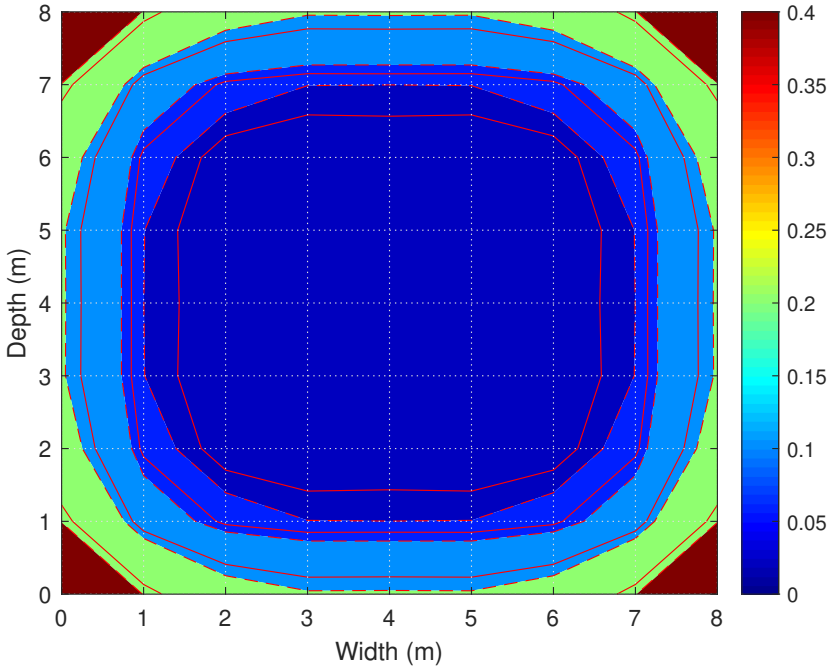

(c) Quasi-synchronous Scenario CRLB with $\zeta_n^2 = 0$ and $\zeta_n^2 = 20$.

Figure 5.5: CRLB as the photodetector receiver moves inside the space for quasi-synchronous scenario, where $T_{\mathrm{o},i} = 10^{-4}$s.

Fig. 5.4 shows the contour plots to study the effect of ζ_n^2 on the error bounds for synchronous scenario, as the photodetector receiver moves along x–y plane inside the area from $\boldsymbol{P}_{\mathrm{r}} = [0\ 0\ 1]^T$ edge to $\boldsymbol{P}_{\mathrm{r}} = [8\ 8\ 1]^T$ edge positions. Fig. 5.4a shows the CRLB when $\zeta_n^2 = 0$ (i.e., no SDSN) and Fig. 5.4b shows the CRLB when $\zeta_n^2 = 20$. The result here agrees with the ones in the previous figures where ζ_n^2 has a negative impact of the error bounds as the contour area for each error bound is smaller when the SDSN exists. In addition, as the figure shows, when the photodetector receiver is placed at the edges, SDSN has less impact on the error bounds. This is due to the fact that the signal strength reduces when moving away from the LED transmitters. This confirms that the impact of SDSN depends on the RSS. Similarly, quasi-synchronous and asynchronous scenarios have similar trend as Fig. 5.5 and Fig. 5.6 illustrate.

Finally, in Fig. 5.7, the CRLBs for synchronous, quasi-synchronous, and asyn-

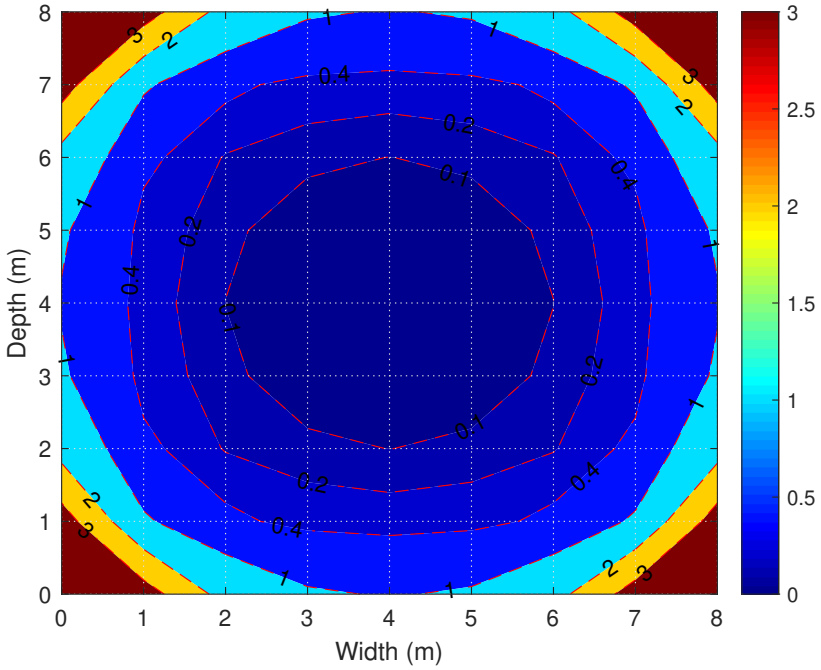

(a) Asynchronous Scenario CRLB with $\zeta_n^2 = 0$.

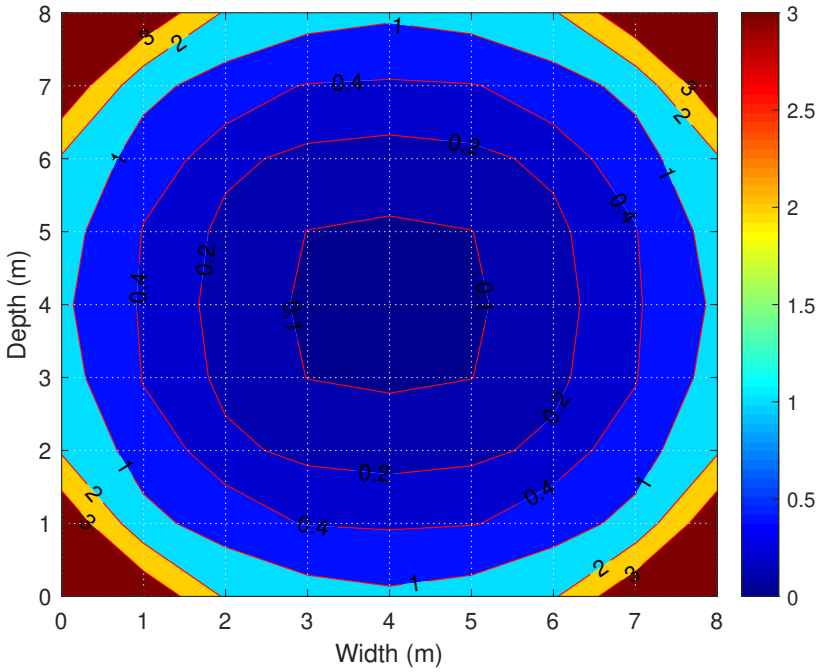

(b) Asynchronous Scenario CRLB with $\zeta_n^2 = 20$.

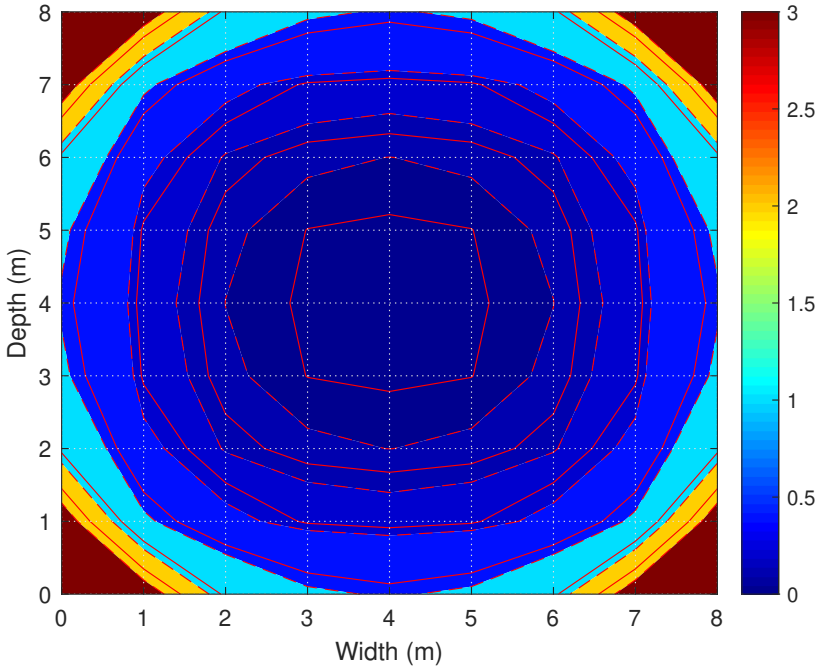

(c) Asynchronous Scenario CRLB with $\zeta_n^2 = 0$ and $\zeta_n^2 = 20$.

Figure 5.6: CRLB as the photodetector receiver moves inside the space for asynchronous scenario, where $T_{\mathrm{o},i} = 10^{-4}$s.

chronous scenarios are plotted versus the source optical power A for different values of ζ_n^2. As anticipated, higher source optical power improves the CRLBs for all the considered scenarios. Moreover, the synchronous scenario still demonstrates the best performance for all the studied energy and ζ_n^2 values. However, as can be seen, the presence of SDSN minimizes the effect of increasing optical power at the source. For example, in the quasi-synchronous scenario, a 1.0 dB power loss between $\zeta_n^2 = 0$ and $\zeta_n^2 = 10$ is noticed when the CRLB $= 10^{-1}$. This loss increases to more than 2.0 dB when the CRLB $= 10^{-2}$. The same trend is observed in synchronous and asynchronous scenarios.

However, an intriguing result can be seen due to the impact of SDSN. There is a point where the performance of the quasi-synchronous scenario at $\zeta_n^2 = 10$, is eclipsed by that of the asynchronous scenario at $\zeta_n^2 = 0$. This can be observed in the subplot where

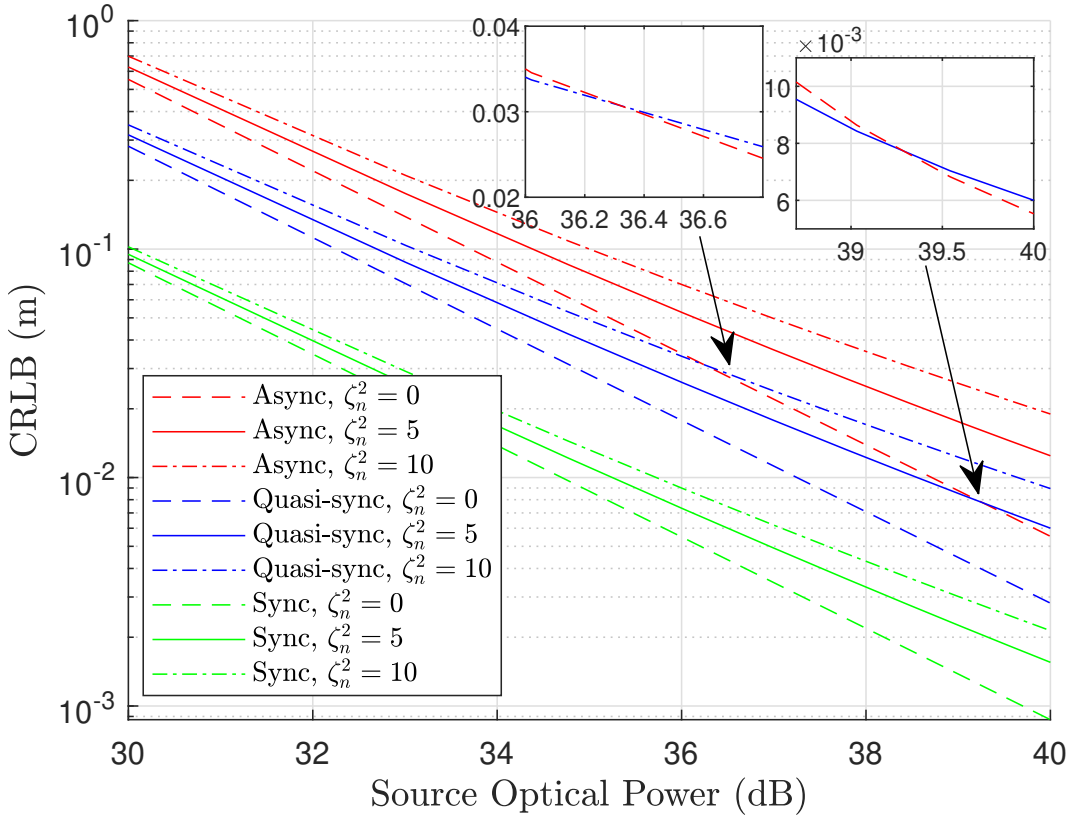

Figure 5.7: CRLB versus source optical power for synchronous, quasi-synchronous, and asynchronous scenarios.

the blue and red lines intersect (i.e., the quasi-synchronous scenario demonstrates better performance before a source optical power of 36.4 dB, and poor performance afterward). The same behaviour can be observed between the quasi-synchronous at $\zeta_n^2 = 5$ and the asynchronous scenario at $\zeta_n^2 = 0$. In this case, the point of intersection shifts to the right and becomes 39.2 dB.

5.5 Conclusion

This chapter presents the theoretical CRLBs for a 3D VLP system under the effect of SDSN. We consider different synchronous, quasi-synchronous, and asynchronous scenar-

ios, specifically the three cases of Hybrid (TOA/RSS), Hybrid (TDOA/RSS), and RSS based position estimations. To this end, we consider the available information from the time of arrival parameter and channel attenuation factor as a function of the photodetector receiver's positioning. It was shown that the SDSN has a severe impact on the estimation bounds in all studied scenarios. Furthermore, it was observed that the degradation level is higher for the asynchronous scenario when the position estimation is based only on channel attenuation factor, which is related to RSS, and is impacted more by SDSN presence. In comparison, when the position estimation considers both channel attenuation factor and time of arrival or time difference of arrival parameters VLP systems are impacted less. In the future work, estimators that can correspond to the CRLB's performance in a system under the effects of SDSN will be considered. In addition, any technique that helps to remove the timing bias in asynchronous and quasi-synchronous scenarios might also help improve the system performance.

Chapter 6

Conclusions and Future Work

6.1 Conclusions

This thesis investigates theoretical CRLBs of a VLP system under the effect of SDSN. We consider different scenarios, specifically the three cases of TOA, RSS and hybrid (TOA-RSS) based distance estimations. To this end, we consider the relationships between the distance, channel attenuation factor, and time delay parameters. It was shown that the SDSN has a severe impact on the estimation bounds in all cases. In addition, the degradation level is higher for scenarios that depend on RSS compared to when the estimation only considers the TOA.

This thesis also addresses the synchronization problem in VLC systems. First, we purposed a bi-directional synchronization protocol that can eliminate time biasing between the transmitter and receiver. Second, we consider the effect of SDSN on distance estimation bounds in bi-directional VLC systems. The results indicate that SDSN significantly impacts the CRLBs for both the synchronous and asynchronous protocols. However, the bi-directional protocol shows impressive performance compared to that of the directional protocol tested.

Lastly, the theoretical CRLBs for a 3D VLP system under the joint effects of SDSN

and thermal noise are presented. We consider synchronous, quasi-synchronous, and asynchronous scenarios, specifically the three cases of Hybrid (TOA-RSS), Hybrid (TDOA-RSS), and RSS based position estimations. Here, we consider the available information from the TOA parameter and channel attenuation factor as functions of the photodetector receiver's positioning. It was shown that the SDSN has a severe impact on the estimation bounds in all studied scenarios. Furthermore, it was observed that the degradation level is higher for the asynchronous scenario when the position estimation is based only on channel attenuation factor, which is related to RSS, and is impacted more by SDSN presence. In comparison to when the position estimation considers both channel attenuation factor and TOA or TDOA parameters which impact VLP systems less.

6.2 Future Work

There are still several issues related to SDSN and synchronization for the discussed VLP systems, and the proposed solutions in this work constitute a favorable platform for several future extensions. The estimators that can correspond to the CRLB's performance in VLP systems under the effects of SDSN should be considered. In addition, any technique that helps to remove the timing bias in asynchronous and quasi-synchronous scenarios for 3D positioning might help to improve the system performance further.

The thesis only considered white color LEDs, another possible direction is a multi-color (RGB LEDs based VLP system in the presence of SDSN. In addition, tri-color LED transmitters having having arbitrary orientations for directional and bi-directional VLC systems can be considered.

Bibliography

[1] ITU-T, "Recommendation ITU-T Y.4000/Y.2060, Overview of the Internet of Things," The ITU Telecommunication Standardization Sector, Tech. Rep., June 2012.

[2] K. Rose, S. Eldridge, and L. Chapin, "The internet of things: An overview," *The internet society (ISOC)*, vol. 80, pp. 1–50, 2015.

[3] W. Saad, M. Bennis, and M. Chen, "A vision of 6G wireless systems: Applications, trends, technologies, and open research problems," *IEEE network*, vol. 34, no. 3, pp. 134–142, 2019.

[4] K. David and H. Berndt, "6G vision and requirements: Is there any need for beyond 5G?" *IEEE vehicular technology magazine*, vol. 13, no. 3, pp. 72–80, 2018.

[5] F. Tariq, M. R. Khandaker, K.-K. Wong, M. A. Imran, M. Bennis, and M. Debbah, "A speculative study on 6G," *IEEE Wireless Communications*, vol. 27, no. 4, pp. 118–125, 2020.

[6] M. Z. Chowdhury, M. Shahjalal, S. Ahmed, and Y. M. Jang, "6G wireless communication systems: Applications, requirements, technologies, challenges, and research directions," *IEEE Open Journal of the Communications Society*, vol. 1, pp. 957–975, 2020.

[7] L. Bariah, L. Mohjazi, S. Muhaidat, P. C. Sofotasios, G. K. Kurt, H. Yanikomeroglu, and O. A. Dobre, "A prospective look: Key enabling technologies, applications and open research topics in 6G networks," *IEEE Access*, vol. 8, pp. 174 792–174 820, 2020.

[8] T. Huang, W. Yang, J. Wu, J. Ma, X. Zhang, and D. Zhang, "A survey on green 6G network: Architecture and technologies," *IEEE Access*, vol. 7, pp. 175 758–175 768, 2019.

[9] S. Arai, M. Kinoshita, and T. Yamazato, "Optical wireless communication: A candidate 6g technology?" *IEICE Transactions on Fundamentals of Electronics, Communications and Computer Sciences*, vol. 104, no. 1, pp. 227–234, 2021.

[10] N. Chi, Y. Zhou, Y. Wei, and F. Hu, "Visible light communication in 6G: Advances, challenges, and prospects," *IEEE Vehicular Technology Magazine*, vol. 15, no. 4, pp. 93–102, 2020.

[11] Spectrum Management Series, "Visible light for broadband communications," The International Telecommunication Union-Radiocommunication Sector, Tech. Rep., June 2019.

[12] A. S. Hamza, J. S. Deogun, and D. R. Alexander, "Classification framework for free space optical communication links and systems," *IEEE Communications Surveys & Tutorials*, vol. 21, no. 2, pp. 1346–1382, 2018.

[13] IEEE, "IEEE Draft Standard for Local and metropolitan area networks - Part 15.7: Short-Range Optical Wireless Communications," *IEEE P802.15.7/D3, August 2018*, pp. 1–412, 2018.

[14] G. Dreyfus and C. Gallinat, "Rise and shine: lighting the world with 10 billion LED bulbs," *US Department of Energy*, vol. 7, 2015.

[15] A. Jovicic, J. Li, and T. Richardson, "Visible light communication: opportunities, challenges and the path to market," *IEEE Communications Magazine*, vol. 51, no. 12, pp. 26–32, 2013.

[16] L. U. Khan, "Visible light communication: Applications, architecture, standardization and research challenges," *Digital Communications and Networks*, vol. 3, no. 2, pp. 78–88, 2017.

[17] L. E. M. Matheus, A. B. Vieira, L. F. Vieira, M. A. Vieira, and O. Gnawali, "Visible light communication: concepts, applications and challenges," *IEEE Communications Surveys & Tutorials*, vol. 21, no. 4, pp. 3204–3237, 2019.

[18] D. Karunatilaka, F. Zafar, V. Kalavally, and R. Parthiban, "LED based indoor visible light communications: State of the art," *IEEE Communications Surveys & Tutorials*, vol. 17, no. 3, pp. 1649–1678, 2015.

[19] E. Gerhátné Udvary, "Visible Light Communication Survey," *Infocommunications Journal*, vol. 11, no. 2, pp. 22–31, 2019.

[20] A. E. Ibhaze, P. E. Orukpe, and F. O. Edeko, "High Capacity Data Rate System: A Review of Visible Light Communication Technology," *Journal of Electronic Science and Technology*, p. 100055, 2020.

[21] A. Gomez, K. Shi, C. Quintana, M. Sato, G. Faulkner, B. C. Thomsen, and D. O'Brien, "Beyond 100-Gb/s indoor wide field-of-view optical wireless communications," *IEEE Photonics Technology Letters*, vol. 27, no. 4, pp. 367–370, 2014.

[22] S. Shao, A. Khreishah, M. B. Rahaim, H. Elgala, M. Ayyash, T. D. Little, and J. Wu, "An indoor hybrid WiFi-VLC internet access system," in *2014 IEEE 11th International Conference on Mobile Ad Hoc and Sensor Systems*. IEEE, 2014, pp. 569–574.

[23] T.-H. Do and M. Yoo, "An in-depth survey of visible light communication based positioning systems," *Sensors*, vol. 16, no. 5, p. 678, 2016.

[24] J. Luo, L. Fan, and H. Li, "Indoor positioning systems based on visible light communication: State of the art," *IEEE Communications Surveys & Tutorials*, vol. 19, no. 4, pp. 2871–2893, 2017.

[25] Y. Zhuang, L. Hua, L. Qi, J. Yang, P. Cao, Y. Cao, Y. Wu, J. Thompson, and H. Haas, "A survey of positioning systems using visible LED lights," *IEEE Communications Surveys & Tutorials*, vol. 20, no. 3, pp. 1963–1988, 2018.

[26] M. Afzalan and F. Jazizadeh, "Indoor positioning based on visible light communication: A performance-based survey of real-world prototypes," *ACM Computing Surveys (CSUR)*, vol. 52, no. 2, pp. 1–36, 2019.

[27] A. Rahman, T. Li, and Y. Wang, "Recent advances in indoor localization via visible lights: A survey," *Sensors*, vol. 20, no. 5, p. 1382, 2020.

[28] M. F. Keskin, A. D. Sezer, and S. Gezici, "Localization via visible light systems," *Proceedings of the IEEE*, vol. 106, no. 6, pp. 1063–1088, 2018.

[29] S. Y. Lee, H. S. Choi, and C. D. Lee, "Visible light communication apparatus for vehicle, system and method for vehicular communication inside tunnel using visible light communication," Mar. 25 2014, uS Patent 8,681,017.

[30] P. Chen, M. Pang, D. Che, Y. Yin, D. Hu, and S. Gao, "A Survey on Visible Light Positioning from Software Algorithms to Hardware," *Wireless Communications and Mobile Computing*, vol. 2021, 2021.

[31] C. Wang, L. Wang, X. Chi, S. Liu, W. Shi, and J. Deng, "The research of indoor positioning based on visible light communication," *China Communications*, vol. 12, no. 8, pp. 85–92, 2015.

[32] M. A. Dawood, S. S. Saleh, E.-S. A. El-Badawy, and M. H. Aly, "A comparative analysis of localization algorithms for visible light communication," *Optical and Quantum Electronics*, vol. 53, no. 2, pp. 1–25, 2021.

[33] S. M. Kay, *Fundamentals of statistical signal processing*. Prentice Hall PTR, 1993.

[34] T. Q. Wang, Y. A. Sekercioglu, A. Neild, and J. Armstrong, "Position accuracy of time-of-arrival based ranging using visible light with application in indoor localization systems," *Journal of Lightwave Technology*, vol. 31, no. 20, pp. 3302–3308, 2013.

[35] X. Zhang, J. Duan, Y. Fu, and A. Shi, "Theoretical accuracy analysis of indoor visible light communication positioning system based on received signal strength indicator," *Journal of Lightwave Technology*, vol. 32, no. 21, pp. 3578–3584, 2014.

[36] C. Amini, A. Taherpour, T. Khattab, and S. Gazor, "Theoretical accuracy analysis of indoor visible light communication positioning system based on time-of-arrival," in *2016 IEEE Canadian Conference on Electrical and Computer Engineering (CCECE)*, 2016, pp. 1–5.

[37] Z. Zheng, L. Liu, and W. Hu, "Accuracy of ranging based on DMT visible light communication for indoor positioning," *IEEE Photonics Technology Letters*, vol. 29, no. 8, pp. 679–682, 2017.

[38] H. Steendam, T. Q. Wang, and J. Armstrong, "Theoretical lower bound for indoor visible light positioning using received signal strength measurements and an aperture-based receiver," *Journal of Lightwave Technology*, vol. 35, no. 2, pp. 309–319, 2016.

[39] A. Naeem, N. U. Hassan, M. A. Pasha, C. Yuen, and A. Sikora, "Performance analysis of TDOA-based indoor positioning systems using visible LED lights," in *2018 IEEE 4th International Symposium on Wireless Systems within the International Conferences on Intelligent Data Acquisition and Advanced Computing Systems (IDAACS-SWS)*. IEEE, 2018, pp. 103–107.

[40] E. Kazikli and S. Gezici, "Hybrid TDOA/RSS based localization for visible light systems," *Digital Signal Processing*, vol. 86, pp. 19–28, 2019.

[41] H. Hosseinianfar and M. Brandt-Pearce, "Performance limits for fingerprinting-based indoor optical communication positioning systems exploiting multipath reflections," *IEEE Photonics Journal*, vol. 12, no. 4, pp. 1–16, 2020.

[42] X. Liu, D. Zou, N. Huang, and S. Zhang, "A Comprehensive Accuracy Analysis of Visible Light Positioning under Shot Noise," in *2020 IEEE/CIC International Conference on Communications in China (ICCC Workshops)*, 2020, pp. 167–172.

[43] B. Zhou, Y. Zhuang, and Y. Cao, "On the Performance Gain of Harnessing Non-Line-Of-Sight Propagation for Visible Light-Based Positioning," *IEEE Transactions on Wireless Communications*, vol. 19, no. 7, pp. 4863–4878, 2020.

[44] M. F. Keskin, S. Gezici, and O. Arikan, "Direct and two-step positioning in visible light systems," *IEEE Transactions on Communications*, vol. 66, no. 1, pp. 239–254, 2018.

[45] H. Manor and S. Arnon, "Performance of an optical wireless communication system as a function of wavelength," *Applied optics*, vol. 42, no. 21, pp. 4285–4294, 2003.

[46] J. M. Kahn and J. R. Barry, "Wireless infrared communications," *Proceedings of the IEEE*, vol. 85, no. 2, pp. 265–298, 1997.

[47] S. M. Moser, "Capacity results of an optical intensity channel with input-dependent Gaussian noise," *IEEE Transactions on Information Theory*, vol. 58, no. 1, pp. 207–223, 2012.

[48] L. Chettri and R. Bera, "A comprehensive survey on Internet of Things (IoT) toward 5G wireless systems," *IEEE Internet of Things Journal*, vol. 7, no. 1, pp. 16–32, 2019.

[49] H. Yang, W.-D. Zhong, C. Chen, and A. Alphones, "Integration of visible light communication and positioning within 5G networks for internet of things," *IEEE Network*, vol. 34, no. 5, pp. 134–140, 2020.

[50] M. K. Afzal, Y. B. Zikria, S. Mumtaz, A. Rayes, A. Al-Dulaimi, and M. Guizani, "Unlocking 5G spectrum potential for intelligent IoT: Opportunities, challenges, and solutions," *IEEE Communications Magazine*, vol. 56, no. 10, pp. 92–93, 2018.

[51] H. Haas, J. Elmirghani, and I. White, "Optical wireless communication," 2020.

[52] M. Giordani, M. Polese, M. Mezzavilla, S. Rangan, and M. Zorzi, "Toward 6G networks: Use cases and technologies," *IEEE Communications Magazine*, vol. 58, no. 3, pp. 55–61, 2020.

[53] S. U. Rehman, S. Ullah, P. H. J. Chong, S. Yongchareon, and D. Komosny, "Visible light communication: a system perspective—overview and challenges," *Sensors*, vol. 19, no. 5, p. 1153, 2019.

[54] "Introduction to infrared reflectography," September 2021. [Online]. Available: https://www.opusinstruments.com/infrared-reflectography/

[55] P. H. Pathak, X. Feng, P. Hu, and P. Mohapatra, "Visible light communication, networking, and sensing: A survey, potential and challenges," *IEEE communications surveys & tutorials*, vol. 17, no. 4, pp. 2047–2077, 2015.

[56] M. Z. Chowdhury, M. T. Hossan, A. Islam, and Y. M. Jang, "A comparative survey of optical wireless technologies: Architectures and applications," *IEEE Access*, vol. 6, pp. 9819–9840, 2018.

[57] Z. Gu, J. Zhang, Y. Ji, L. Bai, and X. Sun, "Network topology reconfiguration for FSO-based fronthaul/backhaul in 5G+ wireless networks," *IEEE Access*, vol. 6, pp. 69 426–69 437, 2018.

[58] H. Viswanathan and P. E. Mogensen, "Communications in the 6G era," *IEEE Access*, vol. 8, pp. 57 063–57 074, 2020.

[59] G. A. Mapunda, R. Ramogomana, L. Marata, B. Basutli, A. S. Khan, and J. M. Chuma, "Indoor Visible Light Communication: A Tutorial and Survey," *Wireless Communications and Mobile Computing*, vol. 2020, 2020.

[60] S. A. Al-Gailani, M. F. M. Salleh, A. A. Salem, R. Q. Shaddad, U. U. Sheikh, N. A. Algeelani, and T. A. Almohamad, "A Survey of Free Space Optics (FSO) Communication Systems, Links, and Networks," *IEEE Access*, vol. 9, pp. 7353–7373, 2020.

[61] A. K. Majumdar, "Chapter 4 - Fundamentals of Free-Space Optical Communications Systems, Optical Channels, Characterization, and Network/Access Technology," in *Optical Wireless Communications for Broadband Global Internet Connectivity*, A. K. Majumdar, Ed. Elsevier, 2019, pp. 55–116. [Online]. Available: https://www.sciencedirect.com/science/article/pii/B9780128133651000047

[62] M. Garlinska, A. Pregowska, K. Masztalerz, and M. Osial, "From mirrors to free-space optical communication—historical aspects in data transmission," *Future Internet*, vol. 12, no. 11, p. 179, 2020.

[63] H. Kaushal, V. Jain, and S. Kar, *Free space optical communication*. Springer, 2017.

[64] I. K. Son and S. Mao, "A survey of free space optical networks," *Digital communications and networks*, vol. 3, no. 2, pp. 67–77, 2017.

[65] X. Wu, M. D. Soltani, L. Zhou, M. Safari, and H. Haas, "Hybrid LiFi and WiFi networks: A survey," *IEEE Communications Surveys & Tutorials*, vol. 23, no. 2, pp. 1398–1420, 2021.

[66] D. Tsonev, S. Videv, and H. Haas, "Light Fidelity (Li-Fi): towards all-optical networking," in *Broadband Access Communication Technologies VIII*, vol. 9007. International Society for Optics and Photonics, 2014, p. 900702.

[67] N. Saha, M. S. Ifthekhar, N. T. Le, and Y. M. Jang, "Survey on optical camera communications: challenges and opportunities," *Iet Optoelectronics*, vol. 9, no. 5, pp. 172–183, 2015.

[68] N. T. Le, M. A. Hossain, and Y. M. Jang, "A survey of design and implementation for optical camera communication," *Signal Processing: Image Communication*, vol. 53, pp. 95–109, 2017.

[69] T. Nguyen, A. Islam, T. Hossan, and Y. M. Jang, "Current status and performance analysis of optical camera communication technologies for 5G networks," *IEEE Access*, vol. 5, pp. 4574–4594, 2017.

[70] Y. Tanaka, S. Haruyama, and M. Nakagawa, "Wireless optical transmissions with white colored LED for wireless home links," in *11th IEEE International Symposium on Personal Indoor and Mobile Radio Communications. PIMRC 2000. Proceedings (Cat. No. 00TH8525)*, vol. 2. IEEE, 2000, pp. 1325–1329.

[71] G. Pang, K.-L. Ho, T. Kwan, and E. Yang, "Visible light communication for audio systems," *IEEE Transactions on Consumer Electronics*, vol. 45, no. 4, pp. 1112–1118, 1999.

[72] Boundless, "Boundless physics," September 2021. [Online]. Available: https://courses.lumenlearning.com/boundless-physics/chapter/the-electromagnetic-spectrum/

[73] J. Chen, T. Liu, and T. Shu, "A Survey on Visible Light Communication Standards," *GetMobile: Mobile Computing and Communications*, vol. 25, no. 1, pp. 9–15, 2021.

[74] M. Nakagawa, "Greeting from Honorary Chairman," September 2021. [Online]. Available: http://www.vlcc.net/modules/xpage1/

[75] S. Haruyama, "JEITA standards CP-1221: Visible light communications system (in Japanese)," September 2021. [Online]. Available: https://www.jeita.or.jp/cgi-bin/standard/list.cgi?cateid=1&subcateid=50

[76] ——, "JEITA standards CP-1222: Visible light ID system (in Japanese)," September 2021. [Online]. Available: https://www.jeita.or.jp/cgi-bin/standard/list.cgi?cateid=1&subcateid=50

[77] ——, "JEITA standards CP-1223: Visible light beacon system (in Japanese)," September 2021. [Online]. Available: https://www.jeita.or.jp/cgi-bin/standard/list.cgi?cateid=1&subcateid=50

[78] "Visible Light Communications Association," September 2021. [Online]. Available: https://j-photonics.org/vlca/en/

[79] "IEEE 802.15 WPAN™ Task Group 7 (TG7) Visible Light Communication," September 2021. [Online]. Available: https://www.ieee802.org/15/pub/TG7.html

[80] "IEEE Standard for Local and Metropolitan Area Networks–Part 15.7: Short-Range Wireless Optical Communication Using Visible Light," pp. 1–309, 2011. [Online]. Available: https://ieeexplore.ieee.org/document/6016195

[81] "IEEE Standard for Local and metropolitan area networks–Part 15.7: Short-Range Optical Wireless Communications," pp. 1–407, 2019. [Online]. Available: https://ieeexplore.ieee.org/document/8697198

[82] "IEEE 802.15 Vehicular Assistant Technology Interest Group," September 2019. [Online]. Available: https://mentor.ieee.org/802.15/documents?is_dcn=DCN%2C%20Title%2C%20Author%20or%20Affiliation&is_group=0vat

[83] "IEEE P802.11 - LIGHT COMMUNICATION (LC) TASK GROUP (TG)," September 2019. [Online]. Available: https://www.ieee802.org/11/Reports/tgbb_update.htm

[84] Spectrum Management Series, "Visible light for broadband communications," The International Telecommunication Union-Radiocommunication Sector, Tech. Rep., June 2018.

[85] ITU-T Recommendations, "G.9961 (03/2019): High-speed indoor visible light communication transceiver – System architecture, physical layer and data link layer specification," The International Telecommunication Union-Telecommunication Standardization, Tech. Rep., April 2021.

[86] ——, "G.9960 : Unified high-speed wireline-based home networking transceivers - System architecture and physical layer specification," The International Telecommunication Union-Telecommunication Standardization, Tech. Rep., November 2018.

[87] J.-H. Yoo and S.-Y. Jung, "Modeling and analysis of variable ppm for visible light communications," *EURASIP Journal on Wireless Communications and Networking*, vol. 2013, no. 1, pp. 1–6, 2013.

[88] E. Monteiro and S. Hranilovic, "Design and implementation of color-shift keying for visible light communications," *Journal of Lightwave Technology*, vol. 32, no. 10, pp. 2053–2060, 2014.

[89] G. Held, *Introduction to light emitting diode technology and applications*. Auerbach publications, 2016.

[90] E. C. Strinati, S. Barbarossa, J. L. Gonzalez-Jimenez, D. Ktenas, N. Cassiau, L. Maret, and C. Dehos, "6G: The next frontier: From holographic messaging to artificial intelligence using subterahertz and visible light communication," *IEEE Vehicular Technology Magazine*, vol. 14, no. 3, pp. 42–50, 2019.

[91] M. Katz and I. Ahmed, "Opportunities and challenges for visible light communications in 6G," in *2020 2nd 6G wireless summit (6G SUMMIT)*. IEEE, 2020, pp. 1–5.

[92] A. Faisal, R. Alghamdi, H. Dahrouj, H. Sarieddeen, N. Saeed, T. Y. Al-Naffouri, and M.-S. Alouini, "Diversity Schemes in Multi-hop Visible Light Communications for 6G Networks," *Procedia Computer Science*, vol. 182, pp. 140–149, 2021.

[93] A. M. Vegni, M. Hammouda, and V. Loscrí, "A VLC-based Footprinting Localization Algorithm for Internet of Underwater Things in 6G networks," in *2021 17th International Symposium on Wireless Communication Systems (ISWCS)*. IEEE, 2021, pp. 1–6.

[94] L. Grobe, A. Paraskevopoulos, J. Hilt, D. Schulz, F. Lassak, F. Hartlieb, C. Kottke, V. Jungnickel, and K.-D. Langer, "High-speed visible light communication systems," *IEEE communications magazine*, vol. 51, no. 12, pp. 60–66, 2013.

[95] M. Saadi, T. Ahmad, M. Kamran Saleem, and L. Wuttisittikulkij, "Visible light communication–an architectural perspective on the applications and data rate improvement strategies," *Transactions on Emerging Telecommunications Technologies*, vol. 30, no. 2, p. e3436, 2019.

[96] B. CREW, "JEITA standards CP-1221: Visible light communications system (in Japanese)," November 2015. [Online]. Available: https://www.sciencealert.com/li-fi-tested-in-the-real-world-for-the-first-time-is-100-times-faster-than-wi-fi

[97] M. T. Rahman, A. S. M. Bakibillah, R. Parthiban, and M. Bakaul, "Review of advanced techniques for multi-gigabit visible light communication," *IET Optoelectronics*, vol. 14, no. 6, pp. 359–373, 2020.

[98] H. Chun, A. Gomez, C. Quintana, W. Zhang, G. Faulkner, and D. O'Brien, "A wide-area coverage 35 Gb/s visible light communications link for indoor wireless applications," *Scientific reports*, vol. 9, no. 1, pp. 1–8, 2019.

[99] Y. Zhang, G. Qiu, M. Liu, and H. Wang, "High-density data transmission and scheduling method in wireless sensor networks based on Wi-Fi," *International Journal of Distributed Sensor Networks*, vol. 16, no. 7, p. 1550147720943414, 2020.

[100] T. Nawaz, M. Seminara, S. Caputo, L. Mucchi, F. S. Cataliotti, and J. Catani, "IEEE 802.15. 7-compliant ultra-low latency relaying VLC system for safety-critical ITS," *IEEE Transactions on Vehicular Technology*, vol. 68, no. 12, pp. 12 040–12 051, 2019.

[101] M. A. Arfaoui, M. D. Soltani, I. Tavakkolnia, A. Ghrayeb, M. Safari, C. M. Assi, and H. Haas, "Physical layer security for visible light communication systems: A survey," *IEEE Communications Surveys & Tutorials*, vol. 22, no. 3, pp. 1887–1908, 2020.

[102] C. Rohner, S. Raza, D. Puccinelli, and T. Voigt, "Security in visible light communication: Novel challenges and opportunities," *Sensors & Transducers Journal*, vol. 192, no. 9, pp. 9–15, 2015.

[103] M. Figueiredo, L. N. Alves, and C. Ribeiro, "Lighting the wireless world: The promise and challenges of visible light communication," *IEEE Consumer Electronics Magazine*, vol. 6, no. 4, pp. 28–37, 2017.

[104] M. Z. Chowdhury, M. K. Hasan, M. Shahjalal, M. T. Hossan, and Y. M. Jang, "Optical wireless hybrid networks: Trends, opportunities, challenges, and research directions," *IEEE Communications Surveys & Tutorials*, vol. 22, no. 2, pp. 930–966, 2020.

[105] H. Kaushal and G. Kaddoum, "Underwater optical wireless communication," *IEEE access*, vol. 4, pp. 1518–1547, 2016.

[106] M. Vieira, M. Vieira, P. Louro, and P. Vieira, "Positioning and advertising in large indoor environments using visible light communication," *Optical Engineering*, vol. 58, no. 6, p. 066102, 2019.

[107] Y. Almadani, D. Plets, S. Bastiaens, W. Joseph, M. Ijaz, Z. Ghassemlooy, and S. Rajbhandari, "Visible light communications for industrial applications—challenges and potentials," *Electronics*, vol. 9, no. 12, p. 2157, 2020.

[108] J. An, N. Q. Pham, and W.-Y. Chung, "Multiple bio-monitoring system using visible light for electromagnetic-wave free indoor healthcare," *Optics Communications*, vol. 405, pp. 107–113, 2017.

[109] D. R. Dhatchayeny, S. Arya, and Y. H. Chung, "Infrared-based multiple-patient monitoring in indoor optical wireless healthcare systems," *IEEE Sensors Journal*, vol. 19, no. 14, pp. 5594–5599, 2019.

[110] A.-M. Căilean and M. Dimian, "Current challenges for visible light communications usage in vehicle applications: A survey," *IEEE Communications Surveys & Tutorials*, vol. 19, no. 4, pp. 2681–2703, 2017.

[111] Y. Zhuang, Z. Syed, Y. Li, and N. El-Sheimy, "Evaluation of two WiFi positioning systems based on autonomous crowdsourcing of handheld devices for indoor navigation," *IEEE Transactions on Mobile Computing*, vol. 15, no. 8, pp. 1982–1995, 2015.

[112] P. Bahl and V. N. Padmanabhan, "RADAR: An in-building RF-based user location and tracking system," in *Proceedings IEEE INFOCOM 2000. Conference on computer communications. Nineteenth annual joint conference of the IEEE computer and communications societies (Cat. No. 00CH37064)*, vol. 2. Ieee, 2000, pp. 775–784.

[113] A. M. Hossain and W.-S. Soh, "A comprehensive study of bluetooth signal parameters for localization," in *2007 IEEE 18th International Symposium on Personal, Indoor and Mobile Radio Communications*. IEEE, 2007, pp. 1–5.

[114] Y. Zhuang, J. Yang, Y. Li, L. Qi, and N. El-Sheimy, "Smartphone-based indoor localization with bluetooth low energy beacons," *Sensors*, vol. 16, no. 5, p. 596, 2016.

[115] A. Cheema, M. Alsmadi, and S. Ikki, "Distance estimation error performance of visible light communication under the effect of signal-dependent noise," in *2021 IEEE 32nd Annual International Symposium on Personal, Indoor and Mobile Radio Communications (PIMRC)*, 2021, pp. 771–776.

[116] C. Gong, "Visible light communication and positioning: Present and future," 2019.

[117] A. Cheema, M. Alsmadi, and S. Ikki, "Distance Estimation in Visible Light Communications: The Case of Imperfect Synchronization and Signal-Dependent Noise," *IEEE Transactions on Vehicular Technology*, vol. 70, no. 10, pp. 11 044–11 049, 2021.

[118] D. Plets, S. Bastiaens, L. Martens, and W. Joseph, "An analysis of the impact of LED tilt on visible light positioning accuracy," *Electronics*, vol. 8, no. 4, p. 389, 2019.

[119] Y. Zhuang, L. Hua, Q. Wang, Y. Cao, Z. Gao, L. Qi, J. Yang, and J. Thompson, "Visible light positioning and navigation using noise measurement and mitigation," *IEEE Transactions on Vehicular Technology*, vol. 68, no. 11, pp. 11 094–11 106, 2019.

[120] L. Hua, Y. Zhuang, L. Qi, J. Yang, and L. Shi, "Noise analysis and modeling in visible light communication using Allan variance," *IEEE Access*, vol. 6, pp. 74 320–74 327, 2018.

[121] T. Komine and M. Nakagawa, "Fundamental analysis for visible-light communication system using LED lights," *IEEE transactions on Consumer Electronics*, vol. 50, no. 1, pp. 100–107, 2004.

[122] J.-Y. Wang, J.-B. Wang, and Y. Wang, "Fundamental analysis for visible light communication with input-dependent noise," *Optical Fiber and Wireless Communications*, pp. 143–157, 2017.

[123] Q. Gao, C. Gong, and Z. Xu, "Joint transceiver and offset design for visible light communications with input-dependent shot noise," *IEEE Transactions on Wireless Communications*, vol. 16, no. 5, pp. 2736–2747, 2017.

[124] M. F. Keskin and S. Gezici, "Comparative theoretical analysis of distance estimation in visible light positioning systems," *Journal of Lightwave Technology*, vol. 34, no. 3, pp. 854–865, 2016.

[125] A. Memedi and F. Dressler, "Vehicular visible light communications: A survey," *IEEE Communications Surveys & Tutorials*, vol. 23, no. 1, pp. 161–181, 2020.

[126] Y. Shen, G. Chen, X. Xu, C. Xu, G. Shen, and J. Li, "Poster: A VLC Solution for Smart Parking," in *Proceedings of the 23rd Annual International Conference on Mobile Computing and Networking*, 2017, pp. 579–581.

[127] M. Qiang, L. Jiaming, Z. Qinfeng, and H. Chunliang, "Indoor Parking Navigation System Using Visible LED Light Communication," in *2019 IEEE International Conference on Computation, Communication and Engineering (ICCCE)*. IEEE, 2019, pp. 157–159.

[128] N. Krommenacker, Ó. C. Vásquez, M. D. Alfaro, and I. Soto, "A self-adaptive cell-ID positioning system based on visible light communications in underground mines," in *2016 IEEE International Conference on Automatica (ICA-ACCA)*. IEEE, 2016, pp. 1–7.

[129] Q. Gao, S. Hu, C. Gong, and Z. Xu, "Modulation designs for visible light communications with signal-dependent noise," *Journal of Lightwave Technology*, vol. 34, no. 23, pp. 5516–5525, 2016.

[130] A. Şahin, Y. S. Eroğlu, I. Güvenç, N. Pala, and M. Yüksel, "Hybrid 3-D localization for visible light communication systems," *Journal of Lightwave Technology*, vol. 33, no. 22, pp. 4589–4599, 2015.

[131] Y. Zhu and N. Reid, "Information, ancillarity, and sufficiency in the presence of nuisance parameters," *Canadian Journal of Statistics*, vol. 22, no. 1, pp. 111–123, 1994.

Appendix A

Visible Light Positioning System Models

A.1 Cramér–Rao Lower Bound

$$\underbrace{r_n}_{\text{Observations}} = \underbrace{\varrho}_{\text{Parameter}} + \underbrace{\eta}_{\text{Noise}},$$

where n is the number of observations.

$$\underbrace{e}_{\text{Error}} = \underbrace{\hat{\varrho}}_{\text{Estimated}} - \underbrace{\varrho}_{\text{Parameter}} \neq 0,$$

$\hat{\varrho}$ is the estimated parameter. There is a need to minimize this error. The Cramer-Rao inequality addresses this question in two steps.

- First, it provides a lower bound to the minimum possible variance achievable by any unbiased estimator. This bound provides a benchmark for assessing all unbiased estimators of $\boldsymbol{\varrho}$.
- Second, if an unbiased estimator achieves the lower bound then it has the smallest possible variance and mean square error.

A.2 Received Signal Model

The received signal model commonly used in the literature is the free-space optical intensity channel, where it is assumed the corrupting noise is additive white Gaussian

distributed and independent of the received signal, is given as [33]

$$r(t) = \alpha R\, x(t-\tau) + \eta(t) \tag{A.1}$$

$$\eta(t) \sim N(0, \sigma_n^2) \tag{A.2}$$

This assumption is reasonable if the ambient light is strong or if the receiver suffer from intensive thermal noise. However, particularly at high power, this model neglects a fundamental issue of optical communication: the noise depends on the signal itself due to random nature of photon emissions in the photodiode and laser diode. The received signal model considering both input-dependent and input-independent noises, a scenario that better reflects the VLC system's physical properties, is given as [47]

$$r(t) = \alpha R\, x(t-\tau) + \sqrt{\alpha R\, x(t-\tau)}\, \eta_{\text{sh}}(t) + \eta_{\text{th}}(t) \tag{A.3}$$

$$\eta_{\text{sh}}(t) \sim N(0, \zeta_n^2 \sigma_n^2) \tag{A.4}$$

$$\eta_{\text{th}}(t) \sim N(0, \sigma_n^2) \tag{A.5}$$

As a result, (A.3) can be re-written as [33]

$$y(t) = \alpha\, R\, x(t-\tau) + \Omega(t). \tag{A.6}$$

where,

$$\Omega(t) = \sqrt{\alpha R\, x(t-\tau)}\, \eta_{\text{sh}}(t) + \eta_{\text{th}}(t) \tag{A.7}$$

$$\Omega(t) \sim N(0, \Gamma) \tag{A.8}$$

$$\Gamma = \sigma_n^2 \left(1 + \alpha\, R\, x(t-\tau)\, \zeta_n^2\right) \tag{A.9}$$

The PDF of the normal or Gaussian random variable can be written as [33]

$$\text{f}(y(t)|x) = \frac{1}{\sqrt{2\,\pi\,\Gamma}} \exp\left(-\frac{1}{2\,\Gamma}\left(y(t) - \alpha\, R\, x(t-\tau)\right)^2\right). \tag{A.10}$$

By observing the interval of the transmitted signal, the log-likelihood function [33]

$$\ln \text{f}(y(t)|x) = \mathcal{L}\left(\boldsymbol{\varrho}\right) = -\frac{1}{2}\ln\left(2\,\pi\right) - \frac{1}{2}\int_{T_1}^{T_2} \ln\, \sigma_n^2 \left(1 + \alpha\, R\, x(t-\tau)\, \zeta_n^2\right) dt$$

$$- \frac{1}{2\,\sigma_n^2} \int_{T_1}^{T_2} \frac{\left(y(t) - \alpha\, R\, x(t-\tau)\right)^2}{(1 + \alpha\, R\, x(t-\tau)\zeta_n^2)} dt, \tag{A.11}$$

the Fisher information matrix (FIM) of $\boldsymbol{\varrho}$, which can be obtained from $\boldsymbol{\mathcal{L}}\left(\boldsymbol{\varrho}\right)$

$$\boldsymbol{\mathcal{I}}(\boldsymbol{\varrho}) = \mathbb{E}\left\{ \left(\nabla_{\boldsymbol{\varrho}} \boldsymbol{\mathcal{L}}(\boldsymbol{\varrho})\right) \left(\nabla_{\boldsymbol{\varrho}} \boldsymbol{\mathcal{L}}(\boldsymbol{\varrho})\right)^T \right\},$$

where $\nabla_{\boldsymbol{\varrho}}$ is the gradient operator. The CRLB is obtained by taking the inverse of the FIM. The estimation error covariance can consequently be expressed as

$$\mathbb{E}\big\{ (\hat{\boldsymbol{\varrho}} - \boldsymbol{\varrho})(\hat{\boldsymbol{\varrho}} - \boldsymbol{\varrho})^{\mathrm{T}} \big\} \succeq \boldsymbol{\mathcal{I}}(\boldsymbol{\varrho})^{-1}.$$